MASARYKOVA UNIVERZITA
Přírodovědecká fakulta
Ústav fyziky kondenzovaných látek

DIPLOMOVÁ PRÁCE

Brno 2024 Bc. Katarína Porubčanová

MASARYKOVA
UNIVERZITA

Přírodovědecká fakulta
Ústav fyziky kondenzovaných látek

Struktura polovodičových mikrokrystalů na mřížkově nepřizpůsobeném substrátu

Diplomová práce

Bc. Katarína Porubčanová

Vedoucí diplomové práce:
Mgr. Mojmír Meduňa, Ph.D.

Brno 2024

Bibliografický záznam

Autor:	Bc. Katarína Porubčanová Přírodovědecká fakulta, Masarykova univerzita Ústav fyziky kondenzovaných látek
Název práce:	Struktura polovodičových mikrokrystalů na mřížkově nepřispůsobeném substrátu
Studijní program:	Fyzika kondenzovaných látek
Směr:	Fyzika kondenzovaných látek
Vedoucí práce:	Mgr. Mojmír Meduňa, Ph.D.
Akademický rok:	2023/2024
Počet stran:	ix + 71
Klíčová slova:	heteroepitaxe; křemík; germanium; mikrokrystaly; RTG difrakce; mřížkový parametr; mapování reciprokého prostoru

Bibliographic record

Author:	Bc. Katarína Porubčanová Faculty of Science, Masaryk University Department of Condensed Matter
Title of Thesis:	Structure of semiconductor microcrystals on lattice mismatched substrate
Degree Programme:	Condensed matter physics
Supervisor:	Mgr. Mojmír Meduňa, PhD
Academic Year:	2023/2024
Number of Pages:	ix + 71
Keywords:	heteroepitaxy; silicon; germanium; microcrystals; X-ray diffraction; lattice parameter; reciprocal space mapping

Abstrakt

V této diplomové práci se zabýváme studiem epitaxních Ge mikrokrystalů, které jsou deponovány na předem vzorkovaném Si substrátu. Tento způsob přípravy vzorků byl poprvé použit na ETH Zürich, kde byly vyrobeny i naše vzorky. Celkem bylo změřeno 30 vzorků, které pocházejí z jedné Si desky. Vzorky byly rozděleny do dvou skupin podle vzorkovaní substrátu. K dispozici jsme měli vzorky s pilíři a dráty, na kterých bylo deponováno Ge ve formě mikrokrystalů. Tyto pilíře a dráty se lišily velikostí základny nebo velikostí mezer mezi nimi. Symetrické a asymetrické difrakční mapy byly měřeny pro každý vzorek pomocí mapování difúzního rozptylu rentgenového záření v reciprokém prostoru. Z polohy píků v difrakčních mapách byly určeny mřížové parametry, paralelní a kolmé složky tenzoru deformace a relaxace. Byly také diskutovány profily meřených map difrakčním píkem. Za účelem lepšího určení hodnot structúrních parametrů byl použit profil podél osy Q_z. Položířky difrakčních maxim byly určeny z průřezu podél Q_x osy. Nakonec byla také zkoumána možnost závislosti získaných parametrů na poloze vzorku na Si desce během depozice.

Abstract

In this diploma thesis, we deal with the study of epitaxial Ge microcrystals, which are deposited on a pre-patterned Si substrate. This method of sample preparation was used for the first time at ETH Zürich, where our samples were produced as well. Totally 30 samples, which come from one Si wafer, were measured. The samples were divided into two groups according to the pattern on the substrate. We had samples with pillars and ridges available. They differed in the size of the base and of the trenches. The symmetrical and the asymmetrical diffraction maps were measured for each sample, using reciprocal space mapping of diffuse X-Ray scattering. The lattice parameters, the parallel and the perpendicular components of the strain tensor and the relaxation state were determined from the positions of the peaks in the diffraction maps. The cross-sections through the diffraction peak were also discussed. The cross-section along Q_z axis was used to determine the parameter values more precisely, while the full width at half maximum was determined from the cross-section along Q_x axis. Finally, the possibility of the dependence of the parameters on the position of the sample on the Si wafer during deposition was investigated.

MUNI
SCI

MASARYKOVA UNIVERZITA
PŘÍRODOVĚDECKÁ FAKULTA
KOTLÁŘSKÁ 2, 611 37 BRNO
IČ: 00216224
DIČ: CZ00216224

ZADÁNÍ
DIPLOMOVÉ PRÁCE

Akademický rok: 2023/2024

Ústav:	Ústav fyziky kondenzovaných látek
Studentka:	Bc. Katarína Porubčanová
Program:	Fyzika
Specializace:	Fyzika kondenzovaných látek

Ředitel *ústavu* PřF MU Vám ve smyslu Studijního a zkušebního řádu MU určuje diplomovou práci s názvem:

Název práce:	Struktura polovodičových mikrokrystalů na mřížkově nepřizpůsobeném substrátu
Název práce anglicky:	Structure of semiconductor microcrystals on lattice mismathed substrate
Jazyk závěrečné práce:	

Oficiální zadání:
Integrace polovodičových součástek směřuje v poslední době nejen ke zvyšování hustoty aktivních prvků na jednom čipu, která se blíží krajnímu limitu (léta známý Moorův zákon), ale také k různorodosti materiálů použitých na jednom čipu (tzv. více než Moore). Použití epitaxních vrstev s různými materiály však přináší řadu obtíží ve formě defektů, které působí proti funkčnosti žádaných optoelektronických součástek. Je to dáno nepřizpůsobením mřížkového parametru vrstvy vůči substrátu. Cílem práce bude měření tlustých epitaxních vrstev složených z mikrokrystalů různých materiálů (např. Ge, GaAs) pomocí rtg rozptylu a skenovacího elektronového mikroskopu. Z rtg difrakčních měření bude určován mřížkový parametr a případně informace o tvaru, samotný tvar včetně krystalových faset bude pozorován také v elektronovém mikroskopu. Předpokladem práce jsou základní znalosti z optiky a fyziky pevných látek.

Vedoucí práce:	Mgr. Mojmír Meduňa, Ph.D.
Datum zadání práce:	7. 10. 2022
V Brně dne:	15. 12. 2023

Zadání bylo schváleno prostřednictvím IS MU.

Bc. Katarína Porubčanová, 7. 10. 2022
Mgr. Mojmír Meduňa, Ph.D., 7. 10. 2022
Mgr. Dušan Hemzal, Ph.D., 7. 10. 2022

Poděkování

V prvom rade by som chcela poďakovať môjmu vedúcemu, Mgr. Mojmírovi Meduňovi Ph.D., za jeho ochotu a výborné rady. Bez neho by táto práca nikdy nevznikla. Ďalej by som chcela poďakovať doc. RNDr. Petrovi Mikulíkovi Ph.D. za pomoc pri práci so skenovacím elektrónovým mikroskopom. Ďakujem môjmu priateľovi a mojej rodine, ktorí ma podporovali počas celého štúdia.

Prohlášení

Prohlašuji, že jsem svoji diplomovou práci vypracovala samostatně s využitím informačních zdrojů, které jsou v práci citovány.

Brno 2.1. 2024

Podpis autora

Contents

1 Introduction **1**

2 Growth of heteroepitaxial layers **3**
2.1 Difference in lattice parameters 3
2.2 Difference in thermal expansion coefficient 4
2.3 Tower morphology 5

3 Kinematical diffraction theory **9**
3.1 General description 10
3.2 Diffraction from perfect crystal 11
3.3 Structure factor 12
3.4 Geometrical factor 13

4 Experimental methods **14**
4.1 Reciprocal space mapping 14
4.2 Structural properties by RSM 16

5 Measurement and results **19**
5.1 Experimental set-up 19
5.2 About the samples 20
5.3 Examples of a reciprocal space maps 21
5.4 Pillars with the same base 24
5.4.1 X2 series, base 5×5 μm 24
5.4.2 X3 series, base 9×9 μm 30
5.4.3 X4 series, base 15×15 μm 33
5.5 Ridges 36
5.5.1 Parallel to [110] 36
5.5.2 Parallel to [100] 40
5.6 The peak elongation in Q_x direction 44
5.7 Coverage 46
5.8 Full width at half maximum of diffraction peaks 48
5.9 Properties depending on location of the sample 51

6 Summary **53**

7 Conclusion **57**

Bibliography **58**

A Parameters for all samples **60**

B Asymmetrical maps **70**

Chapter 1

Introduction

For many years, researchers have been interested in the heteroepitaxial growth of various semiconductor materials on silicon (Si). Highly perfect epitaxial semiconductor layers form the basis for many low-dimensional quantum structures and can be used for ultrafast transistors, solid-state lasers, and detectors. However, many challenges arise when materials differ in the lattice parameters and its thermal properties, making it difficult to maintain defect-free epitaxial structures. This challenge often leads to the emergence of misfit dislocations alongside threading dislocations, substrate bowing and even the layer cracking in the layers exceeding a certain critical thickness [1].

To address these challenges, an alternative approach involves creating space-filling arrays composed of discrete semiconductor microcrystals rather than the continuous layer. Achieving this involves employing a high aspect ratios of these microarays in non-equilibrium deposition settings. The result is a dense network of three-dimensional epitaxial crystals on a micrometer scale. Here, misfit dislocations and threading dislocations are restricted near the heterointerface, while the micro crystal tops usually remain defect-free [2].

X-ray diffraction is a commonly used method for studying defects in epitaxial layers, both qualitatively and quantitatively. This method is frequently used to determine layer structural properties, such as the lattice parameters, strain, relaxation, and defect concentration. In this diploma thesis, we focus on the qualitative X-ray analysis of epitaxially grown samples of Ge on Si. The study involves measuring reciprocal space maps (RSM) around the sample's diffraction maxima, from which their structural properties are obtained [3].

In the second chapter, heteroepitaxy and the challenges associated with the growth will be presented. Subsequently, samples grown in the form of space-filling arrays will be discussed. The samples were prepared at ETH Zurich. In the third chapter, the basics of the kinematic theory of X-ray diffraction will be described, which will serve as the basis for the analysis of the measured data. The fourth chapter will describe the details of the used X-ray diffraction technique — measuring RSM — alongside the equations employed to derive parameters from the measured RSMs. The fifth chapter will present and discuss the results, categorized into two primary groups based on the shape of the pre-patterned Si substrate. The first group consists from square based pillars with different

sized bases and trenches between the pillars. These samples will be sorted into groups according to the size of the pillar. The second group consists from ridge base samples. They differ in the orientation of the ridges. The sixth and seventh chapters contain summary of the results and a conclusion.

Chapter 2

Growth of heteroepitaxial layers

Epitaxial growth is a process used to deposit a crystalline thin film of one material onto a crystalline substrate in a way that the deposited atoms or molecules align with the underlying crystal lattice of the substrate. The epitaxial layer and the substrate exhibit a high degree of structural and chemical conformance as a result of this alignment.

On the other hand, heteroepitaxial growth is a specific type of epitaxial growth in which a thin film is deposited onto a crystalline substrate, but the layer and the substrate are made of different materials with different crystal structures. In heteroepitaxy, the challenge is to align the crystal lattices of two different materials into defect free structure, which can result in various interesting and potentially useful properties. This can also cause several problems during the preparation of such layers.

2.1 Difference in lattice parameters

Difference in lattice parameters is also called lattice mismatch, and can be calculated as [3]:

$$\left(\frac{\Delta a}{a}\right) = \frac{a_L - a_S}{a_S} \tag{2.1}$$

where a_L stands for lattice parameter of the layer, in our case Ge, and a_S for substrate, which is in our case Si. Lattice parameter for germanium (Ge) is $a_L = 5{,}6579$ Å, and for silicon (Si) $a_S = 5{,}4310$ Å, which leads to lattice mismatch of 4,2% [4]. In the case of a mismatch, there are two possible limit configurations for the deposited layer, as indicated in figure 2.1.

If the deposited layer has the same properties as the bulk crystal made from the same material, it is referred to as a relaxed layer. In cubic structures, this means that the perpendicular and parallel lattice parameters have identical values, this can be seen in figure 2.1(a). These layers exhibit no strain, however interfacial defects, usually misfit dislocations, emerge due to difference in lattice parameters.

On the other hand, if the deposited layer fully adapts to the lattice parameter of the substrate, this is called pseudomorphic layer. The pseudomorphic layer

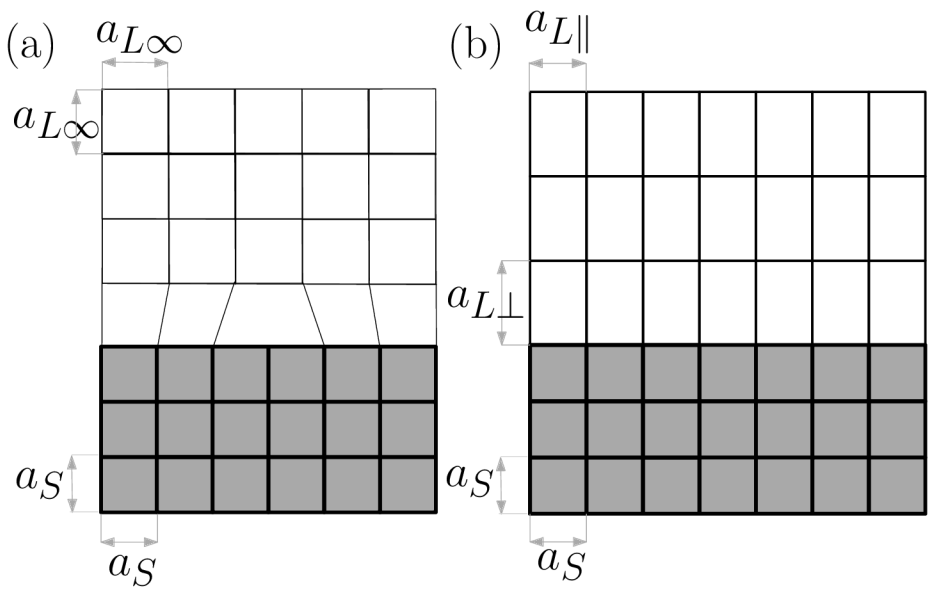

Figure 2.1 (a) Relaxed and (b) pseudomorphic heterostructures. Lattice parameter of the substrate is marked a_S and for the layer $a_{L\infty}$, which denotes lattice parameter of bulk material $a_{L\perp}$ denotes the lattice parameter perpendicular to the substrate and $a_{L\parallel}$ denotes the lattice parameter parallel to the substrate plane, based on [3].

exhibits strain, as the change in the parallel lattice parameter leads to the opposite change in the perpendicular one, as shown in figure 2.1(*b*) [3].

Growing pseudomorphic structures beyond a certain thickness becomes challenging due to formation of the misfit dislocations, see figure 2.1(a). Misfit dislocations are always accompanied by threading dislocations, which propagate towards the surface and can involve active device regions far from the dislocated interface. This critical thickness is very limiting for practical use of heteroepitaxy [5].

2.2 Difference in thermal expansion coefficient

Next to the lattice mismatch, another complication in the growth of heteroepitaxial layers is the difference in thermal expansion coeffiecient. At room temperature the thermal expansion coefficient for Ge is $\alpha_L = 5{,}8 \cdot 10^{-6}$ K^{-1} and for Si it is $\alpha_S = 2{,}5 \cdot 10^{-6}$ K^{-1} [4], which leads to the mismatch of 132 % using the equation below [5]:

$$\left(\frac{\Delta\alpha}{\alpha}\right) = \frac{\alpha_L - \alpha_S}{\alpha_S}. \tag{2.2}$$

Epitaxial layer growth typically involves high-temperature processes, followed by cooling to room temperature. The abrupt temperature decrease, coupled with different coefficients of the thermal expansion, leads to a contraction of the materials, with each material experiencing different shortening. This results in

bending deformation, which can be compared with deformations observed in a bimetallic strip [6].

2.3 Tower morphology

In previous sections, we have discussed the challenges that arise during the growth of continuous heteroepitaxial layers, which made difficult their practical application. In the past, numerous efforts have been made to eliminate defects or reduce their density, and thus ensure the proper functioning of semiconductor components [7, 8]. In 2012, a very promising solution has been proposed by Falub et al [2].

The only practical solution appears to be to replace a continuous layer by a dense arrangement of separate three-dimensional epitaxial crystals [2]. The surface of the Si substrate is initially patterned using photolithography and deep reactive ion etching into pillars with widths of a few micrometers, separated by trenches several µm wide. An example of such patterning can be found in figure 2.2(a). The pillars in figure are 2 µm wide, 8 µm high, and regularly spaced by 2 µm trenches. This represents one example of patterning that can vary from from one sample to another [9].

Afterwards, typically germanium (or another material) is deposited epitaxially using low-energy plasma-enhanced chemical vapor deposition (LEPECVD) mainly on top of these pillars. LEPECVD enables the rapid growth of Ge layers with the necessary thickness and quality for applications forming Ge microcrystals with high aspect ratio, see figure 2.2(b). Typically, microcrystals of heights up to 30 µm, edges varying up to 15 µm, and trenches ranging from nanometers

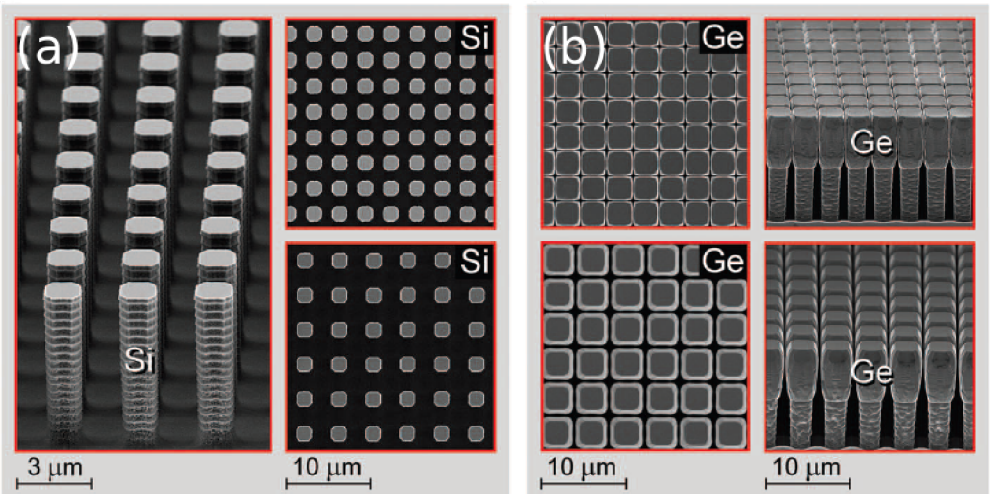

Figure 2.2 (a) SEM micrographs of pillars on Si wafers. These pillars are 8 µm tall, 2 µm wide and made by deep reactive ion etching. (b) SEM micrographs of Ge towers grown by LEPECVD on the Si pillars. Taken from [2].

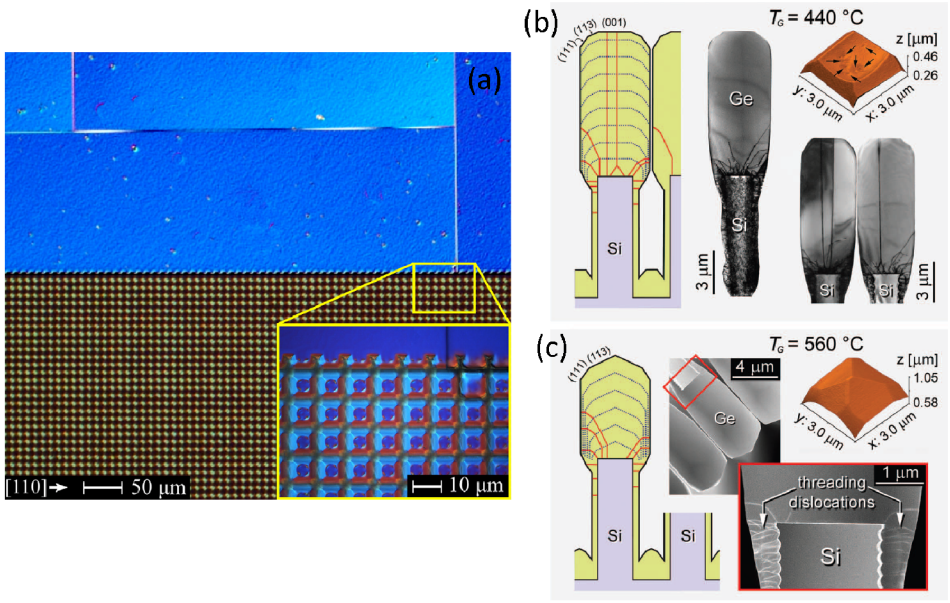

Figure 2.3 (a)Nomarski optical micrograph of the border between unpatterned and patterned areas for 50 µm thick Ge deposited at 490 °C. Taken from [5].(b)(Left) Schematic drawing of growth dislocations trapped in Ge towers and of inclined dislocations escaping to the side walls. (Center) Brightfield TEM crosssection image with inclined dislocations only. (Right) Corresponding TEM images with both kinds of dislocations, and an AFM micrograph taken after defect etching in an iodine solution. (c)Schematic drawing (left), darkfield STEM images (middle), and AFM micrograph (right) for Ge crystals. All dislocations are expelled from the crystals in this case. Taken from [2].

to 50 µm are used [2, 9, 10]. However, even samples with higher microcrystals up to 100 µm were investigated [11]. In this technique, the growth chamber involves a plasma source where the plasma is created through a low-voltage arc discharge, utilizing argon as the discharge gas. Characteristic property of LEPECVD is the capability to independently adjust the energy and density of ions [12].

Another important aspect of this method, especially crucial for growing Ge pillars, is also its speed. A sufficiently high deposition rate is essential for such growth since it restricts the surface diffusion of the deposited atoms. With a growth rate exceeding 4 nm/s, the mean free path of surface diffusion becomes negligible in comparison to the size of the facets of Ge microcrystals, typically ranging from 100 to 200 nm [2].

The growth rate of the Ge microcrystals on these Si pillars varies significantly in different directions, primarily due to the presence of neighboring, growing microcrystals that block the deposition gas from infiltrating the spaces between them. As the microcrystals grow, the space between them decreases, and thus their growth in the lateral direction slows down until it almost stops. While the growth of the crystal in the vertical direction rapidly continues.

Depending on the chosen substrate pattern and on the quantity of material deposited, the arrays of microcrystals can extend across nearly the entire substrate

surface, achieving space fillings of up to 96 %. The filling prevents the formation of a continuous layer, which, in turn, inhibits crack propagation and wafer bowing, regardless of the thickness of the epitaxial layer. This effect is evident in the Nomarski interference contrast image in figure 2.3(a), illustrating the boundary between patterned and unpatterned regions of a 50 µm thick Ge deposited at 490 °C. This image consist of two regions. The continuous region (blue) exhibits numerous cracks resulting from thermal stress during the cool-down phase from the growth temperature, while no cracks have extended into the patterned region (grey) [2].

In the following paragraphs, it will be explored how the tower morphology plays a crucial role in controlling threading dislocations density. At the Si/Ge interface, dislocations form in a manner similar to that observed in layers deposited on the unpatterned substrates. Nevertheless, in the context of isolated microcrystals, dislocations are limited to a small region around the interface. In this particular area, they can be expelled toward the vertical surface, and none of them extend to the top of the Ge pillar [2].

Dislocations that originate at the material interface propagate perpendicular to the microcrystal's surface facets. Unless the microcrystal grows with a facet parallel to the substrate's surface, these dislocations within the microcrystal spread diagonally towards the sides of the microcrystals. Due to the microcrystal's small lateral dimension, they do not reach the surface at the top but rather appear on the sides of the microcrystals. Beyond a certain thickness, growth proceeds already without defects. This is shown in the figure 2.3(b,c) [5].

Additionally, the method of etch pit counting was used to analyse the threading dislocation density. In top right part of the figure 2.3 (b) and (c),

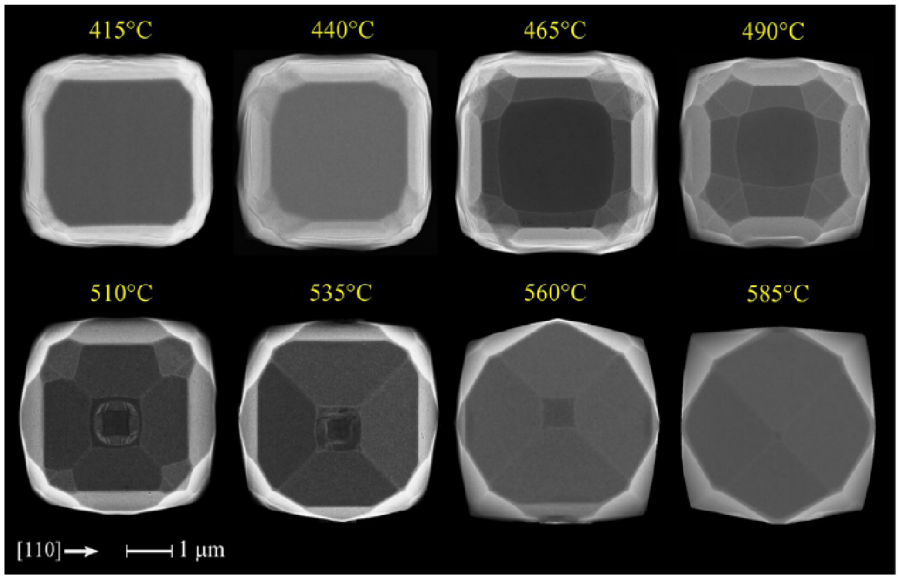

Figure 2.4 Topview SEM micrographs of 8 µm tall Ge crystals grown at different deposition temperatures T_G. Taken from [5].

there are atomic force microscopy (AFM) micrographs, which reveal evenly distributed etch pits on the top facets 2.3(b). When a dislocation extends to the upper surface of the microcrystal, it will manifest as an etch pit after the etching process. Etch pits are denoted by the black arrows. This occurs because the crystal grew with a facet parallel to the substrate's surface [2].

In the AFM image 2.3(c) we do not observe any etch pits, indicating that all the dislocations are indeed displaced to the sides of the microcrystal. This is result of the change in the deposition temperature. The sample in figure 2.3(b) was deposited at temperature $T_G = 440°C$, while the second sample in figure 2.3(c) was deposited at temperature $T_G = 560°C$. This illustrates that the surface morphology of Ge pillars can be controlled by modifying the deposition temperature T_G. In the fully faceted microcrystals, achieved at higher T_G, defects are indeed limited to the lower section of the microcrystals, as indicated by the TEM images 2.3(c) in the middle. The absence of etch pits, see figure 2.3(c) in the right part, further confirms the elimination of threading dislocations from the faceted Ge pillars. Examples of facet shapes for different deposition temperatures are shown in figure 2.4 [2].

As last part of this chapter, lattice bending and the thermal stress will be discussed. Due to the limited surface area of the interface between Si and Ge within the column (on the order of square micrometers), the layer remains crack-free despite differences in the thermal expansion. Instead, the microcrystal lattice simply undergoes bending. Both experimental observations and simulations indicate that the bending of the crystal lattice, caused by the relaxation of thermal strain, diminishes as the height of the Ge microcrystal increases, as shown in figure 2.5. Moreover, at the top of tall crystals the bending of the lattice can be neglected. Furthermore, the strain is exceptionally minimal in regions distant from the bottom interface, rendering these arrays of microcrystals well-suited for device applications [13].

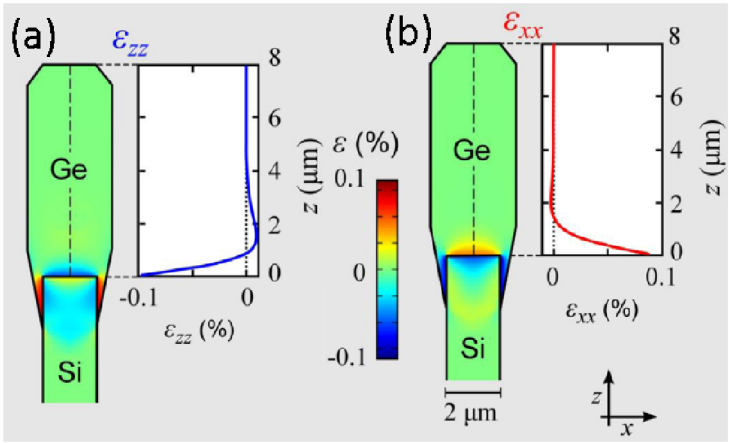

Figure 2.5 FEM calculations of (a)ε_{zz} and (b)ε_{xx} components of the thermal strain for the corresponding Ge crystals, demonstrating that the thermal strain is localized within the Ge microcrystals. Taken from [5].

Chapter 3

Kinematical diffraction theory

In this chapter, we will focus on the kinematical approximation of the diffraction theory. In this theory, it is assumed that an x-ray photon can be scattered only once and the multiple scattering effects are neglected. Another important assumption of this theory is elastic scattering. It means that the incident wave vector $\mathbf{k_i}$ and the refracted wave vector $\mathbf{k_f}$ have the same length $|\mathbf{k_i}|=|\mathbf{k_f}| = \frac{2\pi}{\lambda} = K$, where λ is the X-ray wavelenght. Therefore, the end points of the scattered wave vectors form a spherical surface, which is called Ewald sphere. The allowed diffractions occur when the Ewald construction intersects the reciprocal lattice points [3].

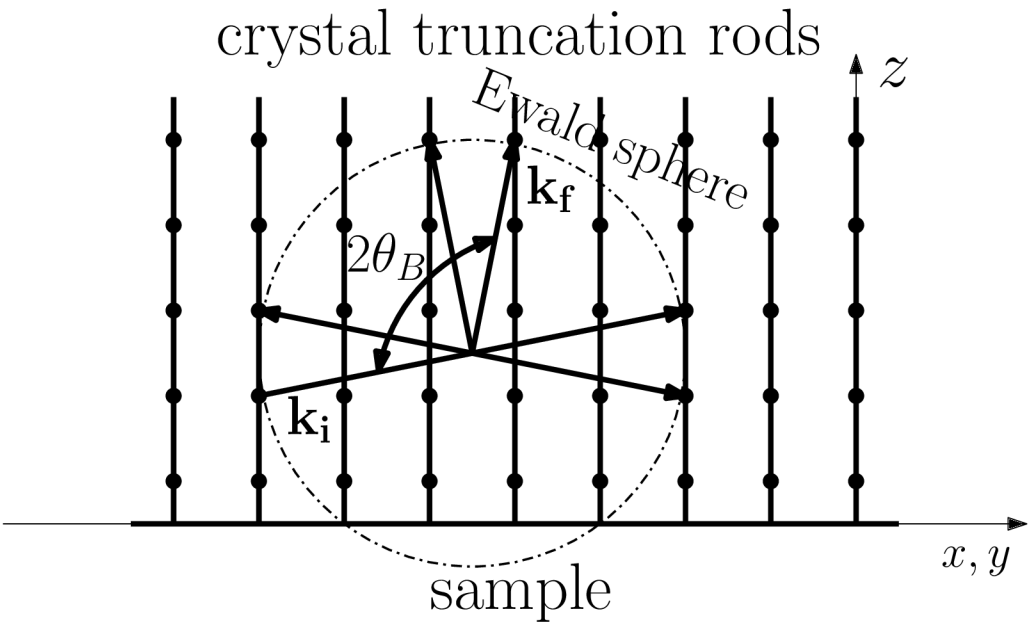

Figure 3.1 The scheme of Ewald construction. The wave vector of the incident wave $\mathbf{k_i}$ points to the origin of reciprocal space and wave vector of diffracted wave to the points of reciprocal lattice. Diffracted vector $\mathbf{k_f}$ has the same lenght as incident wave vector $\mathbf{k_i}$, based on [3].

3.1 General description

Scattering process is described by the scalar wave equation:

$$\left(\Delta + K^2\right)\mathbf{E}\left(\mathbf{r}\right) = \left(graddiv - K^2\chi\left(\mathbf{r}\right)\right)\mathbf{E}\left(\mathbf{r}\right) = \hat{V}\mathbf{E}\left(\mathbf{r}\right) \tag{3.1}$$

where $\hat{V}$ is the scattering potential and $\chi\left(\mathbf{r}\right)$ is the crystal polarisability, which can be expressed by the total electron density as:

$$\chi\left(\mathbf{r}\right) = -\frac{\lambda^2}{\pi} r_{el} C \rho\left(\mathbf{r}\right). \tag{3.2}$$

C is the linear polarisation factor, that depends on the polarisation of the incident wave. The formulation of the scattering potential can be derived from the Maxwell equations [14]. If the right hand side of the equation 3.1 is equal to zero, the expression takes the form of a vacuum wave equation:

$$\left(\Delta + K^2\right)\mathbf{E}\left(\mathbf{r}\right) = 0. \tag{3.3}$$

This homogeneous equation has a solution in form of a plain wave:

$$\mathbf{E}\left(\mathbf{r}\right) = E_i\left(\mathbf{r}\right) e^{ik(\mathbf{k_i}\mathbf{r} - \omega t)}. \tag{3.4}$$

The differencial wave equation (3.1) can be rewriten into the integral form as [3]:

$$\mathbf{E}\left(\mathbf{r}\right) = \mathbf{E_i}\left(\mathbf{r}\right) + \int d\mathbf{r}' G\left(\mathbf{r} - \mathbf{r}'\right)\hat{V}\left(\mathbf{r}'\right)\mathbf{E}\left(\mathbf{r}\right) \tag{3.5}$$

where E_i is solution of of the vacuum wave equation (3.3) and $G\left(\mathbf{r} - \mathbf{r}'\right)$ is the Green function of a free particle. Moreover, the Green function is solution for the following equation [14]:

$$\left(\Delta + K^2\right) G\left(\mathbf{r} - \mathbf{r}'\right) = \delta\left(\mathbf{r} - \mathbf{r}'\right) \tag{3.6}$$

with delta-like right-hand side. Solving this equation we obtain the Green function of a free particle in a form of a spherical wave [3]:

$$G\left(\mathbf{r} - \mathbf{r}'\right) = -\frac{1}{4\pi}\frac{e^{iK|\mathbf{r} - \mathbf{r}'|}}{|\mathbf{r} - \mathbf{r}'|}. \tag{3.7}$$

Subsequently, we substitute polarisability $\chi\left(\mathbf{r}\right)$ (3.2) and the Green function of a free particle (3.7) into the wave equation in intergral form (3.5). At the same time, we will use the solution of the vacuum wave equation in the form of a plain wave (3.4), where we will neglect the time component, because the equations we use are stationary. Additionally, we introduce the of scattering operator $\hat{T} = \hat{V} + \hat{V}G\hat{V} + \hat{V}G\hat{V}G\hat{V} + ...$, which can be simplified in the kinematic approximation as $\hat{T} \approx \hat{V}$. This means that we neglect multiple scattering processes. This first iteration is also known as the first Born approximation. Now we get an explicit expression for the scattered wavefield [3]:

$$\mathbf{E}(\mathbf{r}) = r_{el} C E_i \int d^3\mathbf{r}' \frac{e^{iK|\mathbf{r}-\mathbf{r}'|}}{|\mathbf{r}-\mathbf{r}'|} \rho(\mathbf{r}') e^{i\mathbf{k_i}\cdot\mathbf{r}'}. \tag{3.8}$$

Using far-field limit, the scattered wave has a spherical wavefront. Therefore, the scattering center can be perceived as a point-like scatterer. This is also known as the Fraunhofer approximation and this holds for $|\mathbf{r}| \gg \frac{a^2}{\lambda}$ where a is the size of the scattering object [15]. Within Fraunhofer approximation we can obtain the scattering amplitude as:

$$E(\mathbf{r}) = r_{el} C \frac{E_i e^{iKr}}{r} \int_V d^3\mathbf{r}' \rho(\mathbf{r}') e^{i\mathbf{Q}\cdot\mathbf{r}'} \tag{3.9}$$

where $\rho(\mathbf{r}')$ stands for an electron density of a crystal, $\mathbf{r}\prime$ varies within the volume V and $|\mathbf{r}|$ is the distance of the observer and Q is scattering vector.

3.2 Diffraction from perfect crystal

Henceforth, we assume that a crystalline material is formed by regularly repeating a fundamental structural unit, filling three-dimensional space. Thus, we have regularly arranged atoms in the crystal lattice, where the position vector of each atom can be expressed as:

$$\mathbf{R} = n_1\mathbf{a_1} + n_2\mathbf{a_2} + n_3\mathbf{a_3} \tag{3.10}$$

where $\mathbf{a_1}$, $\mathbf{a_2}$ and $\mathbf{a_3}$ are lattice vectors, and n_1,n_2 and n_3 are integers. Also, the reciprocal lattice can be defined as:

$$\mathbf{g} = m_1\mathbf{b_1} + m_2\mathbf{b_2} + m_3\mathbf{b_3} \tag{3.11}$$

where m_1,m_2 and m_3 are integers. Reciprocal and direct lattice are related by this equation [15]:

$$\mathbf{a_i} \cdot \mathbf{b_j} = 2\pi\delta_{ij}. \tag{3.12}$$

Within the kinematic approximation, the scattering amplitude can be expressed as equation (3.9). It can be written as a superposition of identical units cells, since we assume an ideal crystal that is composed of a sequence of identical elementary unit cells. Afterwards, we introduce the shape function of a crystal $\Omega(\mathbf{R})$. The value of crystal shape function is $\Omega(\mathbf{R}) = 1$ within the crystal and $\Omega(\mathbf{R}) = 0$ outside it. With this knowledge, we can rewrite electron density as [3]:

$$\rho(\mathbf{r}) = \sum_{\mathbf{R}\in V} \rho_c(\mathbf{r}-\mathbf{R}) = \Omega(\mathbf{r}) \sum_{\mathbf{R}} \rho_c(\mathbf{r}-\mathbf{R}) \tag{3.13}$$

where $\mathbf{R}$ are the position vectors of unit cells and V represents a crystal volume. Now we will use the expansion to the Fourier series. This is possible, because the electron density of the crystal is a periodic function:

$$\sum_{\mathbf{R}} \rho_c (\mathbf{r} - \mathbf{R}) = \frac{1}{V_c} \sum_{\mathbf{g}} \rho_c^{FT} (\mathbf{g}) e^{-\mathbf{g}\cdot\mathbf{r}} \tag{3.14}$$

where V_c is the volume of the crystal elementary unit cell, and ^{FT} denotes the Fourier transform, which can be calculated as:

$$\rho_c^{FT} (\mathbf{g}) = \int \rho_c (\mathbf{r}) e^{i\mathbf{g}\cdot\mathbf{r}} d\mathbf{r}. \tag{3.15}$$

Knowing all of this, we can rewrite the expression (3.9) for the scattering amplitude as:

$$E (\mathbf{Q}) = r_{el} C E_i \frac{r^{iKr}}{r V_c} \rho_c^{FT}(\mathbf{g}) \Omega^{FT} (\mathbf{Q}) \tag{3.16}$$

Where $\rho_c^{FT}(\mathbf{g})$ is the Fourier transform of the electron density of atoms belonging to the same elementary unit cell and it involves the structure factor $F (\mathbf{Q})$. In addition, we can introduce the geometrical factor defined as the Fourier transformation of the crystal shape function, $G (\mathbf{Q}) = \Omega^{FT} (\mathbf{Q})$.

3.3 Structure factor

In previous section the structure factor was expressed as (3.15). If the electron density of the atoms in a unit cell is the same as in isolated atoms, and moreover the contribution of a chemical bonds is neglected, we can rewrite this equations as [3]:

$$F (\mathbf{Q}) = \sum_{j=1}^{N} f_j (\mathbf{Q}) e^{-i\mathbf{Q}\cdot\mathbf{r_j}}. \tag{3.17}$$

the value f_j stands for atomic scattering factor, the sum is over the atoms of the same elementary unit cell, and henceforth r_j is the position vector of the j-th atom in the elementary cell.

The structural factor expresses the interference resulting from waves scattered by atoms within the same elementary cell. Under certain specific conditions, waves might interfere destructively causing the structure factor equals zero. This is known as forbidden diffractions. To get selection rules for centered lattices, we need to limit ourselves to a point close to the reciprocal lattice point $\mathbf{Q} \approx \mathbf{g}$. Using equations (3.10), (3.11) and relation between them (3.12), the structure factor around a reciprocal lattice point has the form [3]:

$$F (\mathbf{g}) = \sum_{j=1}^{N} f_j (\mathbf{g}) e^{i2\pi(n_{1j}m_1 + n_{2j}m_2 + n_{3j}m_3)} \tag{3.18}$$

Thanks to this expression, we can derive the selection rules for different types of crystal lattices. For instance, in the case of the diamond structure, wherein silicon and germanium crystallize, only such diffractions that either have all

Laue indices odd or they have all Laue indices even and simultaneously their sum is divisible by four are allowed.

3.4 Geometrical factor

In the previous paragraph the geometrical factor was expressed as Fourier transformations of the crystal shape function, see (3.16)

The geometrical factor has a maximum for a zero argument, and thus the diffraction maximum occurs precisely when the scattering vector is equal to the vector of the reciprocal lattice. This is called Bragg equation in vector form. If we rewrite this equation we get the Bragg equation as:

$$2d_{hkl} \sin \theta_B = \lambda \tag{3.19}$$

where d_{hkl} is the distance between the crystallographic planes, hkl are the Miller indices and $2\theta_B$ is the angle between incident and diffracted beam, see figure 3.1.

Chapter 4

Experimental methods

4.1 Reciprocal space mapping

The study of epitaxial crystal samples is conducted using an x-ray diffraction technique known as reciprocal space mapping. In other words, measuring the dependence of the scattered radiation intensity I on the scattering vector $\mathbf{Q}$. This method is widely used to analyse the strain, relaxation, material composition, and type of defects qualitatively and quantitatively in epitaxial layers, heterostructures and superlattices [16].

The incident wave $\mathbf{k_i}$ and the scattered wave $\mathbf{k_f}$ define the diffraction plane. The experimental setup, where the scattering plane is perpendicular to the sample's surface, is known as coplanar. Otherwise, the arrangement is called

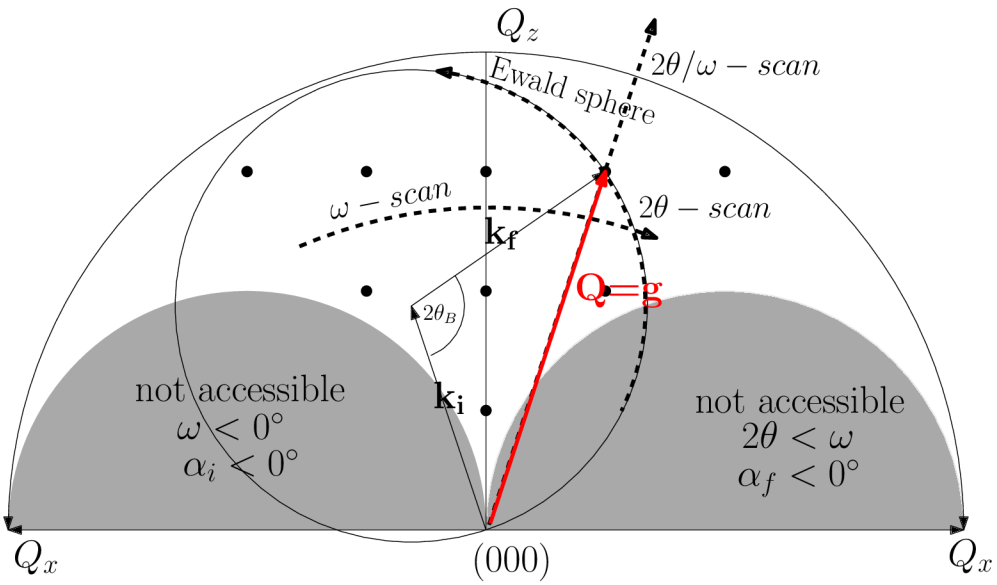

Figure 4.1 The reciprocal space with accessible X-Ray diffractions. Limits for the accessibility of the diffraction reciprocal space are Laue zones ($2\theta < \omega$ and $\omega < 0°$) and the maximal diffractometer angle $2\theta = 4\pi/\lambda$ for CuK_{α_L} is $2\theta = 180$ °. The Ewald sphere construction displays incident $\mathbf{k_i}$ and diffracted $\mathbf{k_f}$ wave vectors. Also the three possible scan directions in reciprocal space are shown, based on [16].

non-coplanar. In the coplanar geometry, the Cartesian system is aligned such that the Q_z axis is practically perpendicular to the sample surface, while the scattering plane lies in the Q_xQ_z plane.

A schematic illustration of such a plane is shown in figure 4.1. The incindent beam $\mathbf{k_i}$ and the scattered beam $\mathbf{k_f}$ are selected to reside in the plane determined by the two crystallographic directions [001] and [110], where [001] is the surface normal and [110] sample edge for cubic structure. There are two limits for accessibility for diffractometric measurements in the Bragg (reflection) geometry - the two small half circles are called Laue zones and have radius $\frac{2\pi}{\lambda}$, and the large half circle with radius $\frac{4\pi}{\lambda}$. The Bragg condition is fulfilled when the scattering vector $\mathbf{Q} = \mathbf{k_f} - \mathbf{k_i}$ equals a reciprocal lattice vector $\mathbf{g}$ [16].

The position of the diffractometer is commonly expressed in angular coordinates ω and $2\theta_B$, where θ_B is the so called Bragg angle from equation 3.19 diffraction condition. ω represents the sample's orientation relative to the incident radiation, while $2 \cdot \theta_B$ denotes the angle between the incident and the scattered beam. Using this two angular coordinates the components of the scattering vector can be calculated as:

$$Q_x = \frac{2\pi}{\lambda} \left(\cos\left(2\theta - \omega\right) - \cos(\omega)\right) \tag{4.1}$$

$$Q_z = \frac{2\pi}{\lambda} \left(\sin\left(2\theta - \omega\right) + \sin\left(\omega\right)\right) \tag{4.2}$$

This equations can be transformed to another by introducing the diffractometer angles α_i, and incident $\alpha_i = \omega$, and the exit angle α_f, which can be expressed as $\alpha_f = 2\theta - \omega$. Using the equations (4.1) and (4.2) we can write:

$$Q_x = \frac{2\pi}{\lambda} \left(\cos\left(\alpha_f\right) - \cos(\alpha_i)\right) \tag{4.3}$$

$$Q_z = \frac{2\pi}{\lambda} \left(\sin\left(\alpha_f\right) + \sin\left(\alpha_i\right)\right). \tag{4.4}$$

Three commonly used scan directions are depicted in figure 4.1. When performing the ω - scan, the angular position of the detector 2θ does not change. We measure the intensity of the scattered radiation depending on the angle of incidence ω. In reciprocal space, the intensity along a circle with radius $Q = 2K \sin\theta$, centered at the origin of reciprocal space, is measured in this case. In order to execute the 2θ - scan, the position of the sample is fixed and only the position of the detector is changing. That means that the angle of incidence does not change, the intensity of the scattered radiation is measured depending only on the angle 2θ. In reciprocal space the intensity along a circle with radius K and centered at the starting point of the vector $\mathbf{k_i}$ is detected. Moreover, the intensity along the Ewald sphere is measured. When conducting $\omega/2\theta$ - scan, the angular position of the detector changes simultaneously with the angle of incidence, but the detector is moved twice as fast as the sample. In the reciprocal space we move along the line given by the scattering vector Q.

Typically, reciprocal space mapping involves performing a series of $\omega/2\theta$ - scans at different ω settings.

4.2 Structural properties by RSM

The process of epitaxial growth on a crystalline substrate introduces strain.This chapter describes the strain analysis approach in expitaxial layer systems. High-resolution X-Ray diffraction is a nondestructive method used to determine the lattice parameters and the strain of epitaxial layers. In this section, we make the assumption that the X-ray beam is highly monochromatic, and we also consider the substrate to be nondeformed. Under these conditions, we can precisely measure the lattice mismatch between the substrate and the strained layer on the relative scale [3].

For partially relaxed systems, two independent measurements are necessary; one to obtain parallel and another to obtain the perpendicular lattice parameter with respect to the surface normal. This can be accomplished by measuring the RSMs of asymmetrical and symmetrical Bragg reflections [3].

While the lattice parameters of the layer a_L and of the substrate a_S may align at crystal growth temperatures, upon cooling the sample towards room temperature, the lattice parameters tend to differ. The resulting lattice mismatch between the lattice parameters was introduced in the chapter 2.1 as equation (2.1).

When the thickness of the substrate significantly exceeds thickness of the layer, the lattice mismatch causes lattice strain solely within the layer. In cases of biaxial strain, such as epitaxy on (001) surface, the non-zero strain components are as follows [3]:

$$\varepsilon_{xx} = \varepsilon_{yy} = \varepsilon_{\parallel} = \frac{a_{L\parallel} - a_L}{a_L}, \tag{4.5}$$

$$\varepsilon_{zz} = \varepsilon_{\perp} = \frac{a_{L\perp} - a_L}{a_L} \tag{4.6}$$

where $\varepsilon_{\parallel}$ is strain parallel and $\varepsilon_{\perp}$ is strain perpendicular to the interface, $a_{L\perp}$ is perpendicular and $a_{L\parallel}$ is parallel lattice parameter of the strained layer.

Using theory of elasticity, a simple conection between $\varepsilon_{\parallel}$ and $\varepsilon_{\perp}$ can be introduced [3]:

$$\varepsilon_{\perp} = -\frac{2C_{12}}{C_{11}}\varepsilon_{\parallel}. \tag{4.7}$$

It is more convenient to express this in terms of the parallel and vertical lattice mismatches (misfits) between the layer and the substrate's lattice parameter, rather than using the strain components [3]. So we introduce misfits as:

$$\delta_{L\perp} = \frac{a_{L\perp} - a_S}{a_S} \tag{4.8}$$

$$\delta_{L\parallel} = \frac{a_{L\parallel} - a_S}{a_S} \tag{4.9}$$

The degree of relaxation can be define as [3]:

$$R = \frac{a_{L\parallel} - a_S}{a_L - a_S}, \tag{4.10}$$

where a_L can be determined from equations (4.6) and (4.7) as:

$$a_L = \frac{C_{11}a_\perp + 2C_{12}a_\parallel}{C_{11} + 2C_{12}}. \tag{4.11}$$

Typically, relaxation assumes values within the interval [0, 1]. If R = 0, the in-plane lattice parameter of the layer is equal to that of the substrate, $a_{L\parallel} = a_S$ and $\delta_{L\parallel} = 0$. This is called the pseudomorphic layer. On the other hand, if R = 1, then the vertical and horizontal lattice parameters are equal, $a_{L\parallel} = a_{L\perp} = a_L$. This is referred to as a fully relaxed layer. If the degree of relaxation exceeds one, $R > 1$, this is denoted as *overrelaxed* layer. This can be a typical case in Ge layers grown on Si due to mismatch in thermal expansion, see section 2.2 [3].

If the layer exhibits a tilt, it is necessary to first adjust the positions of all the layer's symmetrical and asymmetrical diffraction maxima by the degree of tilt before calculating the vertical and horizontal lattice parameters. The tilt of the layer can be calculated as:

$$\phi = \tan^{-1}\left(\frac{Q_{x,max}}{Q_{z,max}}\right) \tag{4.12}$$

where $Q_{x,max}$ is the position of the diffraction maxima in the symmetrical diffraction.

The main topic of this work is to study Ge layers on Si substrate. The position of the Ge diffraction peak of asymmetrical diffraction depends on the degree of Ge relaxation. This is shown schematically in the figure 4.2. If diffraction occurs at pseudomorphic Ge layer, the Q_x-coordinate of the diffraction peak will match that of the Si substrate. On the other hand, when diffraction occurs in a fully relaxed Ge layer, the corresponding peak will be positioned at the intersection of the origin of reciprocal space and the diffraction peak of the Si substrate.

The total tilt of the microcrystals consists of tilts of individual microcrystals and these tilts are completely randomly oriented. The deviation of the growth of the Ge microcrystal from the vertical axis is most probable already given at the beginning of the growth. The tilt of individual microcrystals originates from misfit dislocations at the Si/Ge interface. It is the distribution of the dislocations that determines the direction of Ge microcrystal growth [17].

The line connecting the positions of the diffraction peaks for the fully relaxed and for the pseudomorphic states of the pure Ge layer is known as the relaxation line. It is a set of possible positions of Ge diffraction peaks, each corresponding to different degrees of relaxation.

The coordinates of the maxima in reciprocal space can be used to compute the lattice parameters of the layer. Mapping symmetric and asymmetric diffraction is

essential to determine the lattice parameters in both the lateral and the vertical directions. From the position of the maximum in the symmetric map, the vertical lattice parameter can be calculated as:

$$a_{\perp} = \frac{2\pi l}{Q_{z,max}} \tag{4.13}$$

where l denotes the Miller index and $Q_{z,max}$ stands for the position of the maximum in the symmetrical diffraction. Similarly, the horizontal lattice parameter can be established from the position of the maximum in the asymmetrical diffraction as:

$$a_{\parallel} = \frac{2\pi\sqrt{h^2+k^2}}{Q_{x,max}} \tag{4.14}$$

where h, k are Miller indices and $Q_{x,max}$ denotes the position of the diffraction maximum in the asymmetrical diffraction.

The two relations (4.13) and (4.14) mentioned above are applicable only if the layer exhibits no tilt with respect to the substrate. The tilt of the crystal lattice with respect to the substrate is manifested by the deviation of the symmetrical diffraction maximum from the Q_z axis.

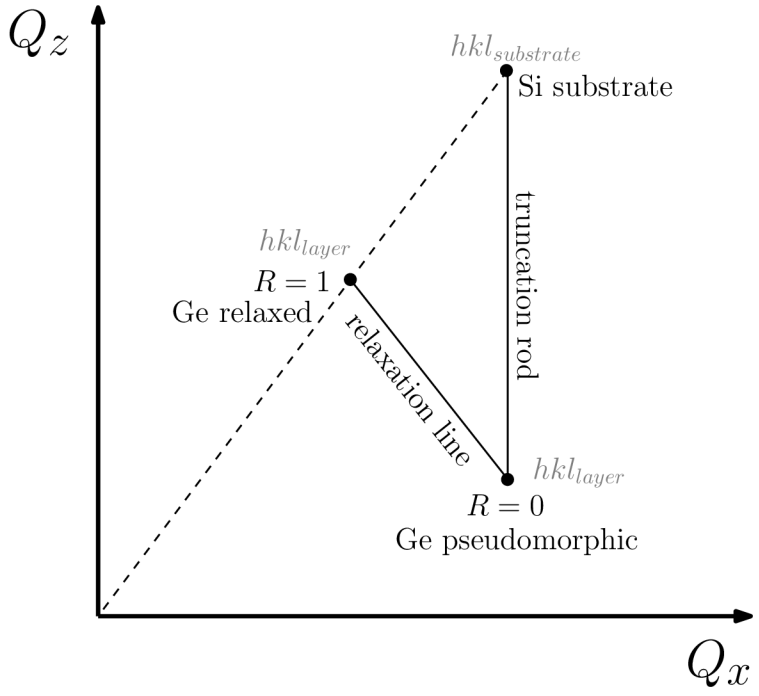

Figure 4.2 The positions of the layer reciprocal lattice point concerning those of the substrate in pseudomorphic and relaxed multilayer systems. It is assumed that $a_{Ge} > a_{Si}$, based on [3].

Chapter 5

Measurement and results

5.1 Experimental set-up

The structural measurements of the samples were performed on Rigaku SmartLab 3kW diffractometer using ultra-high resolution set-up. A schematic illustration of this set-up is depicted in figure 5.1. As an X-ray radiation source, the Cu X-Ray tube with characteristic line Cu$K_{\alpha_1} = 1,54056$ Å was used. The beam from the X-ray tube was initially modified by the Göbel parabolic mirror, where it is partially monochromatized and collimated. The complete monochromatization is achieved using the Bartels monochromator placed behind. The monochromator consists of two germanium crystals in the shape of the letter U, on which four-bounce diffraction (220) occurs. In order to adjust the size of the incident beam, the line slits were used.

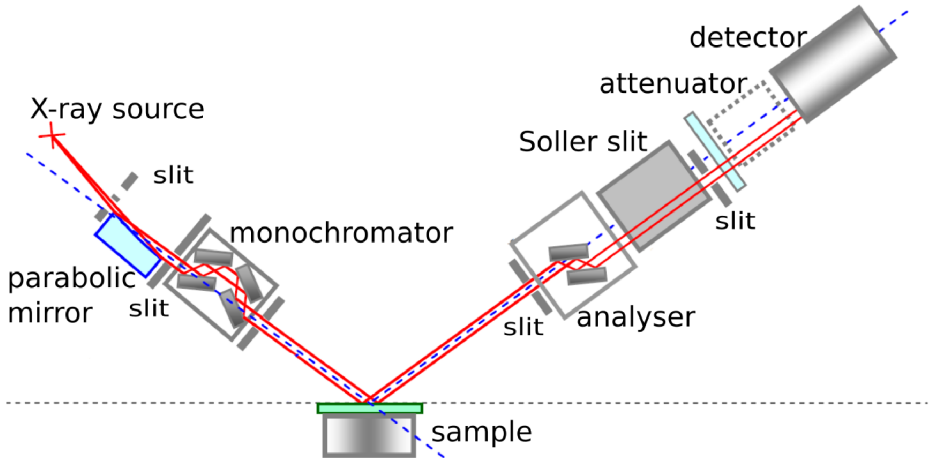

Figure 5.1 A schematic illustration of the set-up used for measurement of the samples, taken from [18].

The beam scattered in the sample, passes through a Ge(220) analyser crystal which is similar to the one in the Bartels monochromator. Therefore, only the two-bounce diffraction occurs on the Ge (220) planes. This analyser is used for measurement in high resolution. Next to the analyser, the 5° Soller slit is also a part of the receiving components of the diffractometer at the detector arm.

The Soller slit is used in order to limit the acceptance of the detector along Q_y direction perpendicular to the scattering plane. As a detector, we use the point scintillation counter SC70.

5.2 About the samples

For this diploma thesis, totally 30 germanium samples having Ge microcrystals grown on Si pillars or ridges with different geometries patterned by etching into the substrate were measured. All the samples were grown in the same manners. Typically the Si pillars with a height of 8 µm are patterned into the substrate. On top of that another 8 µm Si microcrystals were grown at 750°C. Afterwards, the first 100 nm layer of Ge was deposited at high rate at 500°C and as the last 7.9 µm Ge layer was grown at the same temperature at low rate. The total height of the microcrystals was 16 µm. The crystallographic orientation (001) of the Si substrate surface was the same for all of the studied samples.

Regarding the substrate patterning, we have two distinct sample groups, all labeled with a combination of letters and numbers. The first group contains square-based pillars, as shown in figure 5.2. These differ in the size of the pillar base (P) and the trenches (T) between them. The letter denotes the gap size, ranging from 1 µm labeled as A up to 50 µm denoted by F. The number represents the size of the square base with only three possibilities: 2 for 5 µm, 3 for 9 µm, and 4 for 15 µm.

The second group consists of ridges, depicted in figure 5.3. Similarly, the letter denotes the width of the ridges, available in 1 µm, 2 µm, and 3 µm values. Regarding the trench size, there are only two options of the width: 2 µm or 5 µm. One difference for ridges compared to pillars is the two orientation possibilities of the ridges. It can be either parallel to sample edge (110) direction or oriented from the sample edge at a 45° angle.

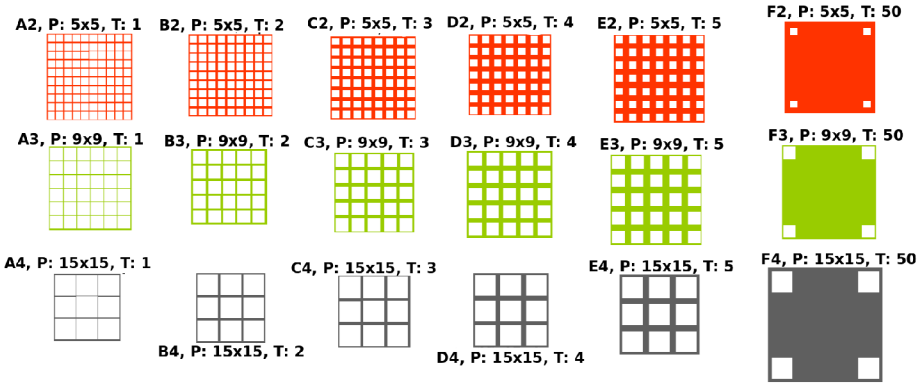

Figure 5.2 The samples patternings for pillars are shown. The letters stands for the gap size, while the numbers represent the pillar size. The first number in the sample label is pillar size and the second trench width.

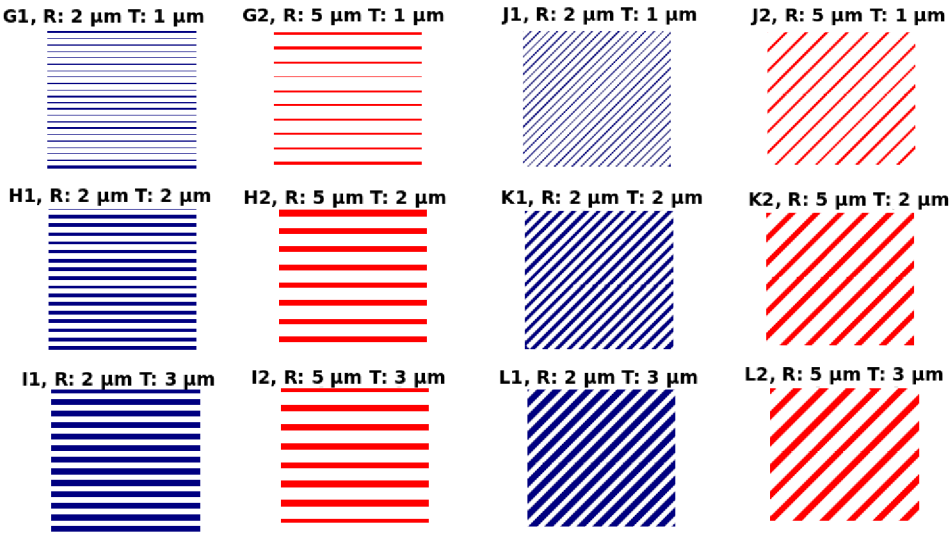

Figure 5.3 The samples patternings for the ridges are shown. The letters stands for the trench size (T), while the numbers represent width of the ridges (R). The first number in sample label is width of ridges and the second one is trench size.

5.3 Examples of a reciprocal space maps

In this section, we will illustrate the overall output of a single sample measurement. Afterwards, we will individually analyse the measured data for all samples categorized by the pillar size. This analysis will be performed separately for symmetrical (004) and asymmetrical (224) or (404) diffractions.

The reciprocal maps shown in figures 5.4 and 5.5 are divided into four distinct sections. The symmetrical diffraction maxima are located on the left and asymmetrical ones on the right. The upper one is for the azimuth 0° and the bottom one for 90°. Due to the larger lattice parameter of Ge, the Ge diffraction maxima lie at the bottom of figure, closer to the origin of the coordinates and the diffraction maxima from Si substrate are above them.

Diffractions for the Si substrate were measured only for the possibility of sample alignment correction. The Si substrate is made of high-quality single crystal of sufficient size. Therefore, it can be used as reference bulk and the maximum will surely lies on the coordinates calculated in the equations (4.1) and (4.2). If the measured maxima of the Si substrate deviate from the calculated coordinates, the correction is necessary. This can be done by moving the origin of the coordinate system so that the measured diffraction maximum corresponds to the calculated one.

As an example, the results for the sample B4 will be discussed. This sample has a pillar pattern with the base size of 15x15 µm and the trench size is 2 µm. The total height of the microcrystals is 16 µm. In figure 5.4 the measured maxima of the substrate and of the layer for symmetrical (004) and asymmetrical (224) diffractions for azimuths 0° and 90° are shown. In table 5.1 all the

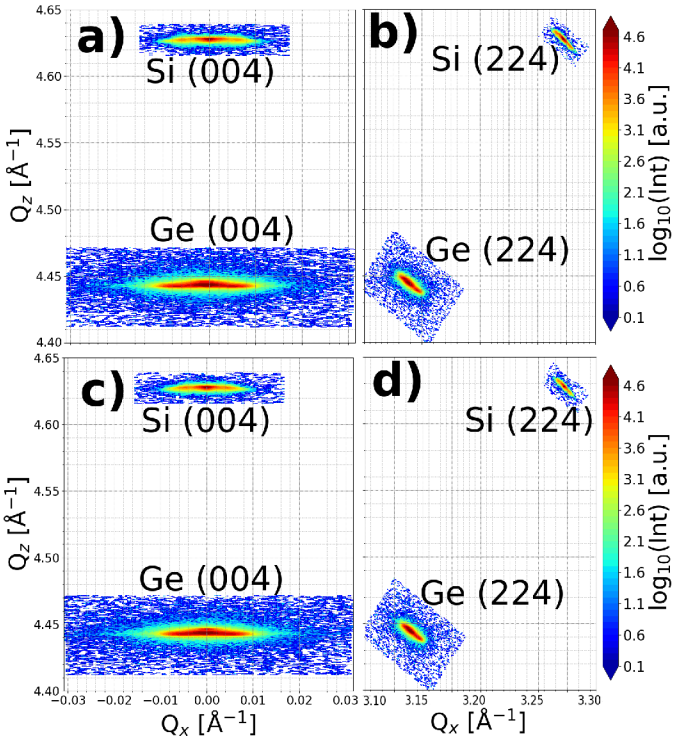

Figure 5.4 Measured reciprocal space map for sample B4 at 0° (a,b) and 90° (c,d) azimuth. The symmetrical (004) diffractions are on the left (a,c) and the asymmetrical (224) diffractions are on the right (b,d).

Table 5.1 Calculated parameters for sample B4 in two different azimuths, 0° and 90°.

	azimuth 0°	azimuth 90°
tilt[°]	-0.0068 ± 0.0001	-0.0036 ± 0.0001
$a_\perp$[Å]	5.6561 ± 0.0004	5.6561 ± 0.0002
$a_\parallel$[Å]	5.6602 ± 0.0007	5.6605 ± 0.0007
$\delta_\perp$[%]	4.120 ± 0.007	4.143 ± 0.004
$\delta_\parallel$[%]	4.244 ± 0.005	4.225 ± 0.005
$\epsilon_\perp$[%]	-0.04 ± 0.01	-0.03 ± 0.01
$\epsilon_\parallel$[%]	0.05 ± 0.02	0.05 ± 0.02
R	1.01 ± 0.01	1.01 ± 0.01

parameters calculated from the peak positions are presented. Lattice parameters from the positions of the main diffraction peaks of the symmetrical (004) and the asymmetrical (224) diffraction were determined using equations (4.13) and

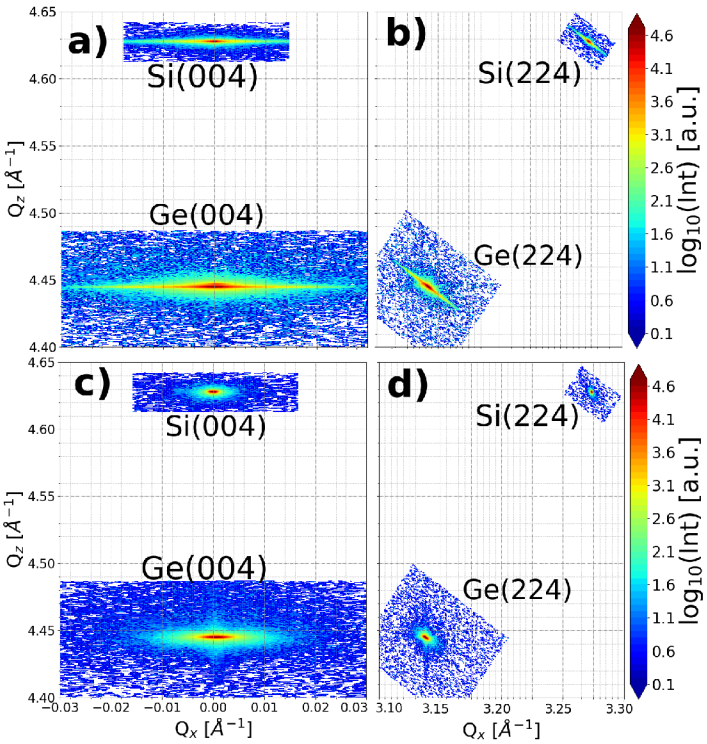

Figure 5.5 Measured reciprocal space map for sample I1 at 0° azimuth (a,b) perpendicular to ridges and 90° azimuth (c,d) parallel to the ridges. The symmetrical (004) diffractions on the left (a,c) and the asymmetrical (224) diffractions on the right (b,d).

(4.14). In addition, a tilt was determined from the symmetrical map using an equation (4.12). The tilt was used for rotation of the Ge layer peak in the asymmetrical map (224) as well. Afterwards, it was possible to calculate all the other parameters using the equations from section 4.1. We are using the elastic constants for pure Ge as $C_{11} = 124$ GPa and $C_{12} = 41$ GPa [4]. If we compare the resulting parameters for both azimuths, see table 5.1, it is evident that they are nearly identical, primarily due to the four-fold symmetry of the pillars. The symmetry arises from the microcrystals having a square base. Rotating the sample by 90° alters the orientation of the patterned substrate, but the overall symmetry of the pillar geometry remains unchanged. Thus we will show the results solely for the azimuth 0°, although the reciprocal maps were measured for both azimuths for all samples.

However, the symmetry only applies to samples with the pillar base. If we look at the example for the ridge sample in figure 5.5, we will see several differences. The sample I1 was used to demonstrate these differences. The substrate patterning of this sample is composed of ridges oriented along [110], with the width of 2 µm and the size of the trenches is 3 µm. In figure 5.5 the maxima for the symmetrical (004) and the asymmetrical (224) diffractions are shown. Parts (a, b) depict the reciprocal space maps at the 0° azimuth, when

Table 5.2 Calculated parameters for sample I1 in two different azimuths, 0°, perpendicular to the ridges and 90° parallel to the ridges.

	azimuth 0°	azimuth 90°
tilt[°]	0.0071 ± 0.0002	-0.0011 ± 0.0001
$a_\perp$[Å]	5.654 ± 0.001	5.6541 ± 0.0008
$a_\parallel$[Å]	5.664 ± 0.003	5.6555 ±0.0004
$\delta_\perp$[%]	4.11 ± 0.02	4.106 ± 0.007
$\delta_\parallel$[%]	4.29 ± 0.01	4.133 ± 0.009
$\epsilon_\perp$[%]	-0.076 ± 0.004	-0.01 ± 0.03
$\epsilon_\parallel$[%]	0.10 ± 0.02	0.015 ± 0.007
R	1.03±0.02	1.00±0.01

the scattering plane is perpendicular to the ridges. On the other hand, (c, d) represent those at the 90° azimuth with the scattering plane parallel to the ridges. Comparing these maps, see figure 5.5 for the two azimuths reveals a significant difference in the maxima's shapes. From the positions of the diffraction maxima the parameters can be calculated in a similar way as for the sample B4, shown in table 5.2. Whereas B4 exhibited almost identical parameters for both azimuths, the sample I1 shows noticeable differences. This is because the ridges are no longer symmetrical and therefore exhibit distinct properties for different azimuths. We will discuss these differences later.

5.4 Pillars with the same base

Firstly, the results for pillar-based samples will be discussed. We will categorize them based on the pillar size and proceed to compare them. Analyzing the shape of their diffraction maxima and the derived parameters obtained from their positions will be our next steps.

5.4.1 X2 series, base 5×5 μm

This section investigates six samples with the common base size of 5×5μm, differing only in the trench sizes: 1μm, 2μm, 3μm, 4μm, 5μm, and 50μm. The images of these samples captured using the Zeiss 2E optical microscope are depicted in figure 5.6.

In figure 5.7, the symmetrical diffraction maxima (004) for all the samples from X2 serie are illustrated. With the exception of the samples A2 and B2, the distinct pair of peaks is observed. The two maxima correspond to the different sections of the Ge layer. The main maxima correspond to the relaxed Ge on the

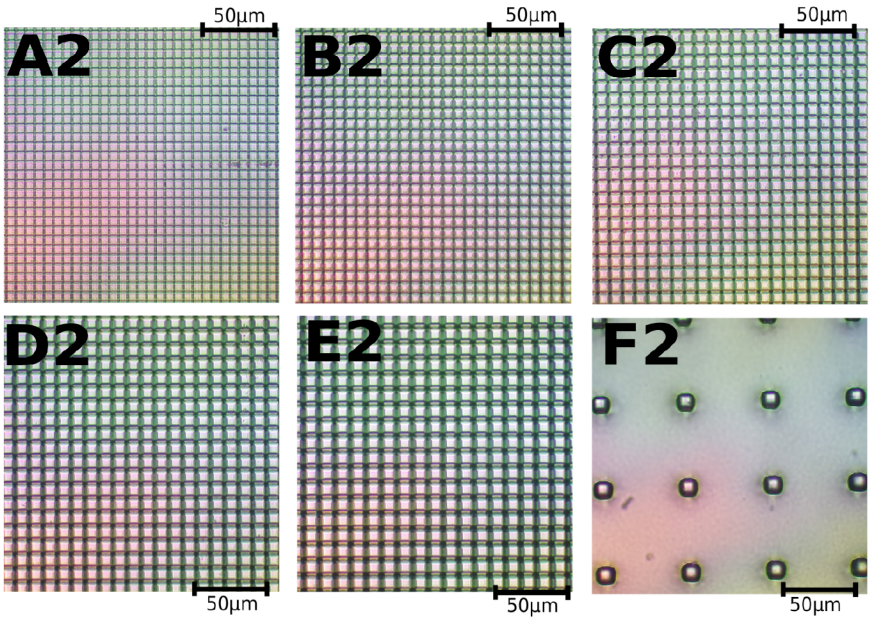

Figure 5.6 Photos of samples with the same size of the base 5×5µm, differing in the trench size. Images taken with Zeiss 2E optical microscope.

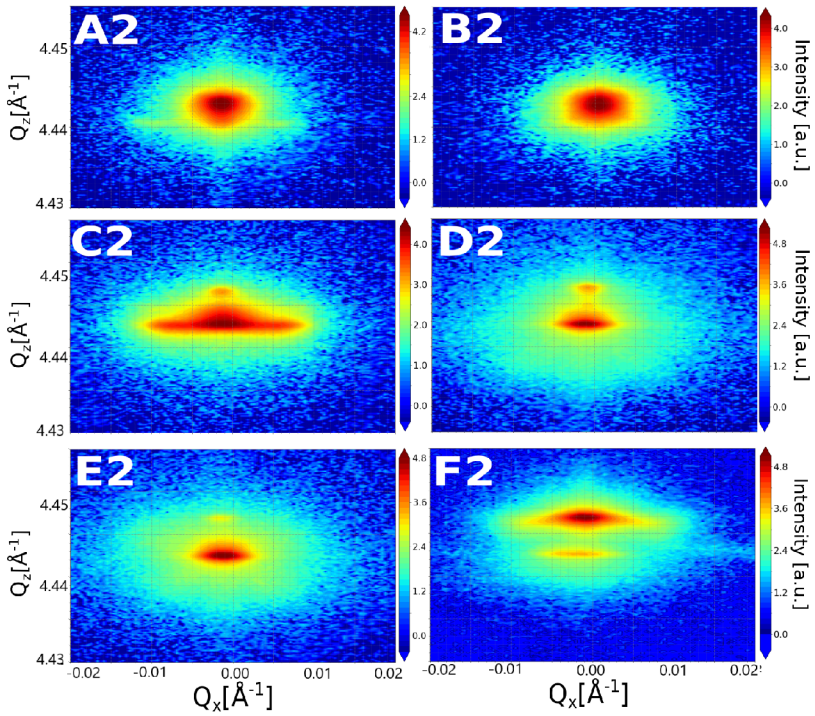

Figure 5.7 Reciprocal space maps around the symmetrical (004) diffraction on the Ge microcrystals

top of the Si pillars. However, Ge was deposited also in the space between Si pillars and the secondary maxima are a result of this. This material is strained and cannot elastically relax [9].

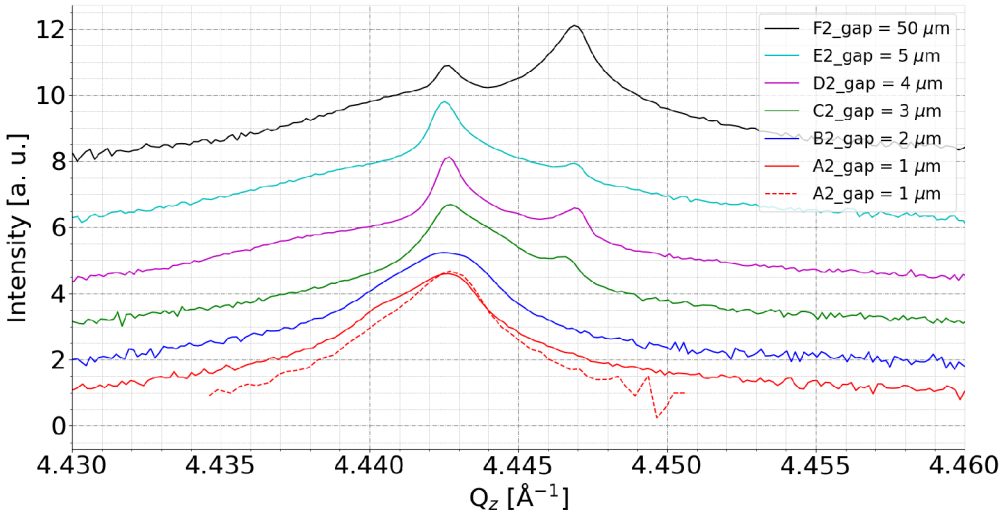

Figure 5.8 Cross-sections through the Ge (004) along Q_z for the sum of the Q_x from −0.1 to 0.1 Å for samples from X2 series. Dotted red line for the sample A2 is an example of the cross-section for Q_x =0

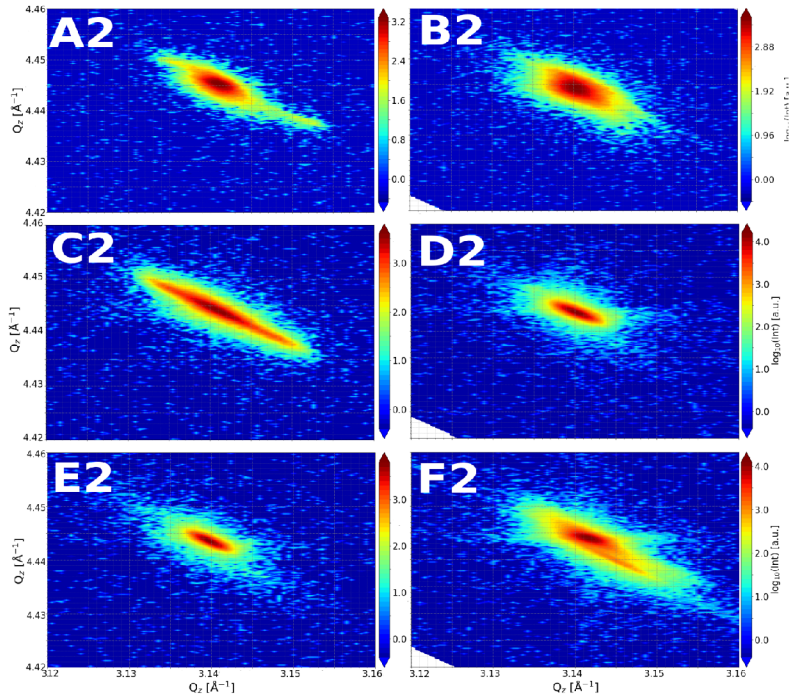

Figure 5.9 Reciprocal space maps around asymmetrical (224) diffraction on Ge micro-crystals

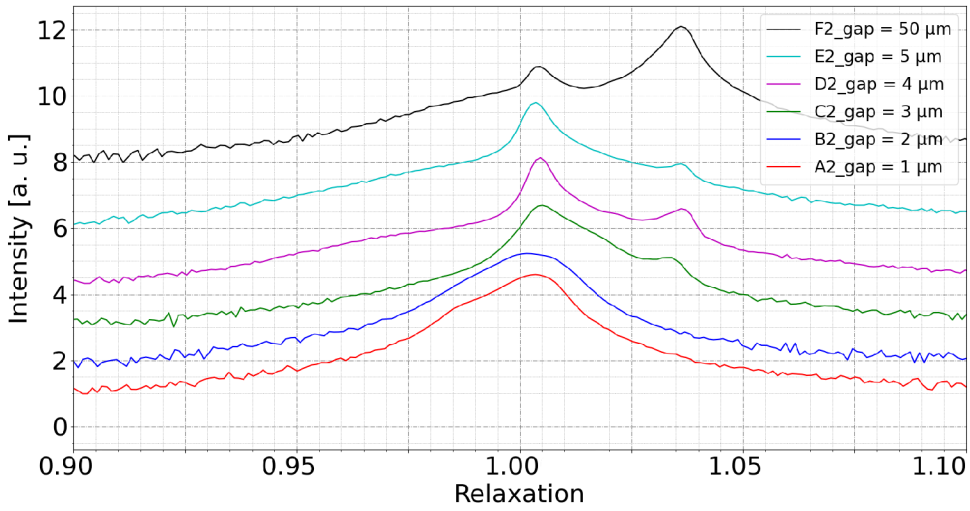

Figure 5.10 Calculated relaxation from cross-sections of symmetrical diffraction (004) for samples from the X2 series.

The sample F2 is little bit different than the others. It is lightly patterned, resulting in the small number of pillars that are 50 µm apart. Consequently, more material is deposited between the Si pillars compared to the material deposited directly on them, leading to a stronger signal from the diffraction maxima from the bottom material. Samples C2 and A2 have also satellite maxima presented as the elongation along Q_x direction. It was assumed that these maxima arise from the thermal bowing of the lattice [13, 17]. In this diploma thesis, we will investigate the possibility that the elongation in Q_x direction may originate also from the cracks edges. These cracks will appear if the certain number of microcrystals merge together during the growth along the sample [11]. This will be discussed more later.

Table 5.3 Calculated lattice parameter for the Ge microcrystals using the equation (4.11). The diffraction maxima correspond to the pure Ge.

Sample	a_L[Å]
A2	5.6579 ± 0.0002
B2	5.6576 ± 0.0003
C2	5.6576 ± 0.0004
D2	5.6575 ± 0.0005
E2	5.6569 ± 0.0005
F2	5.6579 ± 0.0001

For better clarity of the positions of the diffraction maxima, we will use cross-sections through the Ge (004) peak obtained as sum over (-0.1, 0.1), shown

in figure 5.8. The graph illustrates that the position of the diffraction peak, representing the lattice parameter of relaxed Ge, remains consistent regardless of the Ge microcrystals coverage. On the other hand, the position of the diffraction maxima, which corresponds to the strained Ge slightly changes for individual samples. For sample F2, we again see that the peak intensity is at lower Q_z since the amount of the microcrystals with relaxed Ge is smaller than the amount of strained Ge in the trenches.

When comparing the diffraction peaks in these two cross-sections, there is no visible difference in the width, although it might appear so from the the reciprocal maps. This is due to the fact that the cross-sections were made as a sum of intensities along Q_z for Q_x taken from -0.1 to 0.1. The intensity values are the sum over the entire peak, and therefore the cross-sections appear almost identical. For comparison, we added the cross-section through Q_z for $Q_x = 0$ to figure 5.8 as dotted red line for sample A2. We can see that the peak is narrower and the peak corresponding to the satellite maxima is not visible.

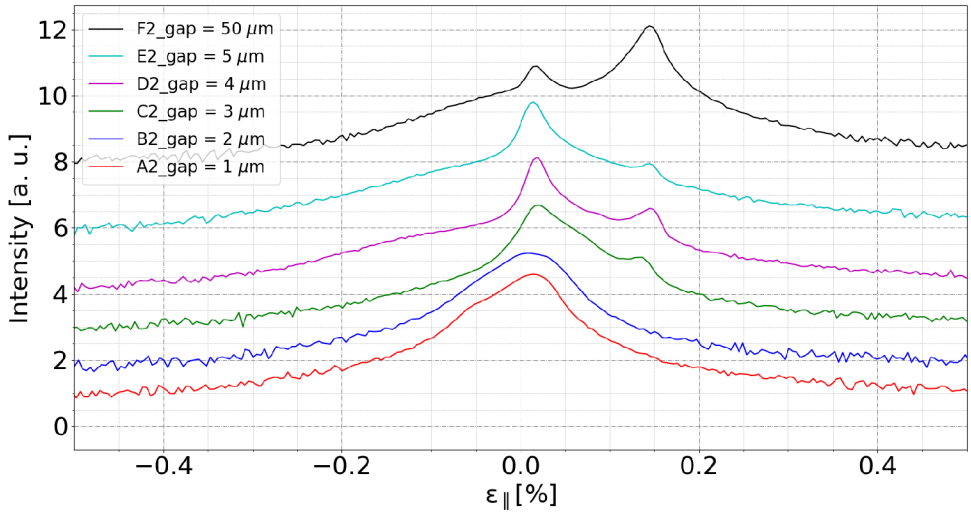

Figure 5.11 Calculated parallel component of the strain $\epsilon_{\parallel}$ tensor from cross-sections of the symmetrical diffraction (004) for samples from the X2 series.

In order to compute all the parameters, it is necessary to measure the asymmetrical (224) diffraction as well. Unfortunately, due to the weak scattered intensity and due to the partial overlap of the peaks, there is an increased uncertainty in determining the accurate position of the secondary peak originating from trenches. In figure 5.9, it is apparent that the precise position of the secondary maximum cannot be determined well for most of the samples. When examining the sample F2, we clearly observe two peaks. The more intense peak corresponds to the material in the trenches, while the weaker one with the smaller Q_z value corresponds to the relaxed material on the Si pillars, similar to what was observed in the case of symmetrical (004) diffraction.

From the knowledge of the positions of the symmetrical and the asymmetrical

diffraction maxima, we can calculate the lattice parameters in the lateral and the horizontal directions using the equations (4.13) and (4.14). Subsequently, the degree of relaxation can be calculated using the formula (4.10). These results, together with the components of the stress tensor, are presented in table in A.1 for relaxed Ge and in table A.4 for strained material in trenches in A part of appendix. For the secondary maxima, the parameters were determined only for the samples where this peak clearly appeared in the symmetrical diffraction. Subsequently, a rough estimate was made for the peak position in the asymmetrical diffraction (224).

Table 5.4 Parameter values obtained from the Q_x cross-sections for the main maxima for X2 samples.

Sample	R	$\epsilon_{\parallel}[\%]$	$\epsilon_{\perp}[\%]$
A2	1.003 ± 0.001	0.015 ± 0.009	− 0.014 ± 0.006
B2	1.003 ± 0.009	0.014 ± 0.007	− 0.012 ± 0.007
C2	1.004 ± 0.002	0.020 ± 0.009	− 0.015 ± 0.004
D2	1.005 ± 0.004	0.020 ± 0.005	− 0.016 ± 0.008
E2	1.003 ± 0.002	0.015 ± 0.004	− 0.012 ± 0.005
F2	1.004 ± 0.001	0.017 ± 0.008	− 0.016 ± 0.005

Table 5.5 Parameter values obtained from the Q_x cross-sections for the secondary maxima for X2 samples.

Sample	R	$\epsilon_{\parallel}[\%]$	$\epsilon_{\perp}[\%]$
C2	1.034 ± 0.002	0.134 ± 0.009	− 0.102 ± 0.004
D2	1.037 ± 0.004	0.145 ± 0.005	− 0.110 ± 0.008
E2	1.036 ± 0.002	0.146 ± 0.004	− 0.110 ± 0.005
F2	1.036 ± 0.001	0.144 ± 0.008	− 0.112 ± 0.005

However, we can notice that the uncertainty of the individual lattice parameters is quite large. For example, the statistical uncertainty of the relaxation parameter is larger than the deviation of mean relaxation from 1, which is our main interest. So we decided to take an alternative method to calculate the relaxation. First, we calculate the lattice parameter of the layer for all samples from the X2 series using the formula (4.11). We do this in order to show that the microcrystals are composed of the pure Ge. Table 5.3 demonstrates that all obtained values are aligned closely with the nominal value of a_L =5.6579Å [4]. So we can really assume that the deposited material consists of 100% Ge. Taking this into account, we derive the formula for the horizontal lattice parameter using the pure Ge lattice parameter and the equations (4.5) and (4.7):

$$a_{L\parallel} = \frac{C_{11}}{2C_{12}} (a_L - a_{L\perp}) + a_L \tag{5.1}$$

where $a_{L\perp}$ is determined from the reciprocal space map of the symmetrical diffraction maximum (004) and a_L is the nominal value of lattice parameter for

the Ge layer. Now we use the relation (4.10) to calculate the relaxation R using $a_{L\parallel}$ from the equation (5.1):

$$R = 1 + \frac{C_{11}}{2C_{12}} \frac{(a_L - a_{L\perp})}{a_L - a_S} \tag{5.2}$$

This equation was also used to convert the Q_x-axis in the graph 5.8 for cross-sections through the Ge (004) into the relaxation R. The resulting relaxation is shown in figure 5.10. From this graph, we are only interested in the relaxation values for the peaks. We can see that while the relaxation values in the A part of appendix in table A.1 are looking almost random, we get more consistent results for the peak positions in this plot, see table 5.4 for main the Ge peak and table 5.5 responding to the secondary peak. From this we can conclude that while the main maxima really come from the pseudo-continuous Ge layer, which is relaxed, the secondary maxima come from the different parts of the microcrystals, which is overrelaxed. For the secondary maxima, the relaxation parameters are shown only for the samples C2-F2, because diffraction maps for the samples A2 and B2 do not have a visible secondary peak.

Using the equations (4.5) and (5.1), it is also possible to convert the Q_z coordinate to the parallel component of the strain tensor $\epsilon_{\parallel}$ as:

$$\epsilon_{\parallel} = -\frac{2C_{12}}{C_{11}} \frac{a_{L\perp} - a_L}{a_L} \tag{5.3}$$

To obtained the perpendicular component of strain $\epsilon_{\perp}$ the equation (4.7) was used. The main maxima results are presented in table 5.4 and for the secondary maxima see table 5.5. While the relaxed layer shows a tension in hundredths of a percent, results from the secondary maximum are slightly higher.

5.4.2 X3 series, base 9×9 μm

In this section, we will examine the results of the measurement for the samples with the base 9×9 μm and the different trench sizes. Photos of the investigated samples are in figure 5.12.

In figure 5.13 the symmetrical Ge (004) reciprocal space maps for the various trench sizes are shown. The presence of the secondary maxima in the reciprocal space maps is visible, except for samples A3 and B3. The overlap with the main maxima probably occurred, or the trenches were not yet large enough for a significant amount of material to be deposited between the pillars and to be visible in RSM. The secondary maxima are larger in their size and have even higher intensity then in the X2 series. For the sample F3, the stronger maximum corresponds to the material deposited between the pillars, while the weaker peak originates from the relaxed Ge microcrystals grown on Si pillars. The diffusion scattering is extremely strong in the sample B3. This may be related to the merging of pillars and subsequent formation of cracks, as was mentioned also for the samples A2 and C2.

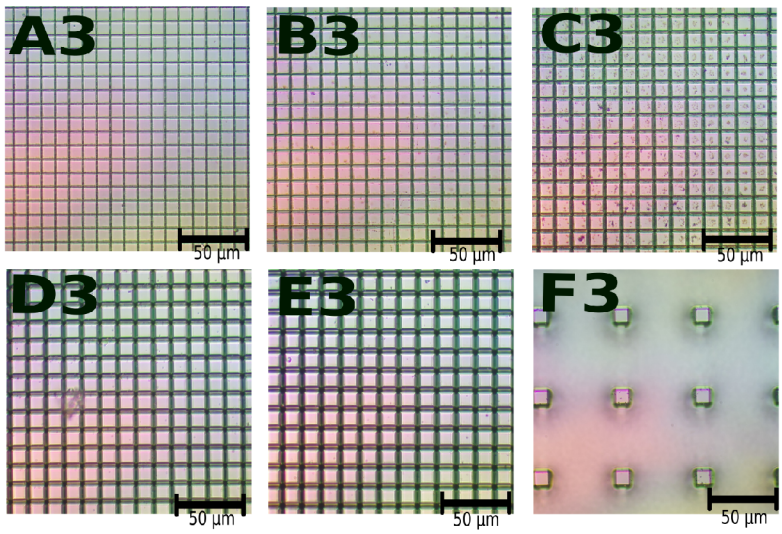

Figure 5.12 Photos of X3 serie samples with the same size of the base, differing in the trenches. Images taken with Zeiss 2E optical microscope.

For a better understanding of the shape of the individual maxima, the cross-sections through the Ge maximum of the symmetrical diffraction (004) along Q_z for various Q_x taken as sum from -0.1 to 0.1 Å were plotted in figure 5.14.

We also measured the asymmetrical diffraction (224) for samples from the X3 series, see figure B.1 in the appendix B. The symmetrical 5.13 and the asymmetrical B.1 maps, were used to calculate the parameters listed in table A.1 in appendix A. Table A.1 reveals that the results obtained using this method appear quite random and have a large uncertainty. Therefore, we will also choose another approach presented in the previous section to obtain the resulting parameters. For this series of the samples, we also assuming pure Ge contents.

After verifying that the deposited layer can be considered as pure germanium by calculating the lattice parameter using equation (4.11), we calculated the parameters by converting the Q_z coordinate. Firstly, the relaxation R was determined using the equation (5.1) and then in-plane $\epsilon_{\parallel}$ and perpendicular $\epsilon_{\perp}$ components of strain tenzor were established applying the equations (5.2) and (5.3). All the resulting parameters are shown in table 5.6 for the main maxima, and in table 5.7 for the secondary maxima. Comparing these two tables affirms the earlier conclusion. The material deposited on the pillars, to which the main maxima correspond, is relaxed. Since the relaxation R values differ from 1 up to the third decimal place, the Ge microcrystals are only slightly overrelaxed. In addition, this material exhibits minimal strain, in the hundreds of percent. On the other hand, the material desposited between the pillars, see the secondary maxima, is overrelaxed. Moreover, this material exhibits the strain, with the both components of the strain tensor ranging in the tenths of percent.

Another interesting observation is the sign of the strain tensor components.

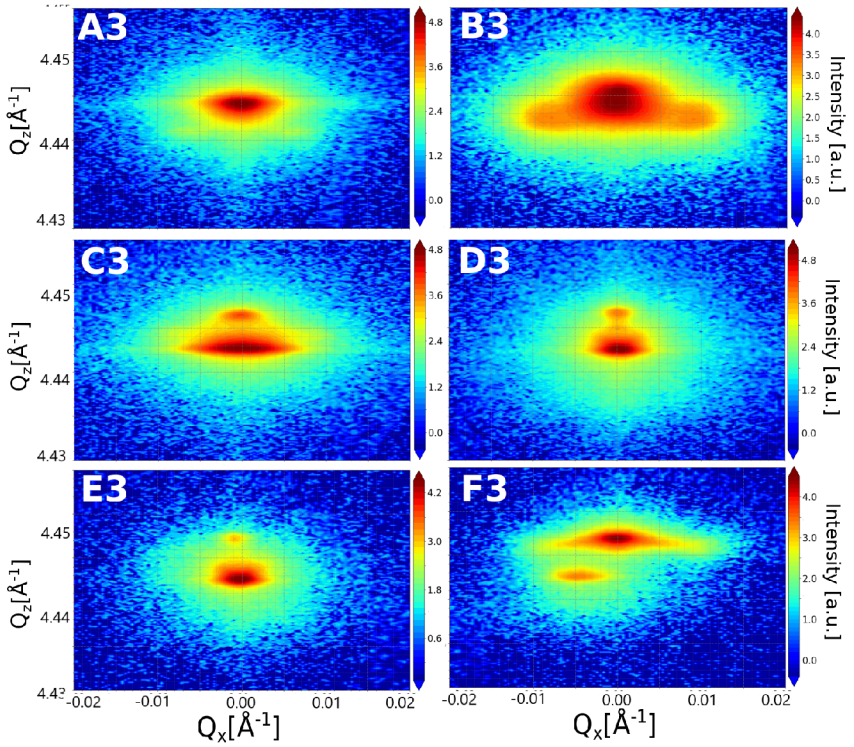

Figure 5.13 Reciprocal space maps around the symmetrical (004) diffraction on the Ge layer of the samples from X3 series.

While the in-plane component is positive, the vertical component is negative. This means that the lattice parameter of the layer lengthens in the direction parallel to the surface, while it shortens in the perpendicular direction. This is caused by different thermal expansion coefficients of Si and Ge.

Table 5.6 Parameter values obtained from the Q_z cross-section for the main maxima for X3 samples.

Sample	R	$\epsilon_{\parallel}[\%]$	$\epsilon_{\perp}[\%]$
A3	1.003 ± 0.001	0.019 ± 0.009	− 0.020 ± 0.006
B3	1.003 ± 0.009	0.020 ± 0.007	− 0.020 ± 0.007
C3	1.004 ± 0.002	0.019 ± 0.009	− 0.016 ± 0.004
D3	1.004 ± 0.004	0.016 ± 0.005	− 0.013 ± 0.008
E3	1.003 ± 0.002	0.012 ± 0.004	− 0.010 ± 0.005
F3	1.004 ± 0.001	0.013 ± 0.008	− 0.010 ± 0.005

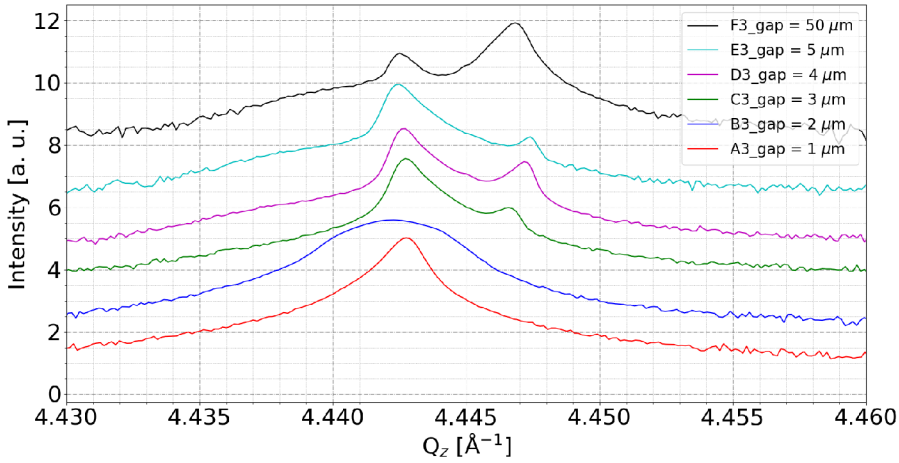

Figure 5.14 Cross-sections through the Ge (004) along Q_z as the sum of Q_x taken from −0.1 to 0.1 Å for samples from X3 series.

Table 5.7 Parameter values obtained from the Q_z cross-section for the secondary maxima for X3 samples. Samples A3 and B3 have no visible secondary maxima.

Sample	R	$\epsilon_{\parallel}[\%]$	$\epsilon_{\perp}[\%]$
C3	1.034 ± 0.001	0.136 ± 0.004	− 0.102 ± 0.003
D3	1.038 ± 0.002	0.153 ± 0.003	− 0.115 ± 0.004
E3	1.040 ± 0.001	0.160 ± 0.006	− 0.120 ± 0.003
F3	1.036 ± 0.001	0.143 ± 0.004	− 0.108 ± 0.001

5.4.3 X4 series, base 15×15 μm

As the last, we investigate square-based microcrystals the samples with pillars having the 15 μm edge size and the different trenches. Photos of the surface of the samples are in figure 5.15.

In figure 5.16 the symmetrical (004) diffraction maxima around Ge are depicted. In this case, the secondary maximum is observable even in sample B4, implying that the diffraction peak originating from the material between the Si pillars is absent only for the sample A4. For the sample F4, similar observations apply as in the other samples having a 50 μm gap. The maximum with the higher Q_z coordinate and larger intensity corresponds to the material in the trenches, while the the maximum closer to the origin coordinates corresponds to the material deposited on the Si pillars. The satellite maxima are clearly visible for samples A4 and B4. From the reciprocal maps it is apparent that these satellite maxima exhibit a greater tilt compared to the primary and secondary maxima. Additionally, it is evident that they are symmetrical. Their presence in the diffraction maps is probably caused by cracks and will be discussed later.

In figure 5.17 the cross-sections of the maxima of the symmetrical diffraction (004) for X4 samples taken as a sum for -0.1 to 0.1 in Q_x are displayed. First

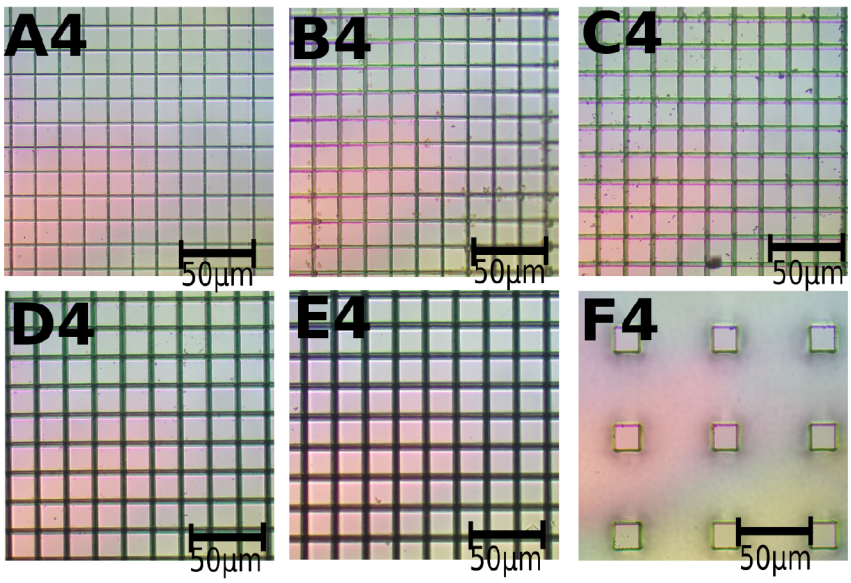

Figure 5.15 Photos of samples from X4 with the same size of the base, differing in the trenches. Images taken with Zeiss 2E optical microscope.

of all, we notice the unusual shape of the cross-section for A4 sample, which was not so evident on the diffraction map. In the cross-section, a double peak is apparent and its position and intensity differs from the other samples as we would expect. The peak associated with relaxed Ge appears smaller, while the more intense peak indicates the strain and over-relaxation. However, it is not located at the position of the secondary maxima as in the other samples. In addition, the broader peak can be seen for the sample B4 as well. Both of these phenomena will be more commented later.

Table 5.8 Parameter values obtained from the Q_z cross-section for the main maxima for X4 samples.

Sample	R	$\epsilon_{\parallel}[\%]$	$\epsilon_{\perp}[\%]$
A4	1.005 ± 0.007	0.022 ± 0.008	-0.013 ± 0.009
B4	1.006 ± 0.004	0.027 ± 0.002	-0.018 ± 0.003
C4	1.005 ± 0.002	0.020 ± 0.003	-0.016 ± 0.001
D4	1.005 ± 0.003	0.020 ± 0.001	-0.015 ± 0.002
E4	1.006 ± 0.001	0.021 ± 0.002	-0.015 ± 0.004
F4	1.005 ± 0.003	0.023 ± 0.002	-0.016 ± 0.001

We used the same method as in the previous sections in order to recalculate the cross-section values from Q_z into the relaxation value R using the expression (5.1), in-plane strain $\epsilon_{\parallel}$ using the equation (5.2) and the vertical strain $\epsilon_{\perp}$ using the formula (5.3). The resulting parameter values are shown for the main maxima

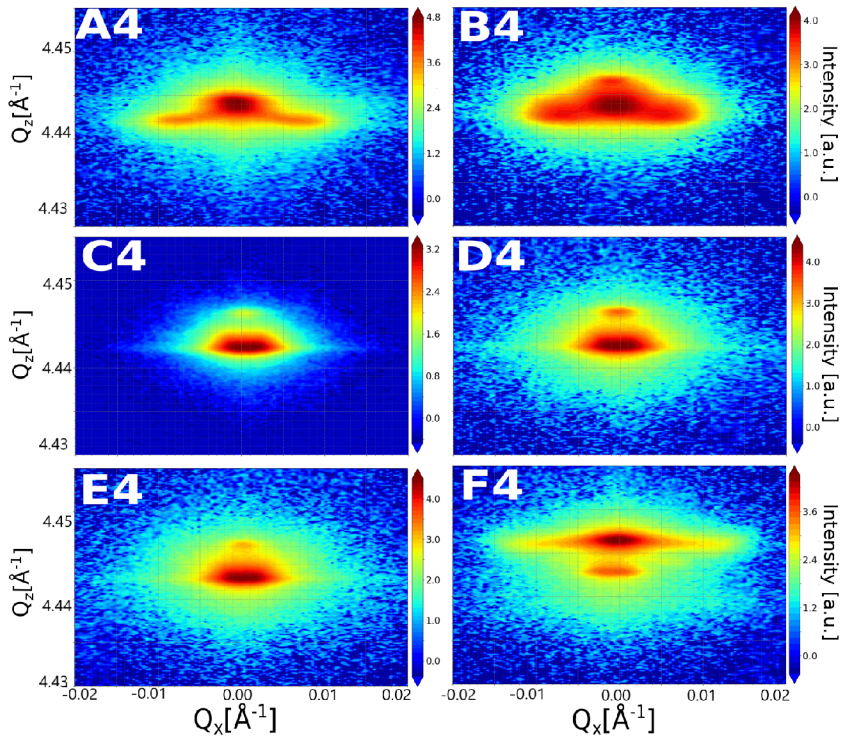

Figure 5.16 Reciprocal space maps around the symmetrical (004) diffraction on the Ge layer of samples from X4 serie.

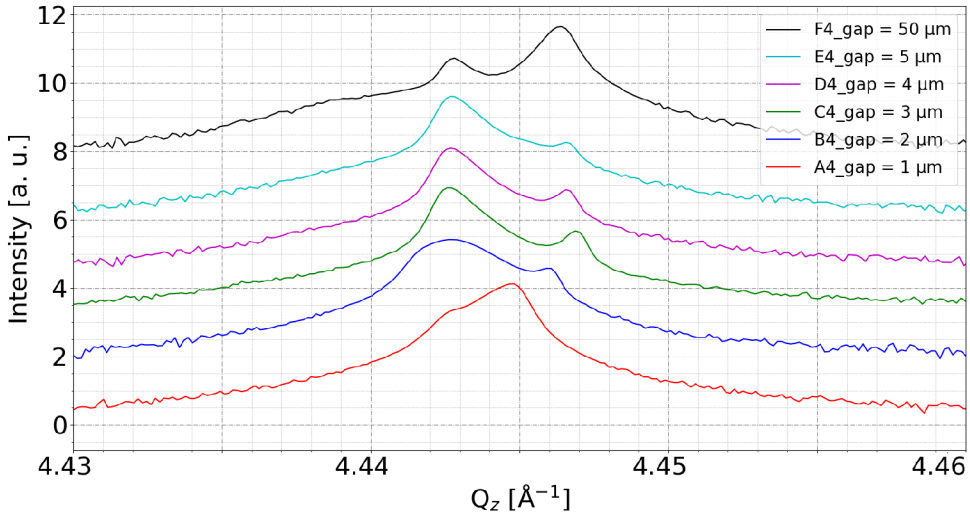

Figure 5.17 Cross-sections through the Ge (004) along Q_z as the sum of Q_x taken from -0.1 to 0.1 Åfor samples from X3 series.

in table 5.8 and for the secondary maxima in table 5.9. For the sample A4, the parameters for the main maximum are calculated from the peak at the position corresponding to the relaxed layer, i.e. from the less intense peak.

Table 5.9 Parameter values obtained from the Q_z cross-section for the secondary maxima for X4 samples.

Sample	R	$\epsilon_{\parallel}$[%]	$\epsilon_{\perp}$[%]
A4	1.022 ± 0.002	0.085 ± 0.01	− 0.053 ± 0.02
B4	1.032 ± 0.002	0.13 ± 0.01	− 0.09 ± 0.02
C4	1.038 ± 0.001	0.15 ± 0.01	− 0.11 ± 0.01
D4	1.035 ± 0.003	0.14 ± 0.02	− 0.10 ± 0.02
E4	1.034 ± 0.001	0.14 ± 0.01	− 0.10 ± 0.01
F4	1.032 ± 0.001	0.13 ± 0.01	− 0.10 ± 0.01

The parameters for the secondary maximum are then calculated from the more intense peak from the position for the more strained layer. For these samples, we also clearly see the extension of the peak in the Q_x direction. We assume that in this case it is caused by cracks that arise during the growth of the microcrystals by the merging of a certain number of microcrystals, as in previous sections.

We will now compare the outcomes in these tables with those from Appendix **??**, derived using the asymmetrical diffraction maps, see figure **??** in Appendix B. The results obtained from the asymmetrical maps exhibit notably higher measurement uncertainty, especially evident in relaxation R values, where the uncertainty range closely aligns with the deviation from 1. This issue is not present in parameters obtained from the Q_z cross-section graph in figure **??**. Strain tensor components calculated from the reciprocal space maps show varied values with considerable uncertainty. On the other hand, values in tables 5.8 and 5.9 display minimal differences within the uncertainty range. This suggests that the data derived from the cross-sections are more reliable, both for the main and secondary maxima. Particularly for the secondary maxima, the parameters' uncertainty from the maps is even higher due to significant overlap in the asymmetrical maps.

5.5 Ridges

In this section, we will focus on evaluating the results for the samples with ridge-shaped microcrystals. We divide them into two groups, depending on the orientation of the ridges - parallel to the edge of the substrate [110] or at angle of 45° with normal to sample edge. We will compare the reciprocal space maps and the structural parameters for samples in these two groups.

5.5.1 Parallel to [110]

There are two options for the width of the ridges, 2 or 5 μm, and the three for the trench between them, 1, 2 or 3 μm. Photos of the sample´s surface structure are shown in figure 5.18.

In the case of the ridges, the reciprocal space maps must be measured for two azimuths, one in the parallel to ridges, see figure 5.19, and the other one

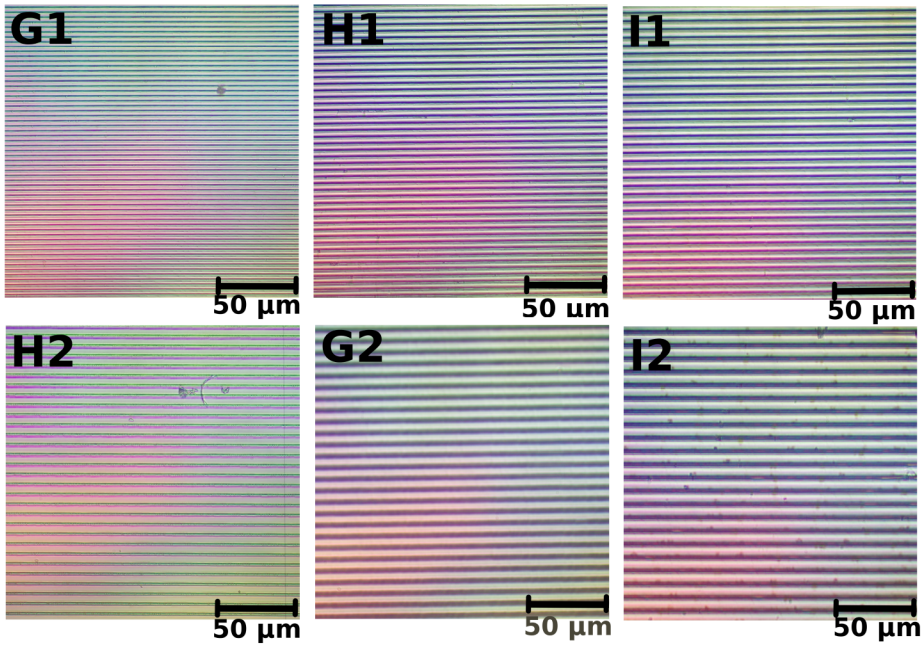

Figure 5.18 Images captured with the Zeiss 2E optical microscope depict the surface of the samples with ridges parallel to the sample edge. These samples vary in the ridge width and the trench sizes.

perpendicular to them, see figure 5.20. The difference in the intensity is clearly visible, when comparing the figures for different azimuths. While for the azimuth perpendicular to the ridges the maxima are always extended with strong diffuse scattering, for the other direction the maxima are usually small and narrow. This is caused by the geometry of the ridges. In the scattering plane perpendicular to the ridges, there is an opportunity for the ridges to relax sideways, however this is not possible in the parallel direction.

We will focus on the maps in figure 5.19. For samples with the 2 µm wide ridges (G1, H1, I1), the diffraction maximum is very broad and has a clear elongation in the Q_x direction. For samples with the 3 µm ridges (G2, H2, I2) it is less elongated. The secondary maxima are visible only for the samples with the large trench, i.e. I1 and I2, which have the 3 µm trenches. The same situation for the secondary diffraction maxima from the material in trenches can be seen in the figure 5.20 for another azimuth.

For a better description of the maxima of the symmetrical diffraction (004), it is convenient to look at the cross-sections along Q_z summed over Q_x (-0.1, 0.1), see figures 5.21 and 5.22. Here as well, the secondary maxima are distinctly visible exclusively in the I samples. Furthermore, we can see that the diffraction peaks for the samples G1 and G2 behave as an over-relaxed and strained layer similarlz as for samples with pillars in section 5.4. Similarly with sample A4, it is possible that the pillars have merged, due to their sizes or size of the trenches.

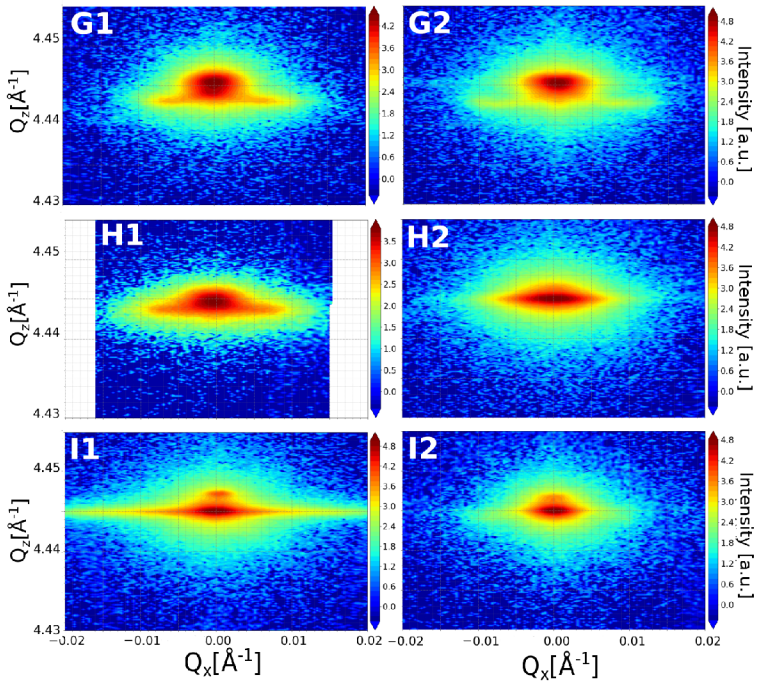

Figure 5.19 Reciprocal space maps around the symmetrical diffraction maxima (004) for samples with the ridges parallel to the edge [110] measured for the azimuth perpendicular to the ridges.

A more intense peak in the cross-section for samples G1 and G2 in figure 5.22 would correspond to diffraction in the merged microcrystals since they are more strained in this case [11].

Table 5.10 Parameters for the main maxima obtained from the Q_z cross-sections of (004) diffraction for the ridges samples G1 - I2 in the direction perpendicular to the ridges.

Sample	R	$\epsilon_{\parallel}[\%]$	$\epsilon_{\perp}[\%]$
G1	1.031 ± 0.003	0.112 ± 0.008	-0.094 ± 0.009
G2	1.031 ± 0.004	0.103 ± 0.009	-0.092 ± 0.007
H1	1.023 ± 0.005	0.08 ± 0.02	-0.06 ± 0.03
H2	1.021 ± 0.002	0.084 ± 0.004	-0.065 ± 0.004
I1	1.020 ± 0.001	0.078 ± 0.003	-0.060 ± 0.001
I2	1.021 ± 0.001	0.084 ± 0.005	-0.061 ± 0.003

Finally, the relaxation values R and the components of the strain tensor will be compared. Table 5.10 presents the values for the azimuth perpendicular to the direction of the ridges and the table 5.11 for the azimuth parallel to the ridges. The relaxation for the perpendicular direction is higher, and so is the strain. As explained before, this is due to the geometry of the ridges, which allows the Ge layer to relax more in one direction while not in the other direction.

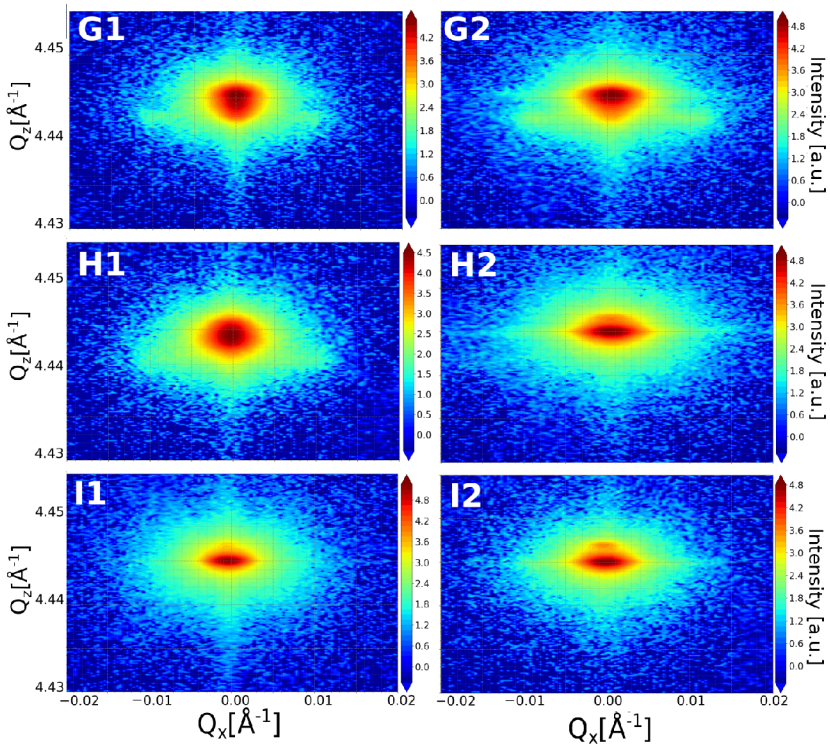

Figure 5.20 Reciprocal space maps around the symmetrical diffraction maxima (004) for samples with the parallel ridges. Measured for the azimuth parallel to the ridges direction.

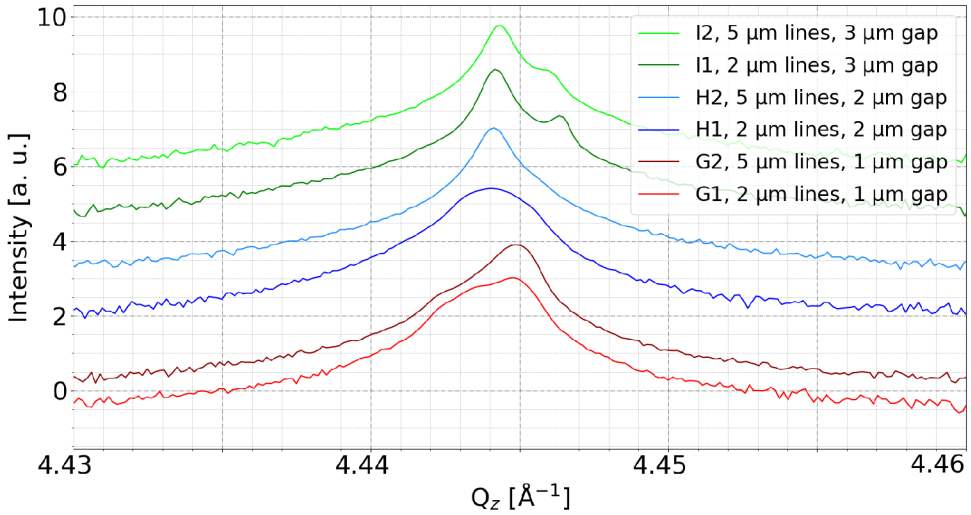

Figure 5.21 Cross-section of the reciprocal space maps from the figure 5.19 along Q_z summed over Q_x taken from -0.1 to 0.1 Å^{-1}. For the azimuth perpendicular to the ridges direction.

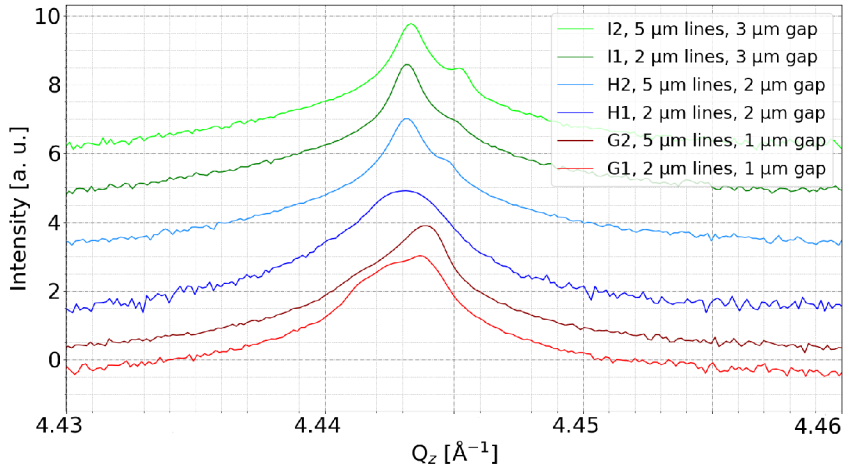

Figure 5.22 Cross-sections of the reciprocal space maps from figure 5.20 along Q_z for sum over Q_x from -0.1 to 0.1, for direction parallel with the ridges.

Table 5.11 Parameters obtained from the Q_z cross-sections of the symmetrical (004) diffraction for the main maxima for the ridges samples G1 - I2 in the direction parallel to the ridges.

Sample	R	$\epsilon_{\parallel}[\%]$	$\epsilon_{\perp}[\%]$
G1	1.014 ± 0.005	0.114 ± 0.002	− 0.094 ± 0.002
G2	1.015 ± 0.004	0.115 ± 0.003	− 0.091 ± 0.004
H1	1.008 ± 0.006	0.07 ± 0.01	− 0.05 ± 0.02
H2	1.009 ± 0.005	0.071 ± 0.001	− 0.051 ± 0.001
I1	1.008 ± 0.003	0.070 ± 0.002	− 0.052 ± 0.002
I2	1.007 ± 0.001	0.068 ± 0.002	− 0.048 ± 0.001

5.5.2 Parallel to [100]

The spectrum of the samples offers the same possible combinations of the width of the ridges and the trenches as for the samples with ridges parallel to edge of substrate. But in this case, the substrate was patterned with the ridges at an angle of 45° with respect to the edge of substrate. How the sample surfaces look like is shown in figure 5.23 using the Zeiss 2E optical microscope.

Similarly as for the parallel ridges, it is important to show both azimuths for the symmetrical diffraction maximum (004), to emphasize the different behavior of the diffraction signal depending on the scattering plane direction with respect to the ridges. In figure 5.24 the diffraction maps for the azimuth parallel to ridges are presented. In the Q_x direction we see a very small elongation, but in the Q_z direction we see peak split. This split appears as the secondary maxima in the cross-sections graph, see figure 5.25. Therefore, the maxima appear much broader in the Q_z direction. The secondary maxima are not present in the samples L1 and L2, due to the small gaps between the ridges.

Looking at the diffraction maxima of the symmetrical diffraction (004) with

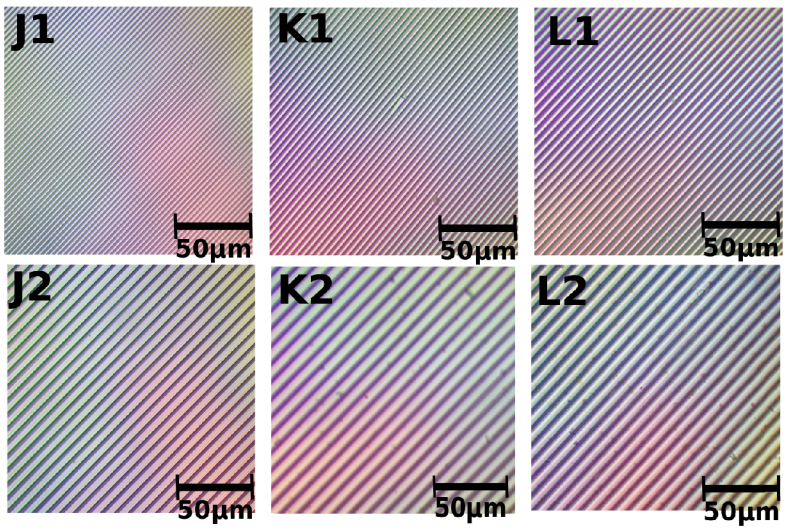

Figure 5.23 Images captured with the Zeiss 2E optical microscope depict samples with ridges having an angle of 45° with the substrate edge. These samples vary in the ridge width and the trench size.

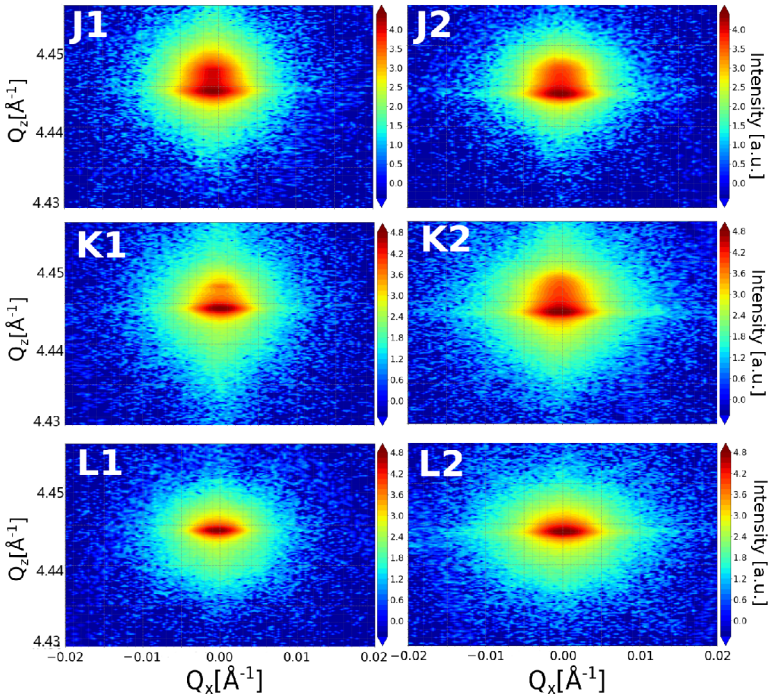

Figure 5.24 Reciprocal space maps around the symmetrical diffraction maxima (004) for samples with ridges parallel to [100]. Measured for the azimuth parallel to the ridges direction.

the scattering plane perpendicular to the orientation of the ridges, see figure 5.26, it is clear that this direction has much wider peaks in Q_x. This is caused

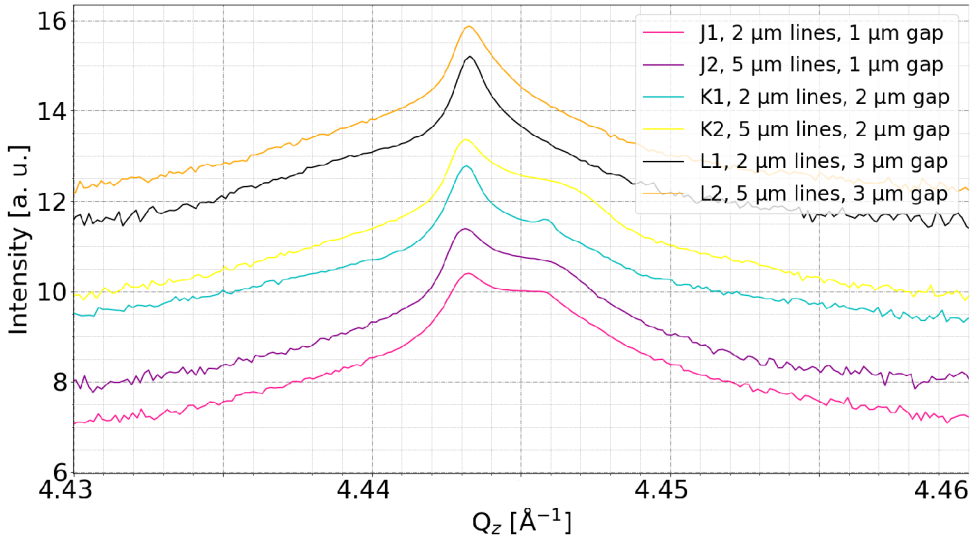

Figure 5.25 Cross-sections through the Ge (004) along Q_z for the ridge base samples grown at the 45° angle.The azimuth parallel to the ridges.

by the geometry of ridges. This is demonstrate also by the higher relaxation and strain values in table 5.12 and in table 5.14 for the parallel and perpendicular directions respectively. Once again, it is possible to conclude that the material has a greater possibility to relax in the direction perpendicular to the ridges than in the direction parallel to them.

Table 5.12 Parameters obtained from the Q_z cross-section for the main maxima for the ridge samples J1 - L2 in the direction parallel to the ridges.

Sample	R	$\epsilon_{\parallel}[\%]$	$\epsilon_{\perp}[\%]$
J1	1.0140 ± 0.0007	0.060 ± 0.003	− 0.048 ± 0.001
J2	1.0143 ± 0.0003	0.060 ± 0.003	− 0.048 ± 0.002
K1	1.0141 ± 0.0004	0.060 ± 0.002	− 0.050 ± 0.002
K2	1.0139 ± 0.0009	0.058 ± 0.004	− 0.045 ± 0.003
L1	1.0143 ± 0.0007	0.060 ± 0.001	− 0.049 ± 0.001
L2	1.0144 ± 0.0005	0.060 ± 0.001	− 0.046 ± 0.01

Table 5.13 Parameters obtained from the Q_z cross-section for secondary maxima for the ridge samples J1 - L2 in the direction parallel to the ridges.

Sample	R	$\epsilon_{\parallel}[\%]$	$\epsilon_{\perp}[\%]$
J1	1.037 ± 0.008	0.06 ± 0.01	− 0.05 ± 0.02
J2	1.037 ± 0.007	0.06 ± 0.02	− 0.05 ± 0.02
K1	1.036 ± 0.003	0.06 ± 0.02	− 0.05 ± 0.01
K2	1.040 ± 0.006	0.06 ± 0.01	− 0.05 ± 0.01

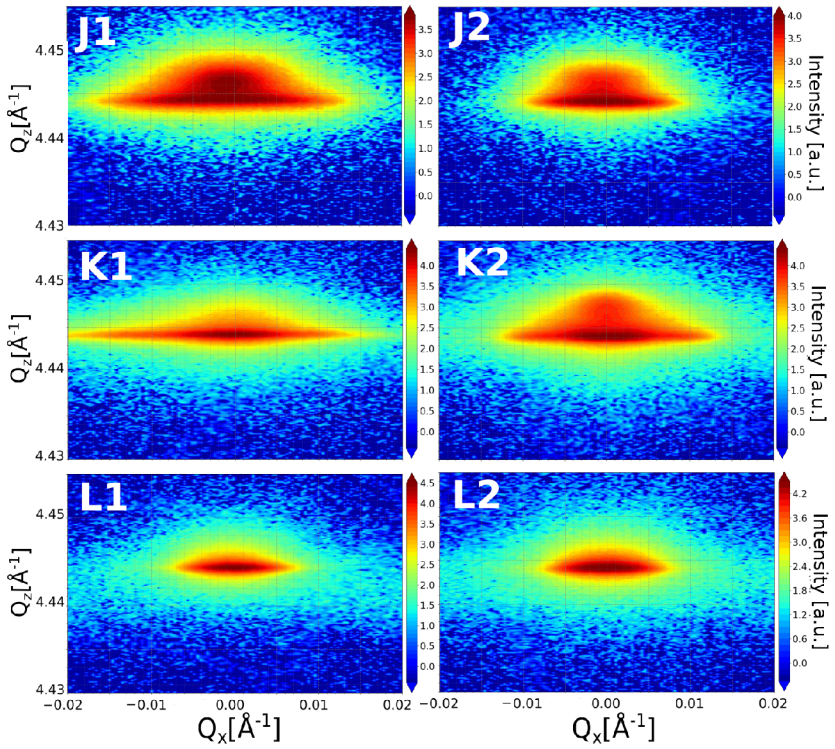

Figure 5.26 Reciprocal space maps around the symmetrical diffraction maxima (004) for samples with the ridges parallel to the [100]. Measured for the azimuth perpendicular to the ridges.

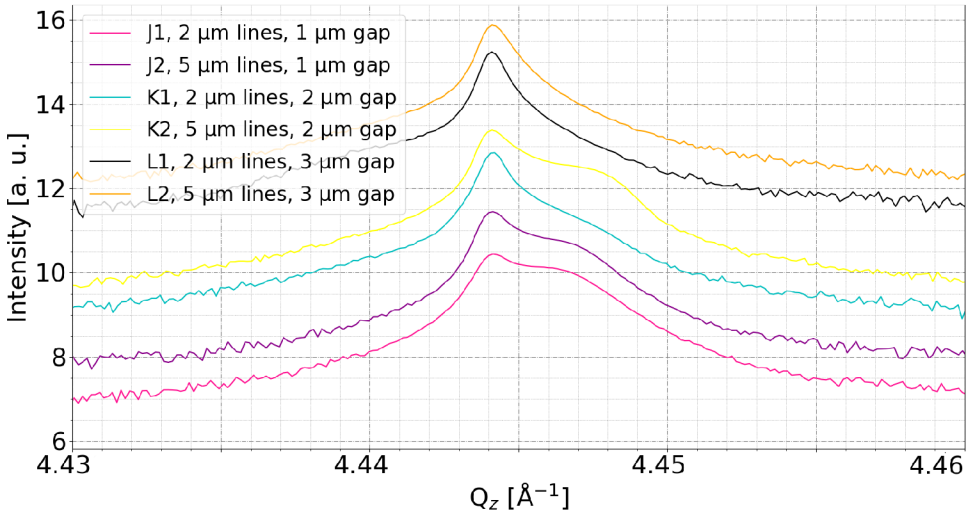

Figure 5.27 Cross-sections through the Ge (004) along Q_z summed over Q_x from -0.1 to 0.1 for the ridge samples grown at the 45° angle. The azimuth perpendicular to the ridges.

For the secondary maxima, see tables 5.13 and 5.15, the relaxation reaches large values compared to the material deposited on the pillars. At the same time, these values have unfortunately higher statistical errors, which is caused by the width of the peaks. In this case, the secondary maxima for the samples L1 and L2 are missing.

We obtained the parameters in tables 5.12, 5.13, 5.14 and 5.15 using calculation from Q_z cross-sections assuming the pure Ge contents. Relaxation values R were obtained using the relation (5.1) and the strain components $\epsilon_{\parallel}$ and $\epsilon_{\perp}$ using the equations (5.2) and (5.3). They will be compared with those obtained from the (404) asymmetrical reciprocal maps, see the appendix A.2. The parameters derived from the maps are quite random with a large measurement uncertainty. Nevertheless, apparent trends emerge from both datasets. The reciprocal space maps reveal much higher relaxation and strain values for the azimuth perpendicular to the ridges, that is in the contrast with the less relaxed and strained state in the direction parallel to ridges. Furthermore, the agreement is also evident in the secondary maxima for relaxations and both strain components.

Table 5.14 Parameters obtained from the Q_z cross-section for the main maxima for the ridge samples J1 - L2 in the direction perpendicular to the ridges.

Sample	R	$\epsilon_{\parallel}$[%]	$\epsilon_{\perp}$[%]
J1	1.0279 ± 0.001	0.11 ± 0.02	− 0.09 ± 0.01
J2	1.0277 ± 0.002	0.11± 0.04	− 0.10 ± 0.05
K1	1.0283 ± 0.001	0.12 ± 0.07	− 0.08 ± 0.06
K2	1.0260 ± 0.001	0.11 ± 0.04	− 0.09 ± 0.01
L1	1.0275 ± 0.001	0.11 ± 0.07	− 0.09 ± 0.06
L2	1.0270 ± 0.001	0.10 ± 0.06	− 0.10 ± 0.06

Table 5.15 Parameters obtained from the Q_z cross-section for the secondary maxima for the ridge samples J1 - L2 in the direction perpendicular to the ridges.

Sample	R	$\epsilon_{\parallel}$[%]	$\epsilon_{\perp}$[%]
J1	1.049 ± 0.008	0.22 ± 0.02	− 0.17 ± 0.02
J2	1.050 ± 0.007	0.20 ± 0.03	− 0.17 ± 0.02
K1	1.052 ± 0.004	0.20 ± 0.02	− 0.16 ± 0.03
K2	1.054 ± 0.007	0.19 ± 0.03	− 0.16 ± 0.02

5.6 The peak elongation in Q_x direction

This section focuses on the shape of the peaks in the reciprocal space maps along the Q_x direction, where some samples exhibits elongation of the intensity around main peak.

For the pillar samples the elongation is clearly observed for the samples C2, B3, A4 and B4, see figures 5.7, 5.13 and 5.16. In the cross-sections for these

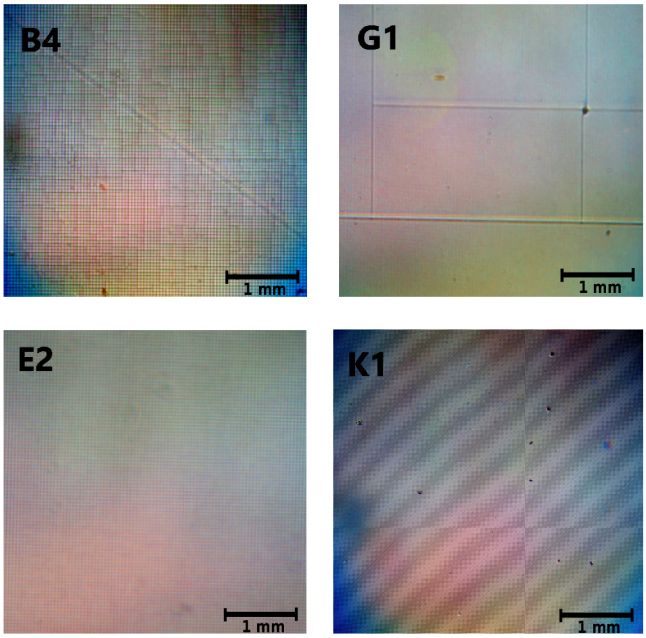

Figure 5.28 Images captured with the Zeiss 2E optical microscope. Cracks are visible on the samples B4 and G1.

samples see figures 5.8, 5.14 and 5.17, we see that the shapes of the peaks are unusual. Similarly, the ridge samples G1, G2, and H1, aligned parallel to the substrate edge [110], also demonstrate these atypical peak shapes, see figure 5.19. For samples with the ridges at the angle of 45° with the edge of the substrate, it is possible to claim that we see a similar phenomenon for the samples J1, J2 and K2, see figure 5.26. For samples with ridges the peak elongation is observable only in the scattering plane perpendicular to ridges.

As mentioned before, these satellite maxima can originate from the edges of the cracks. A certain number of pillars can merge and form the continuous layer, which can grow defect-free only up to a certain critical thickness. During the cooling process from the growth temperature to the room temperature, thermal stress increases, causing the continuous layer to develop cracks. These cracks form across the entire array of microcrystals, resulting in square-shaped domains [11].

The crystal structure has sufficient space to relax by bending at the borders of the crack domains, but not in the middle of them. Consequently, we expect a more pronounced bending of the crystal lattice at the domain boundaries. This correlation suggests that the peak width will likely be greatly influenced by the cracks formed between these merged SiGe microcrystal domains [11].

To test these hypotheses, we examined the samples again with the Zeiss 2E optical microscope, as shown in figure 5.28. For the samples in photos B4 and G1, we can clearly see cracks that form individual domains, while samples the E2 and K1 do not have these cracks. Therefore, the samples displaying

satellite maxima on the reciprocal maps exhibit cracks under the microscope and this correlates for all samples. While the samples that do not have significant elongation in the Q_x direction show no signs of cracks.

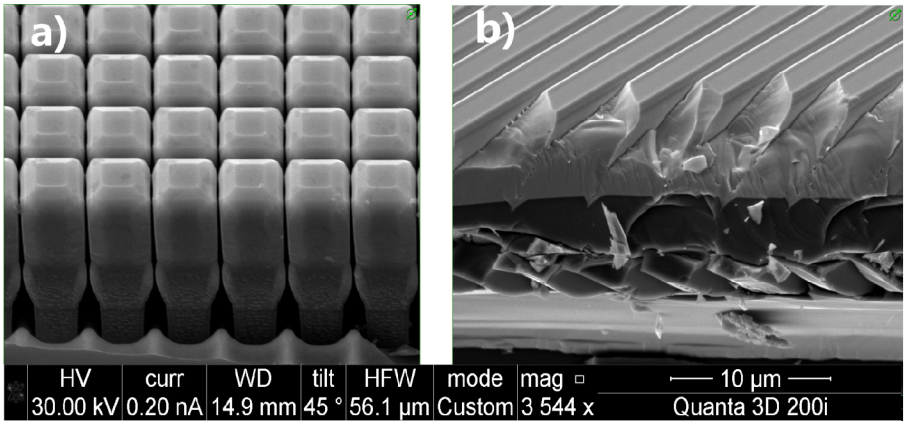

Figure 5.29 Perspective view SEM micrographs of the Si/Ge microcrystals. (a) Pillar sample D2 with the base size 5x5 µm and the trench size 4 µm. (b) Ridge sample J2 with the ridge width 2 µm and the trench size 1 µm oriented 45° from the sample edge.

To confirm merging of the pillars, we examined some samples using the scanning elektron microscope (SEM) Fei Quanta 200i, see figure 5.29. In figure 5.29(a) perspective view SEM micrographs for sample D2 is shown. Even though the pillars have grown to the lateral dimension, there is still some gap between the individual pillars. In figure 5.29(b) the perspective view SEM micrographs for J2 is shown. We can see that the ridges on this sample have grown together as well, creating the continuous layer that has formed cracks.

5.7 Coverage

In this section, the sample coverage will be examined. The coverage can be calculated as:

$$c = \frac{a^2}{(a+t)^2} \tag{5.4}$$

where a is edge size of the pillars and t corresponds to the trench size. All these values can be obtained from figure 5.2 for square-based samples and from 5.3 for ridge-based one for the nominal values of Si substrate. It should be noted that the coverage of the Si pillars is different from the resulting Ge coverage. In figure 2.2(b), we can see that the overlap of the Ge layer over the Si substrate occurs. Therefore, we tried to determine the size of the edge of the Ge pillars and the gap between them from the photos of the samples that were taken using the microscope. The trench size was determined as the difference between the period and edge size, with the period taken as the difference between the centres of two neighbouring Ge microcrystals. The results for all samples are in table 5.16. We can see that the trend of decreasing coverage for the increasing

trench is preserved, and at the same time coverage increases for the increasing base size of the pillars. This is true for both Si and Ge. In graphs of cross-sections, the ratio of intensity of the peaks corresponding to the relaxed Ge to the strained Ge changes with changing coverage of the sample surface by microcrystal pillars can be seen. Furthermore, intensity of diffracted radiation on the Ge microcrystals in the maxima depends directly proportionally on the area covered by the microcrystals.

Table 5.16 Geometric parameters for pillars. Si values calculated from in the figures 5.2 and 5.3 and Ge determined from the photos taken by optical microscope.

	Edge[μm]		Trench[μm]		Coverage	
Sample	Si	Ge	Si	Ge	Si	Ge
A2	5	5.8	1	0.4	0.69	0.87
B2	5	6.0	2	1.0	0.51	0.73
C2	5	6.2	3	1.9	0.39	0.59
D2	5	5.9	4	3.0	0.31	0.44
E2	5	6.1	5	4.2	0.25	0.35
F2	5	6.0	50	49.5	0.008	0.01
A3	9	10	1	0.2	0.81	0.96
B3	9	9.9	2	1.0	0.67	0.82
C3	9	10.2	3	1.6	0.56	0.75
D3	9	10.1	4	2.6	0.48	0.63
E3	9	10	5	3.2	0.41	0.57
F3	9	9.9	50	48.7	0.02	0.03
A4	15	16.3	1	0.2	0.88	0.98
B4	15	16.0	2	0.8	0.78	0.91
C4	15	16.2	3	1.3	0.69	0.86
D4	15	16.5	4	2.9	0.62	0.72
E4	15	16.6	5	4.0	0.56	0.65
F4	15	16.0	50	49.0	0.05	0.06
G1	2	2.6	1	0.3	0.44	0.80
H1	2	2.8	2	.0.7	0.25	0.64
I1	2	2.8	3	1.5	0.16	0.42
J1	2	3	1	0.3	0.44	0.83
K1	2	2.7	2	0.6	0.25	0.67
L1	2	2.9	3	1.4	0.16	0.45
G2	5	6.1	1	0.1	0.69	0.96
H2	5	6.0	2	0.5	0.51	0.85
I2	5	5.9	3	1.2	0.39	0.69
J2	5	6.0	1	0.2	0.69	0.93
K2	5	6.2	2	0.6	0.51	0.83
L2	5	6.3	3	1.4	0.39	0.66
		± 0.1		± 0.1		± 0.05

5.8 Full width at half maximum of diffraction peaks

Cross-sections along the Q_x axis were obtained from the maps of the symmetrical diffraction maxima (004), see figure 5.30. The cross-section is made through the fixed Q_z value for which we get the maximum intensity. Full width at half maximum (FWHM) values were subsequently obtained from this. The FWHM values are presented for all samples in table 5.17. For the ridges we calculated

Table 5.17 Values of FWHM obtained from diffraction maxima cross-section along Q_x for fixed Q_z values.

Sample	FWHM[Å^{-1}]	
A2	0.0028	
B2	0.0028	
C2	0.0030	
D2	0.0032	
E2	0.0033	
F2	0.006	
A3	0.0026	
B3	0.0026	
C3	0.0027	
D3	0.0028	
E3	0.00280	
F3	0.0040	
A4	0.0029	
B4	0.0037	
C4	0.0044	
D4	0.0046	
E4	0.0048	
F4	0.0052	
	± 0.0001	
Sample	FWHM perpendicular	FWHM parallel
G1	0.0028	0.0023
H1	0.0038	0.0025
I1	0.0034	0.0024
J1	0.0085	0.0042
K1	0.0087	0.0043
L1	0.0054	0.0043
G2	0.0029	0.0028
H2	0.0046	0.0029
I2	0.0029	0.0027
J2	0.0083	0.0033
K2	0.0088	0.0033
L2	0.0068	0.0032
	± 0.0001	± 0.0001

the FWHM for both azimuths - perpendicular and parallel to the ridges. The FWHM was obtained simply as the width of the measured peak at half its global maximum, see figure 5.30(b). FWHM contains information about the crystal quality of the examined samples.

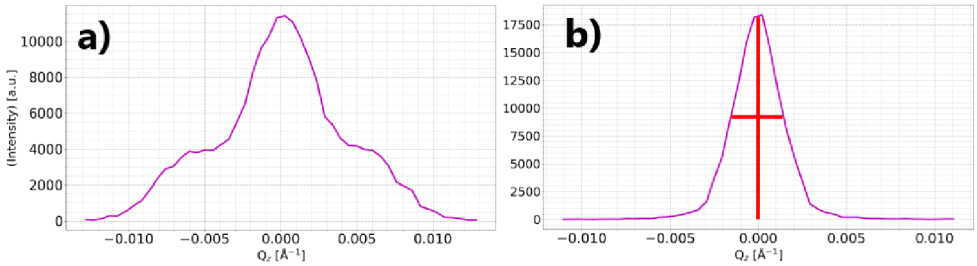

Figure 5.30 Examples of cross-sections along Q_x through the fixed Q_z value. (a) The cross-section for sample B4, which has clearly observable sattelite maxima. (b) The cross-section for sample B2, which has a narrow and sharp maximum. A method for determining the FWHM is indicated.

In figure 5.30 the difference in the cross-sections for the two samples are shown. While the sample B4 has a broadened peak in the Q_x direction, see figure 5.16, the sample B2 does not show such a broadening, see figure 5.7. We can clearly see this in the cross-sections as well. The cross-section for B4 consists of multiple peaks and the main peak is broader, see figure 5.30(a), while for B2 the peak is sharp and probably cannot be decomposed, see figure 5.30(b).

For greater clarity of the mechanisms causing the different shapes of diffraction peaks, it is good to perform a Gaussian decompositions through cross-sections along Q_x. Peaks can be fitted with the sum of two or even three Gaussians [19]. From the FWHM values, it can be concluded that the different elongations are present in the Q_x direction. Several factors can contribute to this elongation. Firstly, the presence of crystal defects, mainly the misfit and threading dislocations. Secondly, the individual crystal tilting which arises from the random misfit dislocation network at the Si/Ge interface. Individual crystal tilting arises from the random MD network at the Ge/Si interface. And third possibility is the lattice bending due to thermal strain [20].

With laboratory conditions, it is possible to measure only the signal coming from the diffraction from a large number of randomly oriented microcrystals. We do not see separate maxima in the measured diffractions, where each would belong to individual microcrystal, we observe only different shapes of these maxima. The number of Gaussians required to fit the given profile depends on the strain of the crystal lattice. If the diffraction maximum comes from an unstrained lattice with randomly oriented microcrystals, the shape of the peak may corresponds to a Gaussian. This means that the distribution of random tilts can be well described by a Gaussian distribution. However, if the lattice is significantly bent and contains misfit dislocations, the maximum is better described by the sum of Gaussians [17].

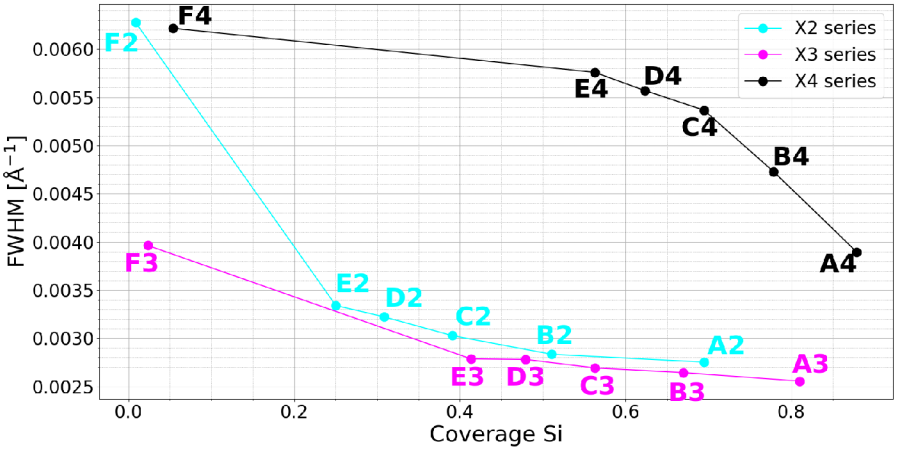

Figure 5.31 Dependence of FWHM on Si pillar coverage for square base samples. Each color belongs to pillars with different edge sizes.

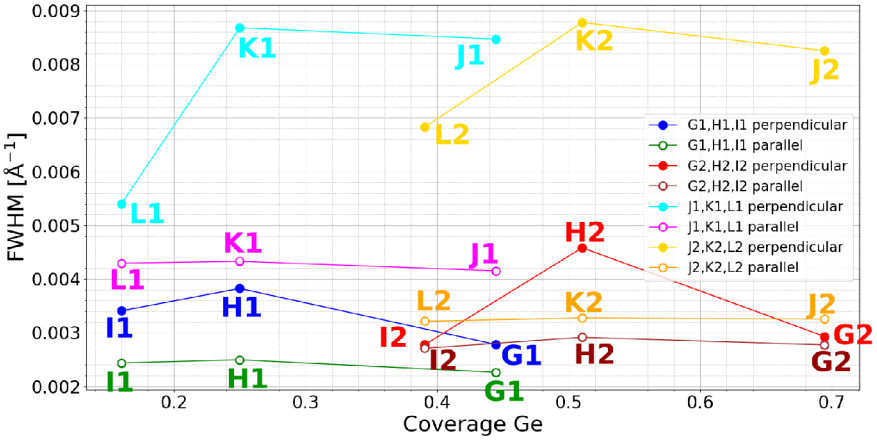

Figure 5.32 Dependence of FWHM on Si pillar coverage for ridge-base samples. Each color belongs to samples with different ridge width or to a different diffraction direction with respect to the ridges.

In figures 5.31 and 5.32, we show the measured FWHM of the diffraction peaks for relaxed Ge depending on the Si coverage. Since we are dealing with the description of the Si/Ge interface, we use Si and not Ge coverage values. In addition, the Si coverage is given by the nominal values of the dimensions of the pillars, while the Ge parameters were determined from photos, which could introduce an uncertainty into the results.

First, we discuss this dependence for pillar samples. In the figure 5.31, we can see that the dependence has a similar shape for all three series. For all series we see a clear tendency for the FWHM to decrease with increasing coverage. It

is possible to draw the conclusion that at a constant size of microcrystals, the diminishing trench size appears to narrow the diffraction peaks.

For ridges samples are the resulting dependences are shown in figure 5.32. Here as well, a certain similarities can be seen for individual curves. For the measurements in direction perpendicular to the ridges, a significant maximum for can be seen. On the other hand, for the parallel direction, this maximum is smaller and less significant. This maximum is for samples K1, K2 and H1 and H2, which all have the same trench size. Additionally, it is noticeable that the the changes in FWHM are minimal in the parallel direction. However, in the perpendicular direction, there is a more distinct variance observed among the samples. Moreover the values of FWHM are larger for scattering plane perpendicular to the ridges than in the direction parallel with them.

5.9 Properties depending on location of the sample

Finally, we also decided to explore if the structural parameters of the individual samples obtained in this diploma thesis could show any dependence on the position on the Si wafer during the deposition.

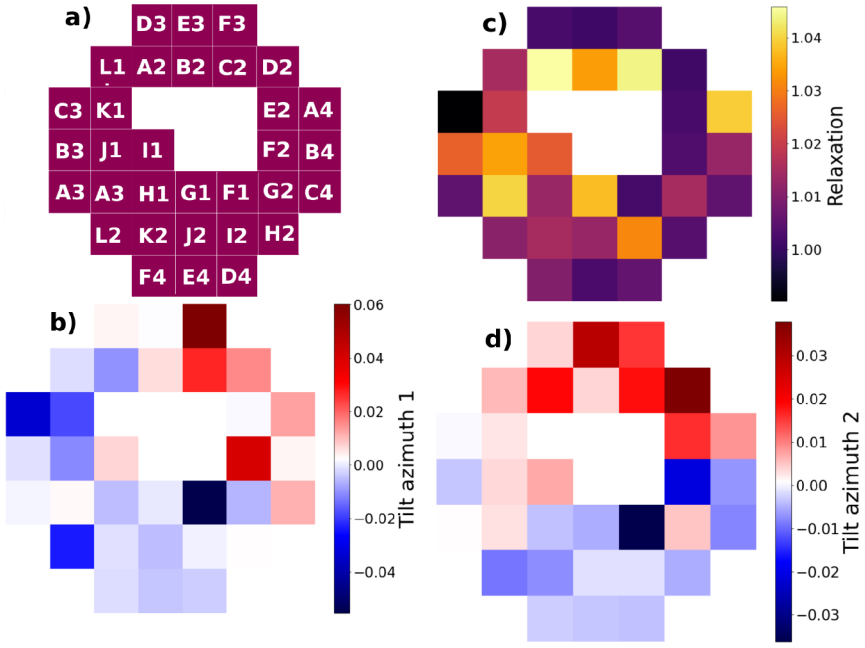

Figure 5.33 (a) Position of the samples on the Si wafer. White spaces in the middle represent samples that were not available for measurement. (b) Tilt value measured in direction of azimuth 1. (c) Relaxation values obtained the from symmetrical and the asymmetrical diffraction maps. (d) Tilt values obtained in direction of azimuth 2.

Figure 5.33(a) shows the positions of the individual samples on the Si wafer during the deposition. Unfortunately, the samples in the center of the wafer were not available for the measurement. Subsequently, the panels (b), (c), (d) show

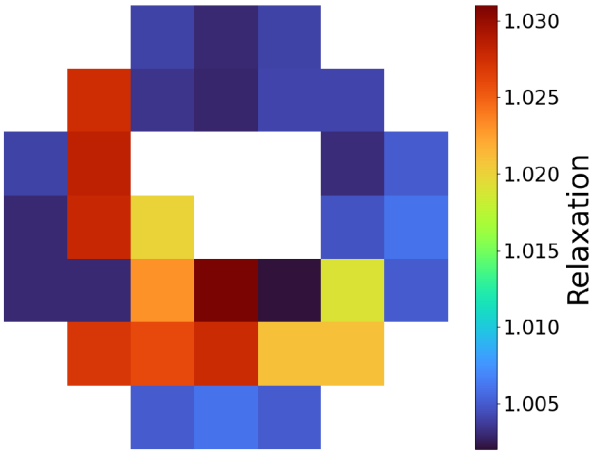

Figure 5.34 Relaxation values obtained from the cross-sections along Q_z.

the parameters that were obtained by calculation using both the symmetrical (004) and the asymmetrical (224)/(404) reciprocal space maps. Part (c) shows the relaxation parameter R. It is not possible to observe any spatial dependence here. There are similar color variations for both strain components. This is perhaps due to the fact that, as we mentioned for the individual samples, the results obtained from the measurement of the asymmetrical maps have a large measurement uncertainty. However, looking at images (b) and (d), which show the tilt in two different directions, we observe more systematic color distribution across the wafer. While in the upper right part the values are more in red and therefore positive numbers, in the lower left part the blue color dominates, which means the negative values. This can be influenced bz the target during the deposition of microcrystals.

Figure 5.34 shows the relaxation values obtained from the Q_z cross-sections of the symmetrical diffraction summed over Q_x from -0.1 to 0.1. However, we do not observe any dependence on position of the samples. Only changes depending on the shape of the Si pillars can be seen. While the relaxation is much closer to 1 for the pillar based samples, the relaxation is much higher for the ridged samples. It is even possible to claim that for samples with ridges at an angle of 45° from the sample edge the relaxation is usually slightly higher than for parallel ones.

Chapter 6

Summary

In this work, we studied samples of the epitaxial Ge microcrystals grown on the pre-patterned Si substrate. We measured two different groups of the samples depending on the shape of the patterning of the substrate - pillars or ridges. The symmetrical and the asymmetrical reciprocal space maps were measured for all samples in an ultra-high resolution set-up.

Firstly, the results for the pillar-based samples will be discussed. We divided these samples into three groups with the same base size. So they differed only in the size of the trenches in one group. Results for the X2 series with a 5x5 μm base size are described in section 5.4.1. Our goal was to determine the structural parameters of Ge microcrystals. We wanted to use the positions of the diffraction maxima in the symmetrical (004) and the asymmetrical (224) maps, see figures 5.7 and 5.9. The detailed results of determined structural parameters are shown in the appendix A.1. However, we observed that these values have a large statistical uncertainty, which probably comes from the asymmetrical maps. That is why we finally decided to choose a different approach, which was based on the assumption that microcrystals are made of pure Ge. We used the cross-sections along Q_z summed over Q_x, where we converted Q_z values into the relaxation values R and intp the parallel $\epsilon_{\|}$ and perpendicular $\epsilon_{\perp}$ components of the strain tensor, see figures 5.10, 5.11 and table 5.4. These values have a smaller uncertainty than the structural parameters obtained from RSMs.

In the RSMs for samples C2, D2 and E2 the secondary maxima placed above the main diffraction maxima occurs, see figure 5.7. The origin of the secondary maximum is from Ge, which was deposited between the Si pillars directly on substrate in trenches [2]. Structural parameters were also determined for the secondary maxima, see table 5.5. While the Ge microcrystals deposited on the Si pillars are mostly relaxed and not strained, the Ge material in the trenches is overrelaxed and strained. The secondary maximum also occurs in the RSM for sample F2. Here, however, the situation is a little different. Sample F2 has very few pillars with large trench size 50 μm width, and therefore more material is deposited between the pillars than on them. Thus, the more intense maximum with a higher Q_z value corresponds to relaxed Ge deposited between the pillars, while the lower maximum corresponds to Ge microcrystal.

For samples A2 and C2, the satellite maxima appeared in the RSMs, which

cause an extension of the peak in the Q_x direction. The satellite maxima have a smaller Q_z value than the main diffraction peak and exhibit a larger tilt as well. The reason for the appearance of these maxima are cracks. They arise if the trenches between the pillars are too small and a certain number of microcrystals merged together. The continuous layer formed in this way cannot grow beyond certain critical thickness without defects, and forms crack after cooling to the room temperature [11].

We performed a similar analysis for the samples from the X3 series, which have the base size 9x9 µm, differing in the trench sizes as well. The structural parameters calculated from the symmetrical and the asymmetrical maps are shown again in table A.1 in the appendix A. Due to the large uncertainties from the asymmetrical maps, we chose the approach that includes the assumption of pure Ge, see table 5.6. In this series, the secondary maxima are observed for samples C3, D3, E3 and F3, for the parameters see table 5.7. While the primary maxima originate from the Ge microcrystals and thus are relaxed and strain-free, the secondary maxima originate from the Ge material in the trenches and they are over-relaxed and strained. Also for the F3 sample, the similar assumption applies as for F2. The more intense peak with the higher Q_z coordinate belongs to the material between the pillars, while the lower peak is from the microcrystals. For samples B3 and C3, the satellite maxima are present again, which come from the cracks, observed also by optical microscope.

As the last pillar-based samples, we investigated the group of samples with an base size 15 µm which differ in the trench sizes in this group. For RSMs around the symmetrical (004) diffraction let us see figure 5.16. In these RSMs, the secondary maxima are observable for all the samples except A4, and the satellite maxima are observed for samples A4 and B4. Therefore we can expect the presence of cracks in the two samples A4 and B4, whick was confirmed by optical microscope again. The structural parameters were determined from the Q_z cross-sections for the main and the secondary maxima, see tables 5.8 and 5.9.

The second group of samples we investigated are the microridges. We divided them into two groups according to the orientation of the ridges with respect to the edge of the substrate. The first set is composed from the ridges parallel to the substrate edge. They differ in the width of the ridges and the trench sizes. While for the pillar-based samples it is usually sufficient to measure RSM for only one azimuth due to spatial symmetry, for ridge samples it is necessary to measure the RSMs in two azimuths. The distinctions between these two orientations—parallel and perpendicular—are clearly observable in figures 5.19 and 5.21. When measuring in the azimuth perpendicular to the ridges, the maxima consistently exhibit elongation, whereas in the other direction, they tend to be smaller and narrower. The scattering plane perpendicular to the ridges offers an opportunity to see the lateral relaxation of the ridges. This possibility is not available in the direction parallel to the ridges. The resulting structural parameters also correspond to this. While in the perpendicular direction the layer is over-relaxed and strained, in the parallel direction the layer is practicaly relaxed and strain-free, see tables 5.10 and 5.11. The secondary maxima are

observable only for the samples with large trenches I1 and I2 demonstrating the large amount of material in the trenches. Within this group, we can assume merging of the microridges for the samples G1, G2 and perhaps for H1, due to present of the lateral satellites connected with the cracks.

The second set of the samples is composed from the microridges parallel to the [100] direction, and thus at angle 45° with respect to the substrate edge. It was also necessary to measure the RSMs in two different directions - the scattering plane perpendicular and parallel to the ridges, see figure 5.24 and 5.26. The calculation of the structural parameters confirmed that the direction parallel to the ridges is closer to the relaxed state than the crystal lattice along the direction perpendicular to the ridges. For these samples, the possible cracks in the Ge layer do not appear as the separated lateral maxima but only as the continuous diffuse scattering present within the peak elongation. According to shape of the Q_z cross-sections for perpendicular direction, see figure 5.27, we can assume that cracks will appear for the samples J1, J2 and K2.

As for the pillars, as for the ridges, we observed the extension of the diffraction peak along the Q_x direction, which is probably caused by the cracks of the Ge layer composed from merged microcrystals. This was found in several samples usually with the smaller trench sizes. In the section 5.6, we verified the formation of cracks for the samples first with the optical microscope, see figure 5.28, and then also with the SEM, see figure 5.29. With the optical microscope, we were able to capture the crack domains that were formed on all the samples with an elongated peaks in the Q_x direction. As examples, we have shown the optical images of the pillar sample B4 and the ridge sample G1, see figure 5.29. Moreover, we verified the merging of the microcrystals in the SEM, see figure 5.29. While the gaps between the individual microcrystals were preserved in sample D2, for sample J2 it is clearly visible that the microcrystals have merged.

Next, we focused on determining the FWHM and its dependence on the coverage, see figures 5.31 and 5.32. For the pillars divided into the three groups as mentioned above, we see decreasing dependencies. In reference [20] the similar results are shown as well. As the coverage decreases, the FWHM increases. For ridge samples, all measured series show the same dependence - the maximum for a sample with a trench size of 2 μm. Changes in the FWHM are minimal in the parallel direction. Moreover, the values of FWHM are larger for the direction perpendicular to the ridges than in the direction parallel with them due to the relaxation state.

Finally, we looked at the distribution of the samples at the deposition and tried to determine if the parameters might show any positional dependence. For the structural parameters, relaxation and strain, we were unfortunately unable to determine any clear dependence on the position, see figures 5.33 and 5.34. This is probably due to the large uncertainty for the parameters calculated using the asymmetrical RSMs. However, when we look at the tilt measured in two azimuths, see figure 5.33(c)(d), it is possible to expect the depedence of the parameters on the target position during the layer deposition. Finally, the figure 5.34 shows the relaxation values calculated from the Q_z cross-sections. Although

no dependence on the position can be seen here, we can clearly see the difference in the relaxation values depending on the patterning of the samples. While the pillar samples have a state of relaxation more closer to 1, for the ridge samples we get an over-relaxed layer. Moreover, we can claim that for the ridges at an angle of 45° with respect to the edge of the substrate, the relaxation is even higher than for the parallel ones.

Chapter 7

Conclusion

In this diploma thesis, samples of Ge epitaxial microcrystals grown on a pre-patterned Si substrate were studied. The microcrystals differed in the sizes and shapes of the base and in the size of the trenches in between them. The analysis was performed using X-Ray diffraction technique called reciprocal space mapping. A total of 30 samples were measured, all of the same height of 16 μm composed partially from Si and Ge. Totally samples involved 18 square pillars and 12 linear ridges. For the square base pillars, we compared series with the same base size and different trenches. The samples with ridges were investigated separated into two categories according to the direction of the ridges with respect to the sample edge. The RSMs were measured for each sample around the symmetrical (004) and the asymmetrical (224) or (404) diffractions. From the Ge diffraction peaks the parameters of the microcrystals, such as vertical and horizontal lattice parameters, strain and relaxation state were determined. The parameters, obtained using both the symmetrical and the asymmetrical RSMs, were compared with those calculated from the cross-sections along Q_z axis. The symmetrical RSMs for individual samples were investigated in details. Some RSMs included the secondary and the satellite maxima in addition to the main maximum. The main maxima usually corresponds to diffraction on microcrystals deposited on top of the Si pillars or the ridges in most of the samples. The secondary maximum corresponds usually to the material that was deposited between the pillars in the trenches. While the material deposited on the pillars is relaxed, the material deposited in the trenches is overrelaxed and strained. The only exception is the samples marked with the letter F. They contain large gaps between the individual pillars, which is the reason why more material was deposited in the trenches than on the pre-patterned pillars. So the more intense maximum corresponds to the overrelaxed material, while the secondary maximum corresponds to the diffraction on the microcrystals. In this work, we have also shown that the satellite maxima, observed in some cases, are caused by the merging of the microcrystals and the by subsequent cracking of the layer. Domains are thus formed, and the satellite maxima correspond most probably to diffractions at the boundaries of these domains. Our measurements demonstrate also dependence of some structural parameters on the position on the wafer substrate.

Bibliography

[1] JW Matthews, S Mader, and TB Light. Accommodation of misfit across the interface between crystals of semiconducting elements or compounds. *Journal of Applied Physics*, 41(9):3800–3804, 1970.

[2] Claudiu V Falub, Hans von Känel, Fabio Isa, Roberto Bergamaschini, Anna Marzegalli, Daniel Chrastina, Giovanni Isella, Elisabeth Müller, Philippe Niedermann, and Leo Miglio. Scaling hetero-epitaxy from layers to three-dimensional crystals. *Science*, 335(6074):1330–1334, 2012.

[3] Ullrich Pietsch, Vaclav Holy, and Tilo Baumbach. *High-resolution X-ray scattering: from thin films to lateral nanostructures.*

[4] Otfried Madelung. *Semiconductors: data handbook.* Springer Science & Business Media, 2004.

[5] R Bergamaschini, Fabio Isa, CV Falub, P Niedermann, E Müller, Giovanni Isella, H Von Känel, and L Miglio. Self-aligned ge and sige three-dimensional epitaxy on dense si pillar arrays. *Surface science reports*, 68(3-4):390–417, 2013.

[6] Hans von Känel. Merging incompatible materials. *Europhysics News*, 43(4):18–21, 2012.

[7] JW Matthews, AE Blakeslee, and S Mader. Use of misfit strain to remove dislocations from epitaxial thin films. *Thin solid films*, 33(2):253–266, 1976.

[8] J-S Park, J Bai, M Curtin, B Adekore, M Carroll, and A Lochtefeld. Defect reduction of selective ge epitaxy in trenches on si (001) substrates using aspect ratio trapping. *Applied Physics Letters*, 90(5), 2007.

[9] Claudiu V Falub, Thomas Kreiliger, Fabio Isa, Alfonso G Taboada, Mojmír Meduňa, Fabio Pezzoli, Roberto Bergamaschini, Anna Marzegalli, Elisabeth Müller, Daniel Chrastina, et al. 3d heteroepitaxy of mismatched semiconductors on silicon. *Thin Solid Films*, 557:42–49, 2014.

[10] Fabio Isa, Marco Salvalaglio, Yadira Arroyo Rojas Dasilva, Mojmír Meduňa, Michael Barget, Arik Jung, Thomas Kreiliger, Giovanni Isella, Rolf Erni,

Fabio Pezzoli, et al. Highly mismatched, dislocation-free sige/si heterostructures. *Advanced Materials*, 28(5):884–888, 2016.

[11] Mojmír Meduňa, Ondřej Caha, Emanuil Choumas, Franco Bressan, and Hans von Känel. X-ray rocking curve imaging on large arrays of extremely tall sige microcrystals epitaxial on si. *Journal of Applied Crystallography*, 54(4):1071–1080, 2021.

[12] C Rosenblad, HR Deller, M Döbeli, E Müller, and H Von Kaenel. Low-temperature heteroepitaxy by lepecvd. *Thin Solid Films*, 318(1-2):11–14, 1998.

[13] Mojmír Meduňa, Claudiu Valentin Falub, Fabio Isa, Anna Marzegalli, Daniel Chrastina, Giovanni Isella, Leo Miglio, Alex Dommann, and H von Känel. Lattice bending in three-dimensional ge microcrystals studied by x-ray nanodiffraction and modelling. *Journal of Applied Crystallography*, 49(3):976–986, 2016.

[14] Stephen Nettel. *Wave Physics: Oscillations, Solutions, Chaos*. Springer Science & Business Media, 2003.

[15] Jens Als-Nielsen and Des McMorrow. *Elements of modern X-ray physics*. John Wiley & Sons, 2011.

[16] G Bauer, JH Li, and V Holy. High resolution x-ray reciprocal space mapping. *Acta Physica Polonica A*, 89(2):115–127, 1996.

[17] Claudiu V Falub, Mojmír Meduňa, Daniel Chrastina, Fabio Isa, Anna Marzegalli, Thomas Kreiliger, Alfonso G Taboada, Giovanni Isella, Leo Miglio, Alex Dommann, et al. Perfect crystals grown from imperfect interfaces. *Scientific reports*, 3(1):2276, 2013.

[18] Rigaku. Intelligent x-ray diffraction system. `https://www.rigaku.com`. Accessed: (15.12.2023).

[19] Mojmír Meduňa, Claudiu Valentin Falub, Fabio Isa, and Hans von Känel. Growth temperature dependent strain in relaxed ge microcrystals. *Thin Solid Films*, 664:115–123, 2018.

[20] Jakub Rozbořil, Mojmír Meduňa, Claudiu Valentin Falub, Fabio Isa, and Hans von Känel. Strain relaxation in ge microcrystals studied by high-resolution x-ray diffraction. *physica status solidi (a)*, 213(2):463–469, 2016.

Appendix A

Parameters for all samples

Table A.1 Calculated parameters from the maxima of the symmetrical (004) and the asymmetrical (224) diffractions for the pillar samples.

Sample	Parameter	Azimuth 0°	Azimuth 90°
A2	tilt[°]	-0.0187 ± 0.0001	-0.0129 ± 0.0001
	$a_\perp$[Å]	5.651 ± 0.004	5.651 ± 0.002
	$a_\parallel$[Å]	5.67 ± 0.02	5.668 ± 0.009
	$\delta_\perp$[%]	4.057 ± 0.002	4.059 ± 0.004
	$\delta_\parallel$[%]	4.40 ± 0.09	4.36 ± 0.004
	$\epsilon_\perp$[%]	-0.14 ± 0.01	-0.13 ± 0.04
	$\epsilon_\parallel$[%]	0.19 ± 0.04	0.17 ± 0.06
	R	1.05 ± 0.03	1.04 ± 0.04
B2	tilt[°]	0.0039 ± 0.0002	-0.0061 ± 0.0001
	$a_\perp$[Å]	5.652 ± 0.004	5.652 ± 0.005
	$a_\parallel$[Å]	5.665 ± 0.007	5.665 ± 0.008
	$\delta_\perp$[%]	4.064 ± 0.001	4.067 ± 0.002
	$\delta_\parallel$[%]	4.31 ± 0.06	4.31 ± 0.04
	$\epsilon_\perp$[%]	-0.10 ± 0.01	-0.12 ± 0.01
	$\epsilon_\parallel$[%]	0.14 ± 0.06	0.13 ± 0.07
	R	1.03 ± 0.02	1.03 ± 0.02
C2	tilt[°]	-0.0175 ± 0.0002	-0.0021 ± 0.0001
	$a_\perp$[Å]	5.6571 ± 0.0004	5.6574 ± 0.0001
	$a_\parallel$[Å]	5.655 ± 0.002	5.675 ± 0.008
	$\delta_\perp$[%]	4.166 ± 0.001	4.164 ± 0.002
	$\delta_\parallel$[%]	4.130 ± 0.003	4.50 ± 0.08
	$\epsilon_\perp$[%]	0.015 ± 0.004	-0.0137 ± 0.004
	$\epsilon_\parallel$[%]	-0.020 ± 0.003	0.18 ± 0.07
	R	1.04 ± 0.03	1.044 ± 0.03
D2	tilt[°]	-0.0378 ± 0.0002	-0.0155 ± 0.0001
	$a_\perp$[Å]	5.6565 ± 0.0003	5.6571 ± 0.0004
	$a_\parallel$[Å]	5.654 ± 0.002	5.6575 ± 0.0001
	$\delta_\perp$[%]	4.152 ± 0.002	4.162 ± 0.001
	$\delta_\parallel$[%]	4.104 ± 0.001	4.170 ± 0.004

Sample	Parameter	Azimuth 0°	Azimuth 90°
	$\epsilon_\perp$[%]	0.020 ± 0.004	0.000 ± 0.001
	$\epsilon_\parallel$[%]	-0.026 ± 0.003	0.000 ± 0.002
	R	0.993 ± 0.02	1.001 ± 0.007
E2	tilt[°]	-0.0160 ± 0.0003	0.0014 ± 0.0001
	$a_\perp$[Å]	5.6573 ± 0.0004	5.6573 ± 0.0001
	$a_\parallel$[Å]	5.6565 ± 0.0001	5.6581 ± 0.0002
	$\delta_\perp$[%]	4.166 ± 0.002	4.165 ± 0.001
	$\delta_\parallel$[%]	4.151 ± 0.003	4.181 ± 0.001
	$\epsilon_\perp$[%]	0.000 ± 0.001	0.000 ± 0.001
	$\epsilon_\parallel$[%]	0.000 ± 0.001	0.000 ± 0.003
	R	1.000 ± 0.004	1.002 ± 0.002
F2	tilt[°]	-0.0212 ± 0.0002	0.0400 ± 0.0003
	$a_\perp$[Å]	5.657 ± 0.001	5.657 ± 0.0001
	$a_\parallel$[Å]	5.654 ± 0.003	5.659 ± 0.001
	$\delta_\perp$[%]	4.163 ± 0.006	4.164 ± 0.004
	$\delta_\parallel$[%]	4.111 ± 0.007	4.188 ± 0.006
	$\epsilon_\perp$[%]	0.022 ± 0.007	-0.010 ± 0.008
	$\epsilon_\parallel$[%]	-0.029 ± 0.007	0.013 ± 0.002
	R	0.993 ± 0.007	1.003 ± 0.003
A3	tilt[°]	0.0010 ± 0.0001	0.0010 ± 0.0002
	$a_\perp$[Å]	5.6514±0.0001	5.6514±0.0001
	$a_\parallel$[Å]	5.653±0.001	5.661±0.004
	$\delta_\perp$[%]	4.057±0.002	4.057±0.001
	$\delta_\parallel$[%]	4.094±0.001	4.23±0.05
	$\epsilon_\perp$[%]	-0.015±0.001	-0.07±0.01
	$\epsilon_\parallel$[%]	0.020±0.001	0.097±0.002
	R	1.005±0.004	1.02±0.02
B3	tilt[°]	-0.0033 ± 0.0002	-0.0013 ± 0.0001
	$a_\perp$[Å]	5.655 ± 0.001	5.655 ± 0.001
	$a_\parallel$[Å]	5.665±0.007	5.663±0.005
	$\delta_\perp$[%]	4.12±0.02	4.11±0.02
	$\delta_\parallel$[%]	4.31±0.08	4.27±0.05
	$\epsilon_\perp$[%]	-0.08±0.04	-0.01±0.01
	$\epsilon_\parallel$[%]	0.11±0.04	0.09±0.05
	R	1.03 ± 0.03	1.02 ± 0.01
C3	tilt[°]	-0.0339 ± 0.0002	0.0037 ± 0.0001
	$a_\perp$[Å]	5.657±0.001	5.657±0.001
	$a_\parallel$[Å]	5.654±0.004	5.657±0.002
	$\delta_\perp$[%]	4.17±0.03	4.17±0.04
	$\delta_\parallel$[%]	4.10±0.02	4.16±0.01
	$\epsilon_\perp$[%]	0.03±0.02	0.00±0.01
	$\epsilon_\parallel$[%]	-0.04±0.03	0.00±0.01
	R	0.99±0.03	1.00±0.04

Sample	Parameter	Azimuth 0°	Azimuth 90°
D3	tilt[°]	0.0039± 0.0001	0.0034 ± 0.0001
	$a_\perp$[Å]	5.657±0.001	5.658±0.001
	$a_\parallel$[Å]	5.658±0.002	5.658±0.001
	$\delta_\perp$[%]	4.165±0.001	4.170±0.003
	$\delta_\parallel$[%]	4.181±0.004	4.173±0.002
	$\epsilon_\perp$[%]	0.000±0.002	-0.000±0.001
	$\epsilon_\parallel$[%]	0.000±0.001	0.000±0.003
	R	1.002± 0.003	1.000 ± 0.002
E3	tilt[°]	-0.0292 ± 0.0001	-0.0012 ± 0.0001
	$a_\perp$[Å]	5.6572±0.0003	5.6574±0.0004
	$a_\parallel$[Å]	5.6576±0.0001	5.6578±0.0002
	$\delta_\perp$[%]	4.164±0.003	4.168±0.004
	$\delta_\parallel$[%]	4.171±0.001	4.174±0.002
	$\epsilon_\perp$[%]	0.000±0.004	0.000±0.001
	$\epsilon_\parallel$[%]	0.000±0.001	0.000±0.002
	R	1.001±0.005	1.001±0.003
F3	tilt[°]	-0.0602 ± 0.0001	0.0153 ± 0.0001
	$a_\perp$[Å]	5.657±0.001	5.657±0.003
	$a_\parallel$[Å]	5.651±0.004	5.659±0.001
	$\delta_\perp$[%]	4.165±0.007	4.164±0.007
	$\delta_\parallel$[%]	4.043±0.009	4.194±0.006
	$\epsilon_\perp$[%]	0.05±0.02	-0.01±0.01
	$\epsilon_\parallel$[%]	-0.07±0.01	0.02±0.02
	R	1.00±0.01	0.98±0.03
A4	tilt[°]	-0.0085 ± 0.0001	-0.0130 ± 0.0001
	$a_\perp$[Å]	5.652±0.004	5.651±0.003
	$a_\parallel$[Å]	5.667±0.006	5.668±0.008
	$\delta_\perp$[%]	4.06±0.04	4.06±0.02
	$\delta_\parallel$[%]	4.35±0.08	4.36±0.07
	$\epsilon_\perp$[%]	-0.12±0.02	-0.12±0.03
	$\epsilon_\parallel$[%]	0.16±0.07	0.16±0.07
	R	1.04±0.03	1.04±0.04
B4	tilt[°]	-0.0068 ± 0.0001	-0.0036 ± 0.0001
	$a_\perp$[Å]	5.6561 ± 0.0004	5.6561 ± 0.0002
	$a_\parallel$[Å]	5.6602 ± 0.0007	5.6605 ± 0.0007
	$\delta_\perp$[%]	4.120 ± 0.007	4.143 ± 0.004
	$\delta_\parallel$[%]	4.244 ± 0.005	4.225 ± 0.00
	$\epsilon_\perp$[%]	-0.04 ± 0.01	-0.03 ± 0.01
	$\epsilon_\parallel$[%]	0.05 ± 0.02	0.05 ± 0.02
	R	1.01 ± 0.02	1.01 ± 0.01
	tilt[°]	-0.0080 ± 0.0002	-0.0112 ± 0.0001
	$a_\perp$[Å]	5.6575±0.0002	5.6575±0.0005
	$a_\parallel$[Å]	5.6597±0.0004	5.6575±0.0002

Sample	Parameter	Azimuth 0°	Azimuth 90°
C4	$\delta_{\perp}$[%]	4.174±0.001	4.169±0.006
	$\delta_{\parallel}$[%]	4.210±0.007	4.174±0.005
	$\epsilon_{\perp}$[%]	-0.016±0.004	-0.000±0.007
	$\epsilon_{\parallel}$[%]	0.022±0.008	0.000±0.004
	R	1.01 ± 0.01	1.000±0.007
D4	tilt[°]	-0.0036 ± 0.0001	0.0035 ± 0.0001
	$a_{\perp}$[Å]	5.6561 ± 0.0004	5.6575±0.0002
	$a_{\parallel}$[Å]	5.6596±0.0004	5.6571±0.0005
	$\delta_{\perp}$[%]	4.166±0.001	4.169±0.001
	$\delta_{\parallel}$[%]	4.208±0.005	4.163±0.006
	$\epsilon_{\perp}$[%]	-0.017±0.004	0.000±0.004
	$\epsilon_{\parallel}$[%]	0.023±0.007	0.000±0.002
	R	1.010±0.002	0.999±0.005
E4	tilt[°]	0.0034 ± 0.0001	0.0044 ± 0.0002
	$a_{\perp}$[Å]	5.6575±0.0005	5.6574±0.0001
	$a_{\parallel}$[Å]	5.6584±0.0004	5.6578±0.0004
	$\delta_{\perp}$[%]	4.169±0.004	4.168±0.002
	$\delta_{\parallel}$[%]	4.187±0.002	4.175±0.002
	$\epsilon_{\perp}$[%]	0.000±0.003	0.000±0.004
	$\epsilon_{\parallel}$[%]	0.010±0.004	0.000±0.001
	R	1.002±0.001	1.001±0.002
F4	tilt[°]	-0.0028 ± 0.0001	-0.0017 ± 0.0001
	$a_{\perp}$[Å]	5.657±0.004	5.6570±0.0001
	$a_{\parallel}$[Å]	5.658±0.006	5.6570±0.0002
	$\delta_{\perp}$[%]	4.16±0.02	4.160±0.003
	$\delta_{\parallel}$[%]	4.19±0.04	4.161±0.001
	$\epsilon_{\perp}$[%]	0.07±0.03	0.000±0.002
	$\epsilon_{\parallel}$[%]	-0.09±0.04	0.000±0.004
	R	1.01±0.02	1.000±0.001

Table A.2 Calculated parameters from the main maxima of the symmetrical (004) and the asymmetrical (224) or (404) diffractios for the ridges samples.

Sample	Parameter	Azimuth 45°	Azimuth 135°
G1	tilt[°]	0.0000 ± 0.0002	-0.0051 ± 0.0001
	$a_{\perp}$[Å]	5.651±0.005	5.651±0.006
	$a_{\parallel}$[Å]	5.6640±0.0009	5.666±0.001
	$\delta_{\perp}$[%]	4.057±0.004	4.056±0.005
	$\delta_{\parallel}$[%]	4.288±0.007	4.33±0.07
	$\epsilon_{\perp}$[%]	-0.095±0.005	-0.113±0.004
	$\epsilon_{\parallel}$[%]	0.127±0.002	0.150±0.005
	R	1.03±0.02	1.04±0.02
	tilt[°]	0.0049 ± 0.0002	0.0062 ± 0.0003

Sample	Parameter	Azimuth 45°	Azimuth 135°
G2	$a_\perp$[Å]	5.65±0.01	5.651±0.009
	$a_\parallel$[Å]	5.66±0.02	5.655±0.008
	$\delta_\perp$[%]	4.05±0.04	4.05±0.05
	$\delta_\parallel$[%]	4.17±0.01	4.13±0.03
	$\epsilon_\perp$[%]	-0.05±0.02	-0.03±0.01
	$\epsilon_\parallel$[%]	0.06±0.01	0.040±0.009
	R	1.02±0.03	1.01±0.04
H1	tilt[°]	-0.0036 ± 0.0001	-0.0053 ± 0.0003
	$a_\perp$[Å]	5.653±0.001	5.653±0.001
	$a_\parallel$[Å]	5.661±0.001	5.658±0.001
	$\delta_\perp$[%]	4.094±0.005	4.091±0.004
	$\delta_\parallel$[%]	4.24±0.01	4.186±0.008
	$\epsilon_\perp$[%]	-0.061±0.008	-0.04±0.01
	$\epsilon_\parallel$[%]	0.081±0.07	0.152±0.08
	R	1.02±0.01	1.01±0.03
H2	tilt[°]	0.0052 ± 0.0001	0.0027 ± 0.0001
	$a_\perp$[Å]	5.6541±0.0001	5.655±0.002
	$a_\parallel$[Å]	5.6558±0.0001	5.654±0.005
	$\delta_\perp$[%]	4.108±0.002	4.112±0.004
	$\delta_\parallel$[%]	4.138±0.004	4.114±0.007
	$\epsilon_\perp$[%]	-0.012±0.002	0.00±0.01
	$\epsilon_\parallel$[%]	0.017±0.004	0.00±0.01
	R	1.042±0.009	1.00±0.03
I1	tilt[°]	0.0071 ± 0.0001	-0.0011 ± 0.0001
	$a_\perp$[Å]	5.654±0.001	5.6541±0.0008
	$a_\parallel$[Å]	5.664±0.003	5.6555±0.0004
	$\delta_\perp$[%]	4.11±0.02	4.106±0.007
	$\delta_\parallel$[%]	4.29±0.01	4.133±0.009
	$\epsilon_\perp$[%]	-0.076±0.004	-0.01±0.03
	$\epsilon_\parallel$[%]	0.10±0.02	0.015±0.007
	R	1.03±0.03	1.00±0.03
I2	tilt[°]	0.0009 ± 0.0001	-0.0013 ± 0.0001
	$a_\perp$[Å]	5.6542±0.0004	5.6541±0.0002
	$a_\parallel$[Å]	5.6615±0.0008	5.6665±0.0001
	$\delta_\perp$[%]	4.108±0.002	4.107±0.001
	$\delta_\parallel$[%]	4.243±0.001	4.336±0.004
	$\epsilon_\perp$[%]	-0.055±0.007	0.13±0.04
	$\epsilon_\parallel$[%]	0.074±0.003	0.05 ± 0.02
	R	1.018±0.009	1.031±0.002
J1	tilt[°]	-0.0195 ± 0.0001	-0.0109 ± 0.0001
	$a_\perp$[Å]	5.655±0.002	5.655±0.004
	$a_\parallel$[Å]	5.654±0.007	5.665±0.002
	$\delta_\perp$[%]	4.122±0.04	4.123±0.001

Sample	Parameter	Azimuth 45°	Azimuth 135°
	$\delta_{\parallel}$[%]	4.021±0.003	4.305±0.001
	$\epsilon_{\perp}$[%]	0.041±0.007	-0.075±0.004
	$\epsilon_{\parallel}$[%]	-0.06±0.02	0.10±0.05
	R	1.002±0.007	1.025±0.005
	tilt[°]	0.0031 ± 0.0001	-0.0063 ± 0.0001
	$a_{\perp}$[Å]	5.655±0.001	5.655±0.004
	$a_{\parallel}$[Å]	5.666±0.001	5.655±0.003
J2	$\delta_{\perp}$[%]	4.131±0.005	4.13±0.04
	$\delta_{\parallel}$[%]	4.319±0.002	4.13±0.02
	$\epsilon_{\perp}$[%]	-0.08±0.04	0.00±0.01
	$\epsilon_{\parallel}$[%]	0.10±0.02	0.00±0.01
	R	1.026 ± 0.007	1.00 ± 0.001
	tilt[°]	0.0115 ± 0.0001	0.0013 ± 0.0001
	$a_{\perp}$[Å]	5.6551±0.0003	5.6583±0.0002
	$a_{\parallel}$[Å]	5.6947±0.0002	5.6551±0.0001
K1	$\delta_{\perp}$[%]	4.124±0.001	4.125±0.002
	$\delta_{\parallel}$[%]	4.837±0.003	4.262±0.002
	$\epsilon_{\perp}$[%]	-0.118±0.004	-0.056±0.004
	$\epsilon_{\parallel}$[%]	0.158±0.001	0.075±0.001
	R	1.059±0.001	1.002±0.002
	tilt[°]	0.0001 ± 0.0000	0.0001 ± 0.0001
	$a_{\perp}$[Å]	5.655 ± 0.004	5.656 ± 0.002
	$a_{\parallel}$[Å]	5.655 ± 0.007	5.674 ± 0.003
K2	$\delta_{\perp}$[%]	4.129 ± 0.007	4.135 ± 0.007
	$\delta_{\parallel}$[%]	4.119 ± 0.005	4.477 ± 0.003
	$\epsilon_{\perp}$[%]	0.000 ± 0.001	-0.141 ± 0.007
	$\epsilon_{\parallel}$[%]	-0.010 ± 0.002	0.187 ± 0.007
	R	0.999 ± 0.001	1.045 ± 0.004
	tilt[°]	0.0048 ± 0.0001	0.0014 ± 0.0001
	$a_{\perp}$[Å]	5.655 ± 0.003	5.655 ± 0.005
	$a_{\parallel}$[Å]	5.667 ± 0.009	5.697 ± 0.007
L1	$\delta_{\perp}$[%]	4.123 ± 0.001	4.12 ± 0.08
	$\delta_{\parallel}$[%]	4.339 ± 0.008	4.89 ± 0.02
	$\epsilon_{\perp}$[%]	-0.09 ± 0.01	-0.32 ± 0.03
	$\epsilon_{\parallel}$[%]	0.12 ± 0.02	0.42 ± 0.04
	R	1.00 ± 0.02	1.01 ± 0.03
	tilt[°]	-0.0092 ± 0.0001	-0.0014 ± 0.0001
	$a_{\perp}$[Å]	5.6551 ± 0.0008	5.6555 ± 0.0002
	$a_{\parallel}$[Å]	5.650 ± 0.002	5.662 ± 0.004
L2	$\delta_{\perp}$[%]	4.128 ± 0.004	4.130 ± 0.004
	$\delta_{\parallel}$[%]	4.035 ± 0.005	4.259 ± 0.008
	$\epsilon_{\perp}$[%]	0.038 ± 0.003	-0.053 ± 0.001
	$\epsilon_{\parallel}$[%]	-0.051 ± 0.002	0.071 ± 0.005

Sample	Parameter	Azimuth 45°	Azimuth 135°
	R	0.99 ± 0.01	1.018 ± 0.003

Table A.3 Calculated parameters from the secondary maxima of the symmetrical (004) and the asymmetrical (224) diffractions for the pillar samples.

Sample	Parameter	Azimuth 0°	Azimuth 90°
C2	tilt[°]	-0.0178 ± 0.0001	-0.0086 ± 0.0001
	$a_\perp$[Å]	5.6526±0.0003	5.6516±0.0003
	$a_\parallel$[Å]	5.6665±0.0002	5.68±0.007
	$\delta_\perp$[%]	4.079±0.002	4.061±0.001
	$\delta_\parallel$[%]	4.34±0.08	4.66±0.09
	$\epsilon_\perp$[%]	-0.106±0.001	-0.246±0.007
	$\epsilon_\parallel$[%]	0.141±0.007	0.33±0.08
	R	1.03±0.02	1.08±0.03
D2	tilt[°]	-0.0098 ± 0.0001	-0.0080 ± 0.0001
	$a_\perp$[Å]	5.6517±0.0001	5.6516±0.0001
	$a_\parallel$[Å]	5.6637±0.0002	5.6656±0.0001
	$\delta_\perp$[%]	4.063±0.002	4.062±0.001
	$\delta_\parallel$[%]	4.284±0.003	4.319±0.002
	$\epsilon_\perp$[%]	-0.091±0.001	-0.106±0.002
	$\epsilon_\parallel$[%]	0.121±0.001	0.141±0.001
	R	1.030±0.001	1.035±0.004
E2	tilt[°]	-0.0191 ± 0.0001	-0.0019 ± 0.0001
	$a_\perp$[Å]	5.6518±0.0001	5.6518±0.0002
	$a_\parallel$[Å]	5.6593±0.0002	5.6641±0.0002
	$\delta_\perp$[%]	4.064±0.001	4.065±0.002
	$\delta_\parallel$[%]	4.203±0.001	4.29±0.002
	$\epsilon_\perp$[%]	-0.057±0.001	-0.093±0.004
	$\epsilon_\parallel$[%]	-0.093±0.004	0.123±0.005
	R	1.019±0.003	1.031±0.007
F2	tilt[°]	-0.0112 ± 0.0003	-0.0101± 0.0003
	$a_\perp$[Å]	5.6517±0.0001	5.6517±0.0001
	$a_\parallel$[Å]	5.6660±0.0004	5.6658±0.0001
	$\delta_\perp$[%]	4.064±0.002	4.062±0.004
	$\delta_\parallel$[%]	4.327±0.004	4.323±0.003
	$\epsilon_\perp$[%]	-0.108±0.004	-0.107±0.003
	$\epsilon_\parallel$[%]	0.144±0.006	0.143±0.002
	R	1.036±0.007	1.036±0.004
C3	tilt[°]	-0.0029 ± 0.0002	-0.0275 ± 0.0001
	$a_\perp$[Å]	5.6527±0.0002	5.6526±0.0001
	$a_\parallel$[Å]	5.6638±0.0002	5.6622±0.0002
	$\delta_\perp$[%]	4.081±0.001	4.079±0.002
	$\delta_\parallel$[%]	4.286±0.004	4.256±0.004

Sample	Parameter	Azimuth 0°	Azimuth 90°
	$\epsilon_\perp$[%]	-0.084±0.004	-0.073±0.003
	$\epsilon_\parallel$[%]	0.112±0.003	0.097±0.001
	R	1.028±0.004	1.024±0.002
D3	tilt[°]	0.0015 ± 0.0001	0.0060 ± 0.0002
	$a_\perp$[Å]	5.6520±0.0001	5.652±0.004
	$a_\parallel$[Å]	5.6663±0.0002	5.6661±0.003
	$\delta_\perp$[%]	4.068±0.004	4.064±0.006
	$\delta_\parallel$[%]	4.333±0.003	4.326±0.007
	$\epsilon_\perp$[%]	-0.109±0.004	-0.108±0.001
	$\epsilon_\parallel$[%]	0.145±0.001	0.144±0.005
	R	1.036±0.003	1.036±0.004
E3	tilt[°]	-0.0111 ± 0.0001	-0.0143 ± 0.0001
	$a_\perp$[Å]	5.6515±0.0003	5.6512±0.0001
	$a_\parallel$[Å]	5.6654±0.0003	5.6660±0.0007
	$\delta_\perp$[%]	4.058±0.004	4.053±0.001
	$\delta_\parallel$[%]	4.313±0.003	4.326±0.004
	$\epsilon_\perp$[%]	-0.105±0.004	-0.113±0.008
	$\epsilon_\parallel$[%]	0.139±0.003	0.150±0.004
	R	1.035±0.005	1.037±0.006
F3	tilt[°]	-0.0012 ± 0.0001	-0.0087 ± 0.0001
	$a_\perp$[Å]	5.6517±0.0004	5.6517±0.0002
	$a_\parallel$[Å]	5.6653±0.0003	5.6660±0.0001
	$\delta_\perp$[%]	4.063±0.004	4.062±0.001
	$\delta_\parallel$[%]	4.314±0.007	4.326±0.002
	$\epsilon_\perp$[%]	-0.103±0.001	-0.109±0.004
	$\epsilon_\parallel$[%]	0.138±0.003	0.145±0.001
	R	1.034±0.001	1.0361±0.002
B4	tilt[°]	-0.0127 ± 0.0003	-0.0002 ± 0.0001
	$a_\perp$[Å]	5.653±0.004	5.652±0.004
	$a_\parallel$[Å]	5.658±0.003	5.659±0.001
	$\delta_\perp$[%]	4.081±0.008	4.072±0.007
	$\delta_\parallel$[%]	3.992±0.009	4.006±0.004
	$\epsilon_\perp$[%]	0.037±0.01	-0.03 ± 0.010.027±0.01
	$\epsilon_\parallel$[%]	-0.049±0.02	-0.036±0.03
	R	0.98±0.03	0.99±0.04
C4	tilt[°]	0.0318 ± 0.0001	-0.0110 ± 0.0001
	$a_\perp$[Å]	5.647±0.002	5.652±0.004
	$a_\parallel$[Å]	5.655±0.004	5.665±0.003
	$\delta_\perp$[%]	3.981±0.007	4.069±0.009
	$\delta_\parallel$[%]	4.131±0.008	4.301±0.006
	$\epsilon_\perp$[%]	-0.06±0.01	-0.10±0.01
	$\epsilon_\parallel$[%]	0.08±0.03	0.13±0.01

Sample	Parameter	Azimuth 0°	Azimuth 90°
	R	1.02±0.02	1.03±0.01
D4	tilt[°]	-0.0032 ± 0.0001	-0.0029 ± 0.0001
	$a_\perp$[Å]	5.6524±0.0001	5.6526±0.0004
	$a_\parallel$[Å]	5.6648±0.0003	5.66518±0.0001
	$\delta_\perp$[%]	4.076±0.001	4.079±0.001
	$\delta_\parallel$[%]	4.304±0.002	4.311±0.002
	$\epsilon_\perp$[%]	-0.094±0.003	-0.096±0.004
	$\epsilon_\parallel$[%]	0.125±0.001	0.127±0.001
	R	1.031±0.002	1.031±0.003
E4	tilt[°]	0.0035 ± 0.0001	0.0025 ± 0.0001
	$a_\perp$[Å]	5.6527±0.0001	5.6525±0.0002
	$a_\parallel$[Å]	5.6633±0.0003	5.6633±0.0001
	$\delta_\perp$[%]	4.081±0.002	4.077±0.005
	$\delta_\parallel$[%]	4.276±0.004	4.277±0.001
	$\epsilon_\perp$[%]	-0.080±0.001	-0.082±0.002
	$\epsilon_\parallel$[%]	0.107±0.005	0.110±0.004
	R	1.027±0.002	1.027±0.003
F4	tilt[°]	-0.0017 ± 0.0001	-0.0033 ± 0.0001
	$a_\perp$[Å]	5.652±0.004	5.6510±0.0005
	$a_\parallel$[Å]	5.660±0.002	5.6607±0.0002
	$\delta_\perp$[%]	4.07±0.05	4.049±0.002
	$\delta_\parallel$[%]	4.10±0.01	4.228±0.004
	$\epsilon_\perp$[%]	-0.01±0.06	-0.074±0.002
	$\epsilon_\parallel$[%]	0.02±0.01	0.098±0.004
	R	1.00±0.02	1.025±0.001

Table A.4 Calculated parameters from the secondary maxima of the symmetrical (004) and the asymmetrical (404) diffractions for the ridge samples.

Sample	Parameter	Azimuth 45°	Azimuth 135°
I1	tilt[°]	0.0053 ± 0.0003	0.0065 ± 0.0001
	$a_\perp$[Å]	5.651±0.001	5.652±0.002
	$a_\parallel$[Å]	5.667±0.004	5.667±0.003
	$\delta_\perp$[%]	4.056±0.006	4.067±0.002
	$\delta_\parallel$[%]	4.346±0.002	4.891±0.002
	$\epsilon_\perp$[%]	-0.119±0.007	-0.34±0.01
	$\epsilon_\parallel$[%]	0.16±0.04	0.45±0.06
	R	1.04±0.02	1.11±0.08
I2	tilt[°]	-0.0046 ± 0.0001	-0.0016 ± 0.0001
	$a_\perp$[Å]	5.652±0.006	5.652±0.007
	$a_\parallel$[Å]	5.665±0.002	5.660±0.004
	$\delta_\perp$[%]	4.06±0.04	4.07±0.06

Sample	Parameter	Azimuth 0°	Azimuth 90°
	$\delta_{\parallel}$[%]	4.30±0.01	4.22±0.08
	$\epsilon_{\perp}$[%]	-0.101±0.001	-0.06±0.01
	$\epsilon_{\parallel}$[%]	0.134±0.002	0.08±0.04
	R	1.03±0.07	1.02±0.05
J1	tilt[°]	-0.0028 ± 0.0002	-0.0006 ± 0.0001
	$a_{\perp}$[Å]	5.666 ± 0.004	5.661 ± 0.007
	$a_{\parallel}$[Å]	5.650 ± 0.007	5.660 ± 0.009
	$\delta_{\perp}$[%]	4.30 ± 0.07	4.31 ± 0.04
	$\delta_{\parallel}$[%]	4.24 ± 0.05	4.23 ± 0.07
	$\epsilon_{\perp}$[%]	-0.10 ± 0.01	-0.16 ± 0.01
	$\epsilon_{\parallel}$[%]	0.19 ± 0.08	0.14 ± 0.07
	R	1.12 ± 0.08	1.11 ± 0.04
J2	tilt[°]	-0.0011 ± 0.0001	-0.0009 ± 0.0001
	$a_{\perp}$[Å]	5.656 ± 0.004	5.656 ± 0.002
	$a_{\parallel}$[Å]	5.660 ± 0.008	5.669 ± 0.009
	$\delta_{\perp}$[%]	4.27 ± 0.08	4.28 ± 0.04
	$\delta_{\parallel}$[%]	4.31 ± 0.005	4.25 ± 0.05
	$\epsilon_{\perp}$[%]	-0.17 ± 0.03	-0.31 ± 0.09
	$\epsilon_{\parallel}$[%]	0.25 ± 0.02	0.25 ± 0.07
	R	1.01 ± 0.01	1.01 ± 0.01
K1	tilt[°]	0.0184 ± 0.0004	0.0017 ± 0.0001
	$a_{\perp}$[Å]	5.6505±0.0003	5.652±0.002
	$a_{\parallel}$[Å]	5.6802±0.0002	5.662±0.003
	$\delta_{\perp}$[%]	4.041±0.002	4.06±0.01
	$\delta_{\parallel}$[%]	4.588±0.001	4.26±0.04
	$\epsilon_{\perp}$[%]	-0.225±0.002	-0.08±0.02
	$\epsilon_{\parallel}$[%]	0.321±0.005	0.11±0.08
	R	1.01 ± 0.011.073±0.009	1.03±0.03
K2	tilt[°]	-0.0018 ± 0.0001	-0.0006 ± 0.0002
	$a_{\perp}$[Å]	5.6519 ± 0.0008	5.6561 ± 0.0002
	$a_{\parallel}$[Å]	5.665 ± 0.002	5.659 ± 0.007
	$\delta_{\perp}$[%]	4.07 ± 0.07	4.18 ± 0.07
	$\delta_{\parallel}$[%]	4.32 ± 0.04	4.24 ± 0.07
	$\epsilon_{\perp}$[%]	-0.10 ± 0.02	-0.11 ± 0.01
	$\epsilon_{\parallel}$[%]	0.14 ± 0.08	0.18 ± 0.07
	R	1.03 ± 0.03	1.04 ± 0.02

Appendix B

Asymmetrical maps

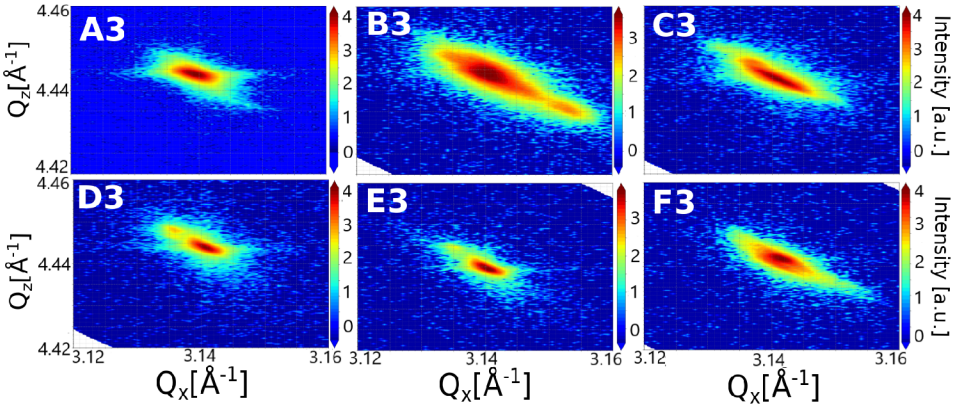

Figure B.1 Reciprocal space maps around asymmetrical diffraction (224) for samples from X3 series

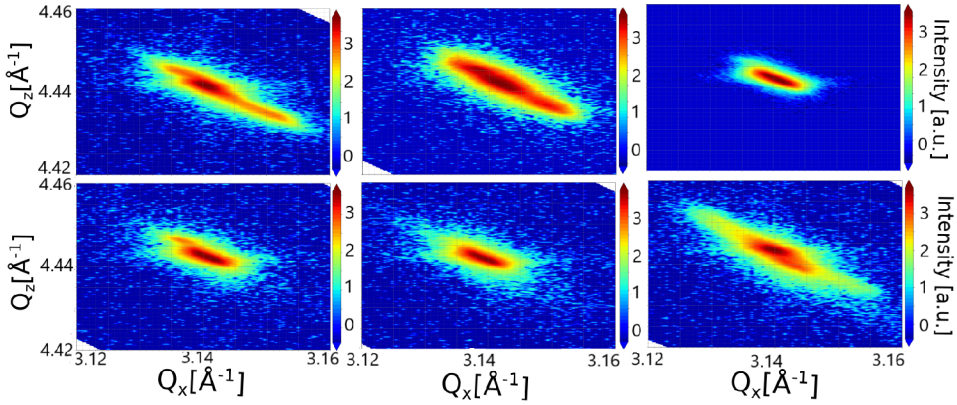

Figure B.2 Reciprocal space maps around asymmetrical diffraction (224) for samples from X4 series

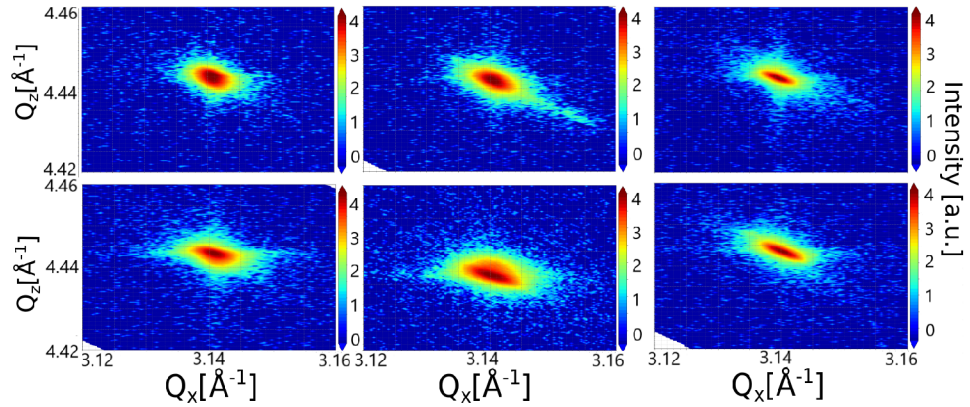

Figure B.3 Reciprocal space maps around asymmetrical diffraction (224) for ridges samples parallel with [110]. Diffraction plane is in direction parallel with ridges.

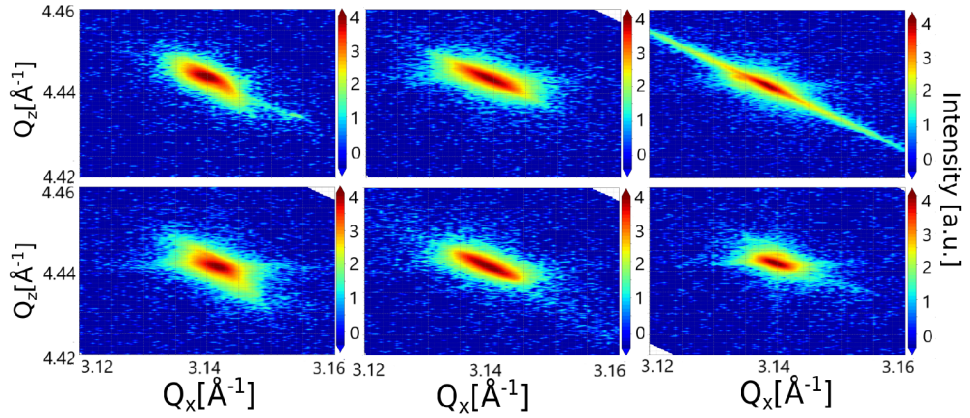

Figure B.4 Reciprocal space maps around asymmetrical diffraction (224) for ridges samples parallel with [110]. Diffraction plane is in direction perpendicular with ridges.

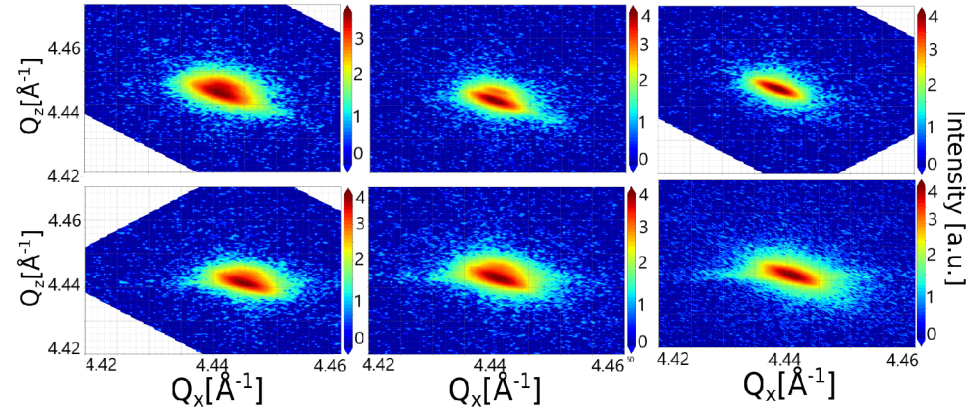

Figure B.5 Reciprocal space maps around asymmetrical diffraction (404) for the samples with ridges parallel with [100]. Diffraction plane is in direction parallel with ridges.

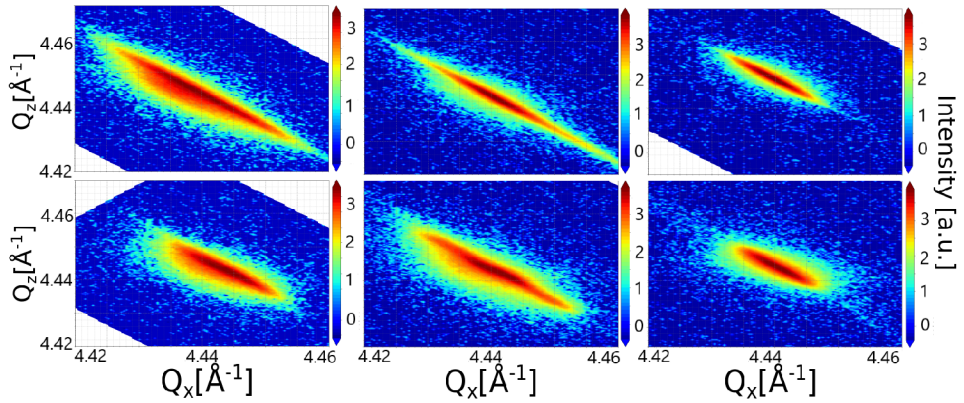

Figure B.6 Reciprocal space maps around asymmetrical diffraction (404) for the samples with ridges parallel with [100]. Diffraction plane is in direction perpendicular with ridges.